

AD_____

Award Number:

W81XWH-10-1-0730

TITLE:

Novel Electromagnetic - Ultrasound Synergistic Technique for Treatment of Cancer

PRINCIPAL INVESTIGATOR:

Paul Carson, Ph.D.

CONTRACTING ORGANIZATION:

University of Michigan, Ann Arbor, MI, 48109

REPORT DATE: S~{æ↑âæãÁG€FĞ

TYPE OF REPORT:

Final

PREPARED FOR: U.S. Army Medical Research and Materiel Command
Fort Detrick, Maryland 21702-5012

DISTRIBUTION STATEMENT:

Approved for public release; distribution unlimited

The views, opinions and/or findings contained in this report are those of the author(s) and should not be construed as an official Department of the Army position, policy or decision unless so designated by other documentation.

REPORT DOCUMENTATION PAGE				Form Approved OMB No. 0704-0188	
Public reporting burden for this collection of information is estimated to average 1 hour per response, including the time for reviewing instructions, searching existing data sources, gathering and maintaining the data needed, and completing and reviewing this collection of information. Send comments regarding this burden estimate or any other aspect of this collection of information, including suggestions for reducing this burden to Department of Defense, Washington Headquarters Services, Directorate for Information Operations and Reports (0704-0188), 1215 Jefferson Davis Highway, Suite 1204, Arlington, VA 22202-4302. Respondents should be aware that notwithstanding any other provision of law, no person shall be subject to any penalty for failing to comply with a collection of information if it does not display a currently valid OMB control number. PLEASE DO NOT RETURN YOUR FORM TO THE ABOVE ADDRESS.					
1. REPORT DATE November 2013		2. REPORT TYPE Final		3. DATES COVERED 1 Sep 2010-31 Aug 2013	
4. TITLE AND SUBTITLE Novel Electromagnetic - Ultrasound Synergistic Technique for Treatment of Cancer				5a. CONTRACT NUMBER	
				5b. GRANT NUMBER W81XWH-10-1-0730	
				5c. PROGRAM ELEMENT NUMBER	
6. AUTHOR(S) Paul Carson, Ph.D. Oliver Kripfgans, Ph.D. Brian Fowlkes, Ph.D. Email: pcarson@umich.edu				5d. PROJECT NUMBER	
				5e. TASK NUMBER	
				5f. WORK UNIT NUMBER	
7. PERFORMING ORGANIZATION NAME(S) AND ADDRESS(ES) University of Michigan Ann Arbor, MI, 48109				8. PERFORMING ORGANIZATION REPORT NUMBER	
9. SPONSORING / MONITORING AGENCY NAME(S) AND ADDRESS(ES) U.S. Army Medical Research and Materiel Command Fort Detrick, Maryland 21702-5012				10. SPONSOR/MONITOR'S ACRONYM(S)	
				11. SPONSOR/MONITOR'S REPORT NUMBER(S)	
12. DISTRIBUTION / AVAILABILITY STATEMENT Approved for Public Release; Distribution Unlimited					
13. SUPPLEMENTARY NOTES					
14. ABSTRACT Hyperthermia and thermal ablation are thermal therapies in which the cytotoxic effects of elevated temperatures in tissue are induced to achieve cell death or render the cells more vulnerable to ionizing radiation and chemical toxins. In application of a thermal ablation approach, high intensity focused ultrasound (HIFU) and high intensity focused microwave (HIFW) have been explored for various medical conditions. Our research is primarily directed at addressing severe limitations of HIFU, that is, very slow treatment times for large, deep lesions, including those close to the chest wall, by combining HIFU and HIFW, and in each modality, introducing new techniques that substantially enhance the treatment results. Two modalities will capitalize on the advantages of each in various situations, and will allow comparison of those advantages as the research progresses to in vivo studies. In this collaborative research, work between the Microwave and Ultrasound groups is being conducted to develop a technique that will synergize the fast heat delivery properties of microwaves with high spatial resolution of ultrasound. This particular progress report is for the ultrasound portion and its future integration with the microwave system.					
15. SUBJECT TERMS-					
16. SECURITY CLASSIFICATION OF:			17. LIMITATION OF ABSTRACT UU	18. NUMBER OF PAGES 66	19a. NAME OF RESPONSIBLE PERSON USAMRMC
a. REPORT U	b. ABSTRACT U	c. THIS PAGE U			19b. TELEPHONE NUMBER (include area code)

Table of Contents

INTRODUCTION.....	2
BODY	2
KEY RESEARCH ACCOMPLISHMENTS.....	4
REPORTABLE OUTCOMES.....	4
CONCLUSION.....	6
REFERENCES.....	6
APPENDICES.....	8

Partnering PI Final Progress Report: DOD Award BC095397P1

Initiating PI: Mahta Moghaddam, Professor, EECS, University of Southern California

Partnering PI: Paul Carson, Professor, Basic Radiological Sciences, University of Michigan

Grant Title: Novel Electromagnetic - Ultrasound Synergistic Technique for Treatment of Cancer

INTRODUCTION

Hyperthermia and thermal ablation are thermal therapies in which the cytotoxic effects of elevated temperatures in tissue are induced to achieve cell death or render the cells more vulnerable to ionizing radiation and chemical toxins. In application of a thermal ablation approach, high intensity focused ultrasound (HIFU) and high intensity focused microwave (HIFW) have been explored for various medical conditions. Our research is primarily directed at addressing severe limitations of HIFU, that is, very slow treatment times for large, deep lesions, including those close to the chest wall, by combining HIFU and HIFW, and in each modality, introducing new techniques that substantially enhance the treatment results. Two modalities will capitalize on the advantages of each in various situations, and will allow comparison of those advantages as the research progresses to *in vivo* studies. In this collaborative research, work between the Microwave and Ultrasound groups is being conducted to develop a technique that will synergize the fast heat delivery properties of microwaves with high spatial resolution of ultrasound. This particular progress report is for the ultrasound portion and its future integration with the microwave system.

BODY

Task 1. Design and construct an ultrasound breast lesion treatment and targeting system, capable of treatment of locations throughout the breast including next to the chest wall and compatible with microwave treatment from the other side.

Research Findings: Progress on the treatment system has included construction and some programming of the full driving electronics for the 298 element transducer array that is compatible with treatment from both sides of the compressed breast in the mammographic geometry and also from outside a 20 cm OD microwave antenna array when the array can be

made acoustically transparent [1]. Fig. 1 shows the multichannel ultrasound electronics. Maximum acoustic pressure achieved was approximately 30 MPa PP. A fire destroyed almost the entire laboratory containing the therapeutic ultrasound transducer array electronics, but insurance is paying for their reconstruction with some design improvements resulting from our experience at no additional cost.

For practical targeting, we have the GE Vivid 7 scanner with V3 (2000 element) 2D array that fits easily in the 55 mm opening in the center of the US therapy arrays. More advanced research on ultrasound imaging for targeting and correcting the microwave and US therapeutic and imaging beams was conducted in our laboratory with our help by one of Dr. Moghaddam's students, Mark Haynes. That work provides significant advances in calibration of ultrasound transducer arrays for full wave migration imaging that can provide acoustic properties of tissues including speed of sound, scattering, attenuation and compressibility [2, 3].

Task 2. Evaluate lesion production with microwave and ultrasound (single element and with the array transducers) in breast tissue mimicking phantoms at depths up to 5-7 cm.

Research Findings: The two modes are not combined yet. It was determined that a microwave antenna on a flat compression plate would not give enough focal gain for deeper heating in the breast than at the skin. A cylindrical microwave antenna was designed and constructed as reported, with record target to surrounding tissue heating efficiency. These results are described in the report of the initiating P.I. While our ultrasound could be brought in from the bottom of the cylindrical microwave antenna, it was deemed more effective to refine the two modalities separately and then initiate a new project to allow ultrasound transmission through the microwave antenna. Plans and quite satisfactory progress with ultrasound heating and its enhancement have been and are being reported publicly [1, 4].

Task 3. Test operation of simultaneous ultrasound and microwave heating of tissue-mimicking phantoms. Obtain initial data on beam steering errors for validation of future correction of same.

Research Findings: As discussed in Task 2, simultaneous operation has not been achieved because the ultrasound transmission through the existing microwave substrate material is unacceptably high. However, experimental results using laboratory prototypes generated focused heating sufficient for an antitumor effect deep in the breast in tissue-mimicking gelatin phantoms with both microwave and ultrasound separately. Heating focal spot sizes were as small as 1.5 cm with microwaves [5] and 1.5 mm with ultrasound [1]. Reasonably acceptable lipid/water emulsions have been found as coupling fluids for both modalities as well as for mammography [5]. They currently leave an oily residue on the skin [6].

Task 4. Evaluate future acceleration of acoustic treatment by increasing sound absorption only in the treatment zone by creation of bubbles in the acoustic focus using acoustic droplet vaporization (ADV); this will also allow use of higher microwave and US powers by shielding of ultrasonically distal skin.

Research Findings: Exceptional additional progress has been made with acceleration of the ultrasound treatment by scattering from acoustically vaporized droplets [1, 4]. Emulsions of perfluorocarbon droplets (lipid coated, C5F12, $\text{Ø } 2.0 \pm 0.1 \text{ }\mu\text{m}$, $\sim 99\% < 8 \text{ }\mu\text{m Ø}$) were used to create thermal agents in polyacrylamide phantoms. The emulsion concentration in the gel was 3×10^5 droplets per mL. Egg white was incorporated to allow for visual inspection of the phantoms after acoustic exposure. *In situ* MRI temperature monitoring limited focal heating to 75°C. Lesion sizes were measured as a function of applied acoustic power. A similar, but different acoustic array was employed for this recent experiment. Acoustic trenches, as sketched in Fig. 2, were created by vaporizing the droplets to form bubble walls in a spiral pattern on an underlying wall to trap sound scattered by the bubbles (Fig. 3b). Exposures in the middle of these trenches produced nearly uniform heating throughout the larger lesion (Fig. 3c). Lesion volumes increased by a factor of at least 17 when comparing lesion volumes in phantoms with droplets to without droplets. With the use of acoustic droplet vaporization (ADV)

and the resulting trenches, a uniform ablation volume of 15 mL was achieved in 15 s. These experiments were repeated with a commercial MR Guided HIFU system with the same results [1]. Safety of the emulsions was investigated via biodistribution studies [7].

Task 5. Design key features of a clinical dual sided treatment system with degrees of freedom equivalent to those of a mammography unit for treatment of the breast from mediolateral, through CC, to lateral medial. The design should allow treatment of all breast tissues imageable mammographically. The two-sided treatment could be either with a single modality or dual.

Task 6. Research Findings: Additional progress has been made in planning two approaches for the prone patient: 1) a bowl microwave antenna array with the ultrasound transducer manipulated around the outside with a robotic arm, an initial design of which was shown in the previous annual report: 2) a cylindrical microwave antenna with a circular ring ultrasound array for temperature measurements by speed of sound imaging. In this second approach, after treatment of the body of the breast, the breast could be compressed against the chest wall by a membrane for chest wall heating by the ultrasound therapeutic array, moved inside or below the cylindrical antenna. In both arrangements, the Ultrasound array can be split for treating through the antenna bowl or cylinder with the flat side of the array close to the chest wall when that is required. These two approaches were included in a DOD Breast Cancer Research Program Idea Expansion proposal and the second in an NIH RO1 proposal on a different body part. The resulting system from the latter could be used or adapted for breast cancer treatment. Neither proposal was funded, but resubmissions are planned.

KEY RESEARCH ACCOMPLISHMENTS

- Essential completion and calibration of an advanced 298 element array system for initial studies of lesioning for treatment from both sides of the compressed breast or for treatment through or from below a microwave antenna.
- Design of methods to integrate ultrasound and microwaves in a new, prone, uncompressed breast geometry with cylindrical or bowl antenna array.
- Further validation of ultrasound lesion production acceleration with uniform coverage using acoustic droplet vaporization.

REPORTABLE OUTCOMES

Manuscripts, publications, abstracts, presentations

All publications listed under REFERENCES, below, except for numbers 7 and 8.

Others:

Journal Research Articles and Dissertations (Copies of all but the PhD dissertation (Ref. 2) are attached):

References 2,3,5,6

M. Haynes, J. Stang, M. Moghaddam, "Microwave Breast Imaging System Prototype with Integrated Numerical Characterization," IEEE International Journal of Biomedical Imaging, Volume 2012, Article ID 706365, 18 pages, doi: 10.1155/2012/706365.

Meeting Proceedings Articles and Extended Abstracts:

Reference 1.

M. Haynes, L. van Nieuwstadt, S. Clarkson, J. Stang, C. Ward, M. Moghaddam, Ongoing Development of Microwave Breast Imaging System Components, 30th General Assembly and Scientific Symposium of the International Union of Radio Science (URSI), Aug 13-20, 2011, Istanbul Turkey (4 pages).

Abstracts and Meeting Presentations

Reference 4.

J. Stang, M. Haynes, M. Moghaddam, P. Carson "Transcutaneous microwave thermal therapy for breast cancer treatment using image based time-reversal focusing," Society for Thermal Medicine 2012 Annual Meeting, April 13-16, 2012, Portland, OR.

J. Stang, M. Haynes, M. Moghaddam, A Transcutaneous Microwave Thermal Therapy System Prototype For Breast Cancer Treatment Using Image Based Time-Reversal Focusing, National Radio Science Meeting, Jan 4-7, 2012, Boulder CO, invited abstract.

M. Haynes, J. Stang, M. Moghaddam, Evaluation of a Full-Cavity Numerical Characterization Approach for an Experimental Microwave Breast Imaging System, National Radio Science Meeting, Jan 4-7, 2012, Boulder CO, invited abstract.

F. Padilla, P. Carson, O.D. Kripfgans, M.L. Fabiilli, A. Covert, M. Zhang, J.B. Fowlkes, J. Stang, M. Ali, M. Moghaddam, "Collaborative Research on Microwave-Ultrasound Synergistic Techniques for Treatment of Breast Cancer: Ultrasound Ablation System and Method," Era of Hope Department of Defense Breast Cancer Research Program, Orlando, Florida 2011).

M.F. Zhang M. Fabiilli; P. Carson, F. Padilla, S.K. Swanson, O. Kripfgans, J.B. Fowlkes, "Spatial Control and Acceleration of Ultrasound Thermal Therapy Using Acoustic Droplet Vaporization," Procs., Amer. Inst. Ultras. Med., J. Ultras. Med, 30, S46, 2011).

J. Stang, P.L. Carson, O.D. Kripfgans, M. Fabiilli, A. Covert, M. Zhang, J.B. Fowlkes, F. Padilla, M. Ali, M. Moghaddam, Ultrasound Synergistic Techniques for Treatment of Breast Cancer, 2011 Era of Hope Conference, Aug 2-5, 2011, Orlando FL.

J. Stang, M. Ali, O.D. Kripfgans, J.B. Fowlkes, P.L. Carson, M. Moghaddam, Microwave Synergistic Techniques for Treatment of Breast Cancer, 2011 Era of Hope Conference, Aug 2-5, 2011, Orlando FL.

J. Stang, M. Moghaddam, O.D. Kripfgans, J.B. Fowlkes, P.L. Carson, Image Based Microwave Focusing for Transcutaneous Therapy in Combination with Focused Ultrasound Heating, 2011 Joint AAPM/COMP Meeting, Jul 31 - Aug 4, 2011, Vancouver BC.

J. Stang, M. Moghaddam, J.B. Fowlkes, P.L. Carson, Achieving Tumorcidal Dose with Focused Microwave Thermal Therapy, Proc. IEEE International Symposium on Antennas and Propagation and USNC/URSI National Radio Science Meeting, Jul 3-8, 2011, Spokane WA,.

M. Haynes, J. Stang, M. Moghaddam, Microwave Medical System Components with Possible MEMs Applications, Center for Wireless Integrated MicroSystems (WIMS), June 2011.

J. Stang, M. Moghaddam, O.D. Kripfgans, J.B. Fowlkes, P.L. Carson, Image Based Time-Reversal Focusing for Transcutaneous Microwave Thermal Therapy, Proc. National Radio Science Meeting, Jan 5-8, 2011, Boulder CO.

J. Stang, M. Moghaddam, M. Ali, Pinsky RW, J.B. Fowlkes, P.L. Carson, O.D. Kripfgans, A Transcutaneous Focused Microwave Ablation System for Noninvasive Cancer Therapy, RSNA 96th Scientific Assembly and Annual Meeting, Nov 28-Dec 3, 2010, Chicago IL.

M. Haynes, L. van Nieuwstadt, J. Stang, S. Clarkson, M. Moghaddam, Inverse Scattering System Components for Breast Imaging, Advances in Breast Cancer Research, Oct 2010, University of Arkansas.

J. Stang, J.B. Fowlkes, M. Moghaddam, M. Ali, O. Kripfgans, P.L. Carson, Modeling a Focused Microwave System for Transcutaneous Thermal Therapy, COMSOL Conference, Oct 7-9, 2010, Boston MA.

J. Stang, J.B. Fowlkes, M. Moghaddam, M. Ali, O. Kripfgans, and P.L. Carson, Numerical Modeling of a Transcutaneous Focused Ablation System for Noninvasive Cancer Therapy, NIBIB 2010 Training Grantees Meeting, Bethesda, MD, June 24-25, 2010.

Patents and licenses

- University of Michigan Invention Disclosure (2011), File Number 5273. Copy submitted separately by Initiating Partner.

Funding Applications

- NIH R01 Research Grant Application - Uniform Microwave Hyperthermia of Limb Sarcomas with US Monitoring and Control, submitted Feb. 5, 2013.
- DoD CDMRP/BCRP Idea Expansion Award Application BC123512P1 - Integrated Microwave and Ultrasound Synergistic System for Treatment of Breast Cancer 12/18/2012.

Resubmission of both is planned.

Employment and research opportunities

- Postdoctoral Research Fellow, John Stang, received position of Research Assistant Professor based on experience/training supported by this award.
- Mario Fabiilli, Postdoctoral Research Fellow
- Sneha A. Nair, Graduate Student Research Assistant
- Oliver Kripfgans, Assistant Research Scientist
-

CONCLUSION

Others have developed ultrasound therapy systems with similar amplitude and focusing characteristics, but not with the split shell array that can get a large part of the aperture close to the chest wall for treatment in the mammographic geometry or in the prone geometry in combination with microwave treatment. The mammographic geometry allows precise, sure targeting by x-ray and high resolution ultrasound as verified by a real time phased array that can operate with the therapeutic array. The prone geometry offers the promise of unprecedented uniformity and other control of temperature distributions by microwave and ultrasound for lesion ablation as well as whole breast and adjacent lymph nodes for local control. The acceleration of ultrasound thermal and ablative therapy by patterned vaporization of IV-injected perfluorocarbon microbubbles is very promising and still unique. Others have begun working with similar approaches using activation of gas containing ultrasound contrast agents and vaporization of perfluorocarbon nanodroplets.

REFERENCES

- [1.] Kripfgans OD, Zhang M, Fabiilli M, Carson P, Padilla F, Swanson S, Mougénout C, Fowlkes B, "Acceleration of ultrasound thermal therapy by patterned acoustic droplet vaporization," J. Acoust. Soc. Am. **135**(1), 537-545, (2014).
- [2.] Haynes MS, "Full-wave Nonlinear Inverse Scattering for Acoustic and Electromagnetic Breast Imaging, Ch. 2, Acoustic Inverse Scattering Algorithm, Ch. 8, Acoustic Inverse Scattering Experiment," PhD Dissertation, Univ. of Michigan, 2011, Ann Arbor, pp. 281.

- [3.] Haynes M, Verweij S, Moghaddam M, Carson P, "Transducer Model and Volume Integral Formulation for Self-Characterization of Commercial Ultrasound Probes in Transmission Acoustic Inverse Scattering," IEEE Trans. Ultras. Ferroelectrics Freq. Control, accepted with minor revisions, (2014).
- [4.] Fabiilli ML, Kripfgans OD, Swanson SD, Mougnot C, Carson PL, Zhang M, Fowlkes JB, "On the Acceleration of Ultrasound Thermal Therapy by Patterned Acoustic Droplet Vaporization," Annual Meeting Am.d Inst. Ultrasound Med., NY, NY (Apr 6-10, 2013).
- [5.] Stang J, Haynes M, Carson P, Moghaddam M, "A Preclinical system prototype for focused microwave thermal therapy of the breast," IEEE Trans Biomedical Eng. **59**(9), 2431 – 2438, (2012).
- [6.] Carson PL, LeCarpentier GL, Lashbrook CR, Lee WM, Goodsitt MM, Saitou K, Wang B, Baek S, Fowkes B, Local Compression During Automated Ultrasound Scanning and Methods of Acoustic Coupling (Application only), U.S.P. Office, No., US20130116570A1, May 9, 2013, pp. 25.
- [7.] Fabiilli ML, Piert MR, Koeppe RA, Sherman PS, Quesada CA, Kripfgans OD, "Assessment of the biodistribution of an [18F]FDG-loaded perfluorocarbon double emulsion using dynamic micro-PET in rats," Contrast Media and Molecular Imaging **8**(4), 366-374, (2013).

APPENDICES

Attach all appendices that contain information that supplements, clarifies or supports the text. Examples include original copies of journal articles, reprints of manuscripts and abstracts, a curriculum vitae, patent applications, study questionnaires, and surveys, etc.

APPENDIX 1 - SUPPORTING DATA

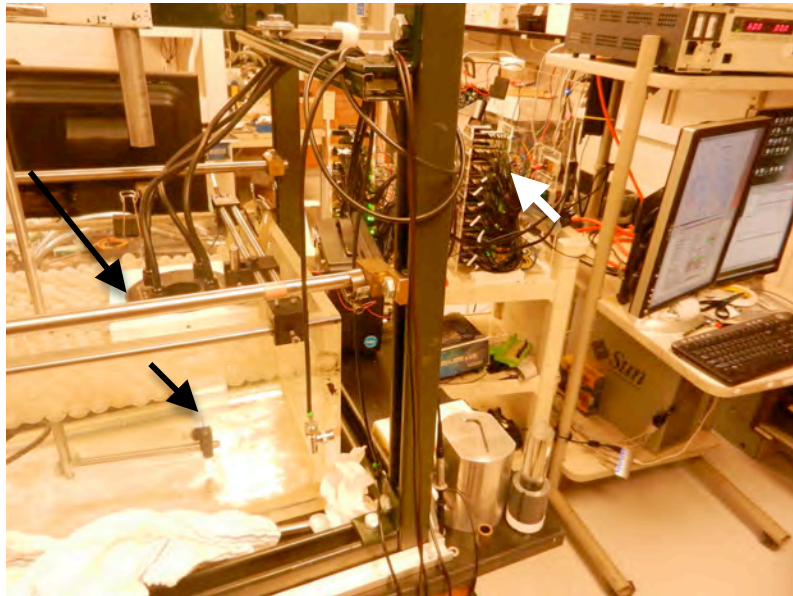


Figure 1.

Therapeutic array transducer (black arrow) in water tank aimed at needle hydrophone for automated output calibration (short black arrow). Amplifier and FPGA control boards and cables (white arrow) for the 298 driver channels are in a clear plastic electronics rack.

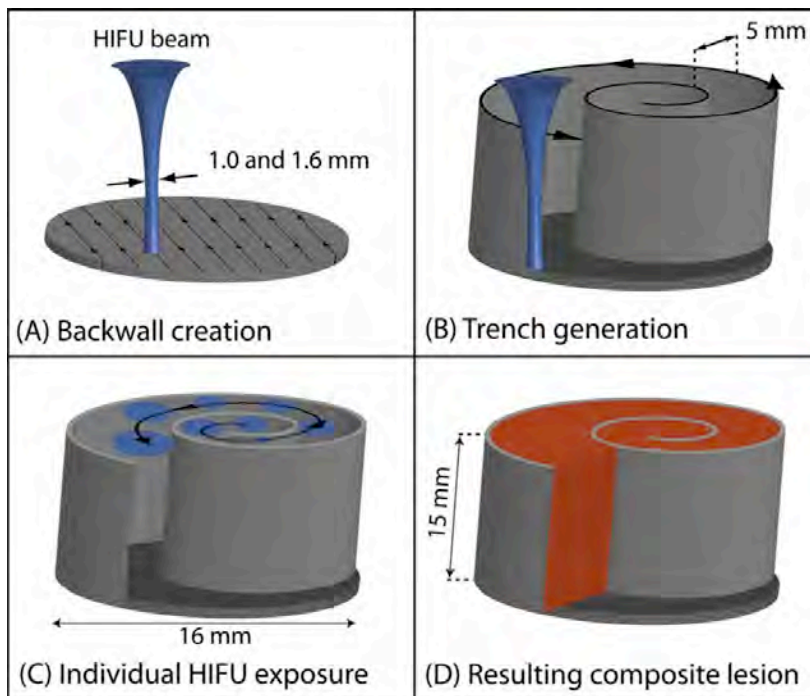


Figure 2. Diagram of an acoustic well and first layer, spiral treatment pattern.

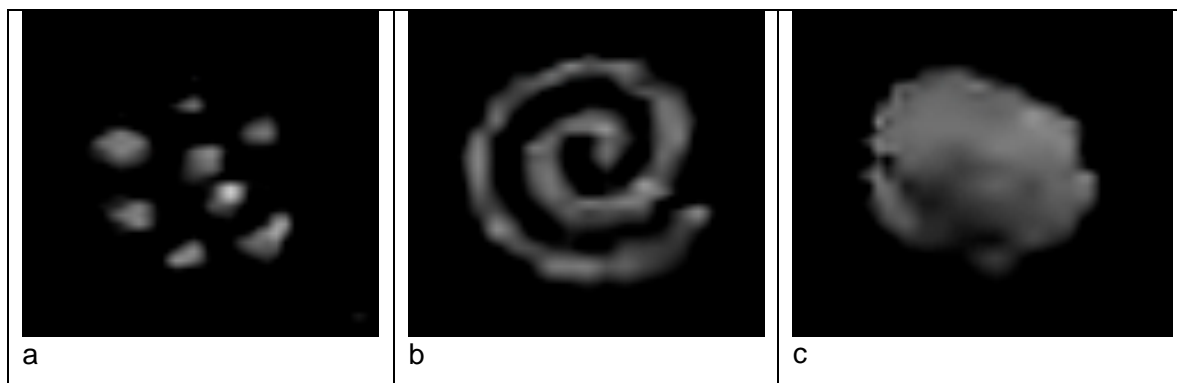


Figure 3. B-mode images of single (a) and compound lesions from a US HIFU system. The lesion in panel B is created in a rapid succession of individual HIFU pulses that were electronically steered. Twenty individual lesions were created in 500 ms to form the spiral acoustic trench (b). To only create the bubble walls, this spiral could have been at shorter duration, with thermal ablation accomplished in the next step. The formed acoustic trench was filled-in by 20 additional individual lesions which then created the solid lesion (c).

APPENDIX 2 – RESULTING PUBLICATIONS

Attached in the following order:

- [a.] Kripfgans OD, Zhang M, Fabiilli M, Carson P, Padilla F, Swanson S, Mougout C, Fowkes B, "Acceleration of ultrasound thermal therapy by patterned acoustic droplet vaporization," J. Acoust. Soc. Am. **135**(1), 537-545, (2014).
- [b.] M. Haynes, J. Stang, M. Moghaddam, "Microwave Breast Imaging System Prototype with Integrated Numerical Characterization," IEEE International Journal of Biomedical Imaging, Volume 2012, Article ID 706365, 18 pages, doi: 10.1155/2012/706365.
- [c.] Haynes M, Verweij S, Moghaddam M, Carson P, "Transducer Model and Volume Integral Formulation for Self-Characterization of Commercial Ultrasound Probes in Transmission Acoustic Inverse Scattering," IEEE Trans. Ultras. Ferroelectrics Freq. Control, accepted with minor revisions, (2014).
- [d.] Kripfgans OD, Zhang M, Fabiilli M, Carson P, Padilla F, Swanson S, Mougout C, Fowkes B, "Acceleration of ultrasound thermal therapy by patterned acoustic droplet vaporization," J. Acoust. Soc. Am. **135**(1), 537-545, (2014).
- [e.] Stang J, Haynes M, Carson P, Moghaddam M, "A Preclinical system prototype for focused microwave thermal therapy of the breast," IEEE Trans Biomedical Eng. **59**(9), 2431 – 2438, (2012). (Among the top 18 papers in the journal in the number of times it was downloaded in September 2012)
- [f.] Public description of project for BCRP public brochure.



Ultrasound thermal ablation system and methods for treatment of breast cancer

O. D. Kripfgans, A. Covert, F. R. Padilla, J. B. Fowlkes, M. L. Fabiilli, M. Moghaddam, and P. L. Carson

Citation: [AIP Conference Proceedings](#) **1481**, 185 (2012); doi: 10.1063/1.4757332

View online: <http://dx.doi.org/10.1063/1.4757332>

View Table of Contents: <http://scitation.aip.org/content/aip/proceeding/aipcp/1481?ver=pdfcov>

Published by the [AIP Publishing](#)

Ultrasound Thermal Ablation System and Methods for Treatment of Breast Cancer

O. D. Kripfgans, A. Covert, F. R. Padilla, J. B. Fowlkes,
M. L. Fabiilli, M. Moghaddam^a, P. L. Carson

Departments of Radiology and ^aElectrical Engineering, University of Michigan, Ann Arbor, MI

Abstract. The design and initial testing of an ultrasound system capable of targeting and treating breast cancer noninvasively is presented; this system can be used either in the prone position, thus compatible with MRI localization and microwave-assisted treatment, or in the mammographic geometry for improved localization. Two half-shell transducers with holes in the centers for 2D imaging arrays allow placement close to the chest wall around, or on either side of, the breast. To drive the pair of 149 element arrays, we are building and programming circuitry to output radiofrequency (RF) tone bursts at 1.5 MHz. The low frequency may allow aperture sharing with microwave antennas and yet is high enough for acoustic droplet vaporization at 4 MPa peak rarefactional pressure for pulse trains of 2 s at 1% duty factor and far less for CW exposures. Five Altera DE1 development boards individually output RF tone bursts through 64 programmable channels each. A MATLAB-based, graphical user interface controls the system. Acoustic output tests at low pressures on a few array elements and electrical characterization of all elements suggest the necessary pressures can be achieved with either half of the full 0.7 f-number array using inexpensive amplifiers.

Keywords: HIFU, Minimally Invasive Therapy, Transducer Array, FPGA

PACS: 43.80.Vj, 43.80.Sh

INTRODUCTION

This research is directed primarily toward eliminating the most severe limitation of high intensity focused ultrasound (HIFU), that is, very slow, and occasionally incomplete treatments, particularly for large, deep lesions, including those close to the chest wall. When inhomogeneous ultrasound attenuation or small, diffuse metastases are expected, combining HIFU and high intensity focused microwave (HIFW) may be advantageous. The use of two modalities might not be much more complex clinically than treatment with one modality. Here we address the ultrasound system and its potential operation in the mammographic geometry. We are gaining confidence that whole breast ultrasound imaging can be performed in this geometry with the images closely aligned to those from 3D mammography (digital breast tomosynthesis) [1, 2]. Coupling to the breast at a much lower frequency for HIFU and imaging the treatment with a 2D array should allow placement of the focus anywhere in the breast [3], including over tumors close to the chest wall, without substantial chest wall heating (Figure 1). We are also making progress with several other imaging modalities that are compatible with this geometry and capable of improving guidance and assessment of treatment, including microwave, speed of sound [4] and vascularity imaging [5, 6].

The development and testing of HIFU phased arrays is of great interest due to their therapeutic potential. While tissue ablation by HIFU has already gained approval by the FDA for the treatment of uterine fibroids, development continues on other possible applications that are less forgiving of incomplete treatment, such as thermal necrosis of malignant masses. Researchers are investigating how to maintain the focus of an array through or around aberrating structures, minimize damage to tissue surrounding the target area, safely increase focal power, and steer the focus in three-dimensional space.

Since HIFU can heat a relatively small volume of tissue at a time, this leads to long treatment times that are limited by the heating of overlying tissues. Ongoing work with microbubbles and HIFU has demonstrated the ability to greatly increase the local absorption of sound in the treated tissue volume with less absorption of overlying tissues in the beam paths. These microbubbles can be 1) created by very high intensity ultrasound; 2) injected as ultrasound contrast agents; 3) generated by acoustic vaporization, as planned in this work, of injected perfluorocarbon droplets only in the transducer focal zone [7].

In order to perform these techniques with a phased array, each element must have its own fully programmable driver channel. This allows the output from each element to be phased and adjusted. Each channel must have a source that generates the waveform, an amplification device, and in most cases, a matching circuit to raise the impedance of the driver circuit to equal that of the element.

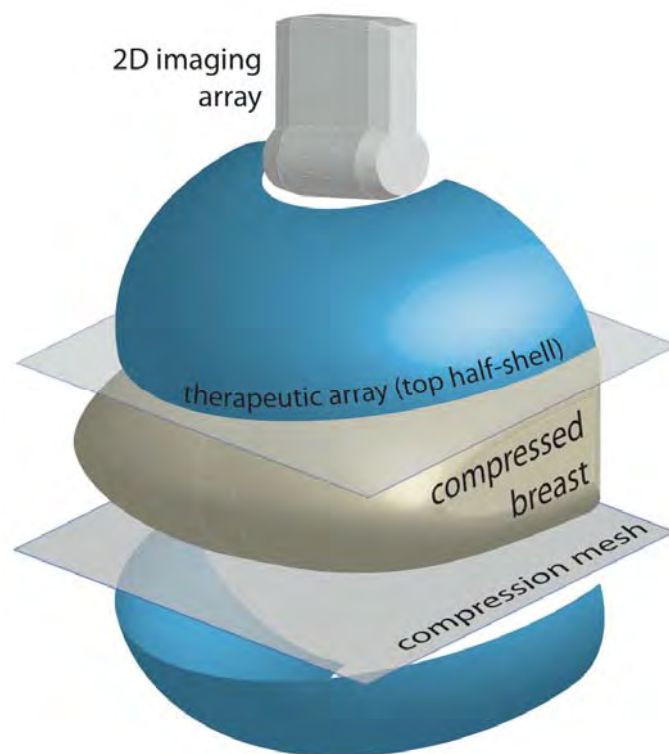


FIGURE 1. Schematic of a breast in the mammographic position with a therapeutic array above and below tissue to be treated. The use of half-shells allows for focusing and treatment close to the chest wall.

Similar projects utilize such systems to drive their arrays. Dr. Kullervo Hynynen's 1372-element, concentric array is driven by an in-house developed RF system with 2000 individual channels [8, 9]. This system is controlled by computer via a high speed digital interface (National Instruments' PCI-6534). Dr. Mathias Fink's quasi-random, 300-element array is driven by a 300-channel electronic driving system [10]. Three-hundred matching circuits are used to raise the impedance of the circuits to the impedance of the elements.

This paper describes the design, programming, fabrication, and evaluation of a RF driver system for a 298-element, concentric array (Imasonic SA, Besancon, France) composed of inexpensive Field-Programmable Gate Arrays (FPGA) development boards, amplifier boards, and matching circuitry. The system was designed with the following characteristics:

1. Fully programmable individual broadband channels capable of generating tone burst digital waveforms with 10 ns resolution
2. Frequency range of 1.5 kHz to 50 MHz
3. Up to 20 W per channel
4. Conductive Graphical User Interface (GUI)

MATERIALS AND METHODS

Therapeutic Array Design

A high-power, split-array design was pursued for combination of microwave and ultrasonic heating. Active elements range from 55 mm diameter (inner ring) to 130 mm diameter (outer ring). Figure 2 illustrates the split between the two half-shells resulting in 149 aperture elements each. Separability facilitates the incorporation of an additional microwave-based treatment device. Mechanical focusing is achieved by a spherical radius of curvature of 100 mm, yielding an f-number of 0.76. The elements are divided over seven rings spaced approximately 5.7 mm apart in a concentric fashion.

Signal Generation

Digital waveforms are generated by off-the-shelf FPGA control boards. Specifically, 6 development boards (DE1, Altera Corporation, San Jose, CA, Figure 3) were employed for triggering, synchronization, and signal generation. Software was developed in Verilog by use of Quartus II.

Each FPGA board can control a maximum of 64 ultrasound channels. Each channel can be controlled remotely for center frequency, number of transmitted waveform cycles, waveform delay for additional electronic focusing, and duty-factor for pulse-width-modulation waveform amplitude shaping. These values are communicated to the board via read/write USB (universal serial bus) from a control computer. Transmission is triggered either by software control or an external TTL input (3.3 V_{pp}, ≥ 50 ns, positive edge). For use in external devices such as an oscilloscope, a trigger-out signal is provided (3.3 V_{pp}, 2 μ s, positive edge).

Two additional user programmable channels are available. A master/client setup synchronizes both triggering as well as FPGA clock cycles. One master board is employed to provide a common 100 MHz digital clock signal for the signal generating client boards as well as for triggering. Waveform-delay as well as transmit frequency selection is bound to 10 ns resolution. Sixteen bit counters allow for up to 650 μ s time-delay between channels as well as 65,000 cycle waveforms. Very long HIFU pulse trains are accommodated by repeated trigger events. This allows for up to 85 s quasi continuous excitation.

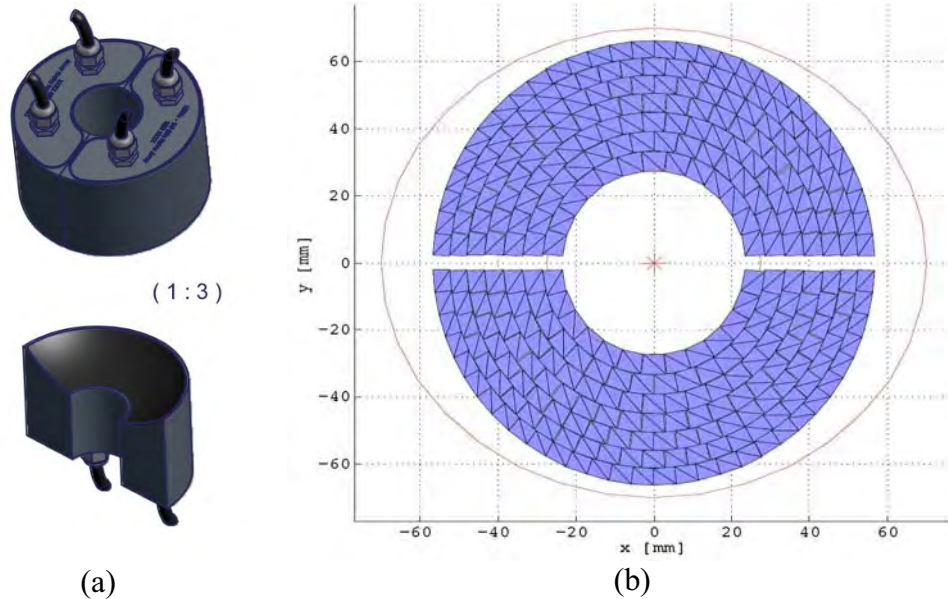


FIGURE 2. (a) Design photos of the therapeutic array transducer. Each half-shell contains 7 concentric rings with a total of 149 transducer elements. (b) A broad focus at a distance of 10 cm is achieved by shaping the array in an elliptical fashion as shown here (Note: each element consists of two triangular picture elements.)

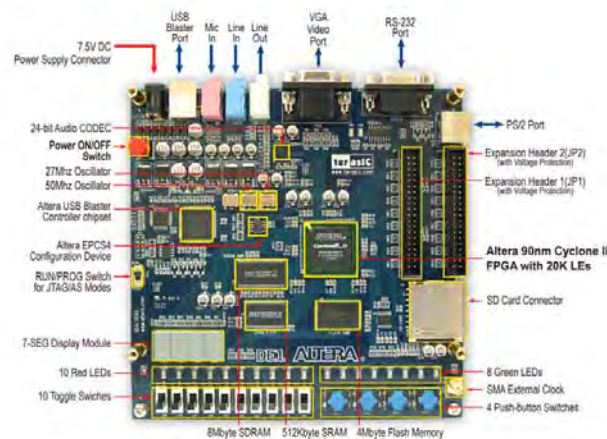


FIGURE 3. Employed off-the-shelf FPGA development hardware. PC to FPGA communication is facilitated by the use of an USB protocol. Digital waveforms are transmitted to the amplifier electronics via the general purpose I/O expansion headers.

User Interface

Two-way USB communication between a host computer and all 6 FPGA boards is facilitated by an in-house DLL driver and MATLAB (MathWorks, Natick MA). A conducive graphical user interface allows for channel-by-channel waveform control as described above, triggering, and motorized 3D positioning of the array transducer (6K4 Motion Controller, Parker Hannifin Corporation, Cleveland, Ohio).

Acoustic Measurements

The acoustic output was sensed with a needle hydrophone (HNC-1500, Onda Corporation, Sunnyvale, CA) and captured using a digital oscilloscope (WaveJet 324A, LeCroy Corporation, Chestnut Ridge, NY).

RESULTS

Non-amplified signal generation produced a 60 dB signal-to-noise waveform with a 200 kPa peak-to-peak pressure, for a 3.3 Vpp input of a 10 cycle tone burst (1.5 MHz center frequency). The generated RF waveforms show a root-mean-square jitter of 2.5 ns with a standard deviation of 1.9 ns, well under the inherent 10 ns system clock resolution.

Peak-Output Performance

Short-time performance allowed for up to 18 Watts of electrical power per channel and a usual efficiency of 70%. Typically, 15-cycle tone bursts were transmitted with up to 1 kHz pulse repetition rates. The single-channel performance of amplified rf-signals yielded 130 kPa peak-to-peak in the natural focus of the array. Assuming linear superposition of 298 elements, this would correspond to approximately 40 MPa peak-to-peak, not taking nonlinear propagation into account.

Time-Average Power Performance

Long-time performance was tested for up to 1 Watt of electrical power per channel. Trigger signals were employed to ensure >98% duty cycle tone-burst output for 5 s. Single-channel performance yielded 17.5 kPa peak-to-peak acoustic output. Again, assuming linear superposition of 298 elements, this would correspond to >5 MPa peak-to-peak pressure wave.

CONCLUSIONS

In general, HIFU arrays are not innovative, though a split ring design is new and will be useful for operation close to the chest wall. The driving circuits employ standard, non-expensive, off-the-shelf components. Commercial signal generators that

would meet the aforementioned requirements would likely be more expensive. National Instrument's PCI-6542 digital waveform generator provides 32 digital output channels with an inter-channel jitter of 0.6 ns for \$4999 [9]. The FPGA design described in this paper will be 1/10 of that cost. The obtained acoustic output pressures are acceptable for both HIFU as well as hyperthermia mode excitation.

ACKNOWLEDGEMENTS

This work is supported in part by DOD/BCRP W81XWH-10-1-0730 (BC095397).

REFERENCES

1. Sinha SP, Hooi FM, Syed Z, Pinsky R, Thomenius K, Carson PL, "Machine learning for noise removal on breast ultrasound images," 2010 IEEE Int. Ultrasonics Symp., Inst. Elect. Electr. Engrs., Number, San Diego (Oct. 10-13, 2010).
2. Carson PL, "Multimodality Breast Imaging Systems: Tomo/Ultrasound/Optics, Ultrasound/Other," Conference Name, Pages, recorded presentation with slides, (Jul 18-24, 2010). <http://www.associationarchives.com/SITES/aapm>.
3. Hooi FM, Thomenius K, Fisher R, Carson P, "Hybrid Beamforming and Steering with Reconfigurable Arrays," IEEE Trans Ultrason. Ferroelectr. Freq. Control 57(6), 1311-1319, PMC2914568, (2010).
4. Wodnicki R, Thomenius K, Ming Hooi F, Sinha SP, Carson PL, Lin DS, Zhuang X, Khuri-Yakub P, Woychik C, "Large area MEMS based ultrasound device for cancer detection," Nuclear Instruments and Methods in Physics Research, Section A: Accelerators, Spectrometers, Detectors and Associated Equipment, (2011).
5. LeCarpentier GL, Roubidoux MA, Fowlkes JB, Krucker JF, Hunt KA, Paramagul C, Johnson TD, Thorson NJ, Engle KD, Carson PL, "Suspicious breast lesions: assessment of 3D Doppler US indexes for classification in a test population and fourfold cross-validation scheme," Radiology 249(2), 463-470, PMC2657861, (2008).
6. Wang X, Fowlkes JB, Cannata JM, Hu C, Carson PL, "Photoacoustic imaging with a commercial ultrasound system and a custom probe," Ultrasound Med. Biol. 37(3), 484-492, (2011).
7. Zhang M *et al.* Manuscript submitted to Academic Radiology.
8. Junho S, Kullervo H. A 1372-element Large Scale Hemispherical Ultrasound Phased Array Transducer for Noninvasive Transcranial Therapy. 8th Int Symp Therap Ultras. 1113, pp. 377-81 (2009).
9. Sokka SD, Juste J, Hynynen K. Design and Evaluation of Broadband Multi-Channel Ultrasound Driving System for Large Scale Therapeutic Phased Arrays. Ultrasonics, 2003 IEEE Symposium on (Oct. 5-8 2003) (2) pp.1638-41.
10. Pernot M, Aubry JF, Tanter M, Marquet F, Montaldo G, Boch AL, Kujas M, Seilhean D, Fink M. High Power Phased Array Prototype for Clinical High Intensity Focused Ultrasound : Applications to Transcostal and Transcranial Therapy. Conf Proc IEEE Eng Med Biol Soc.; 2007, pp. 234-7.

Research Article

Microwave Breast Imaging System Prototype with Integrated Numerical Characterization

Mark Haynes, John Stang, and Mahta Moghaddam

*Applied Physics Program, Basic Radiological Sciences Ultrasound Group, and Radiation Laboratory,
Department of Electrical Engineering and Computer Science, University of Michigan, Ann Arbor, MI 48109-2122, USA*

Correspondence should be addressed to Mark Haynes, mshaynes@umich.edu

Received 2 October 2011; Accepted 7 December 2011

Academic Editor: Paul Meaney

Copyright © 2012 Mark Haynes et al. This is an open access article distributed under the Creative Commons Attribution License, which permits unrestricted use, distribution, and reproduction in any medium, provided the original work is properly cited.

The increasing number of experimental microwave breast imaging systems and the need to properly model them have motivated our development of an integrated numerical characterization technique. We use Ansoft HFSS and a formalism we developed previously to numerically characterize an S-parameter-based breast imaging system and link it to an inverse scattering algorithm. We show successful reconstructions of simple test objects using synthetic and experimental data. We demonstrate the sensitivity of image reconstructions to knowledge of the background dielectric properties and show the limits of the current model.

1. Introduction

A number of experimental systems for microwave breast imaging have been developed in recent years. These systems test full-wave inverse scattering algorithms [1–4] as well as synthetic aperture beam focusing techniques [5]. While imaging algorithms abound in the literature, techniques to properly model, characterize, and calibrate these systems have lagged behind algorithm development. Investigators have started to identify characterization as a major task, which must be addressed in order to fully evaluate the efficacy of microwave imaging for breast cancer detection. Part of this evaluation involves separating modeling errors from intrinsic algorithm artifacts in the final images. Thus, there is a need for accurate models of experimental systems, as well as methods that efficiently incorporate these models into the imaging algorithms.

The task of characterizing a microwave breast imaging system for inverse scattering, as compared to a free-space system, is complicated by several factors. Specifically, the antennas are not isolated in the background media but exist as part of the surrounding structure. Also, compact arrangements of many antennas create a cavity-like imaging geometry, and the transmitter incident fields include all background multiple scattering. Finally, the antennas and

object are in each others near-fields, so object-cavity scattering should be modeled.

In trying to characterize breast imaging systems, investigators have turned to full numerical simulation. The antenna cavity in [6] was modeled using Ansoft HFSS and only used for antenna design and sensitivity analysis. In [7], dipole sources of an inverse scattering experiment were modeled with HFSS and calibration constants used to scale the antenna incident fields. HFSS has also been used to obtain antenna incident fields in a near-field and open, antenna setup [8]; however, ad hoc methods have been used to calibrate the scattered field S-parameter data for the inverse scattering algorithm. In more recent work [9], CST Microwave Studio was used to study and tune antenna performance in a breast imaging cavity. Also, finite-volume time-domain solvers of [10] modeled wide-band antennas for time-domain beam focusing. The most complete work to date is [11], where an FEM forward solver is used to simulate the entire breast in the presence of the antennas, but computational complexity remains a challenge. Despite the growing use of numerical solvers to model breast imaging systems, there has been no clear or formal way of incorporating the results from full-wave numerical models into the imaging algorithms.

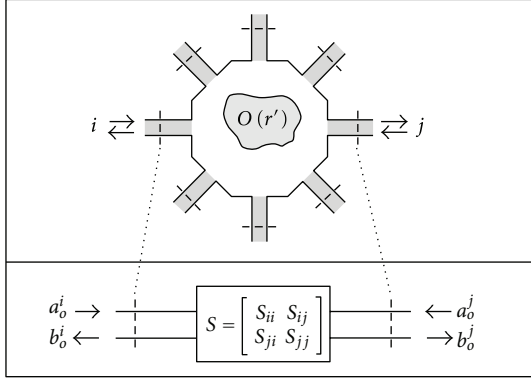


FIGURE 1: Microwave network model of cavity and scattering object. S-parameters are measured between the reference planes on the transmission lines.

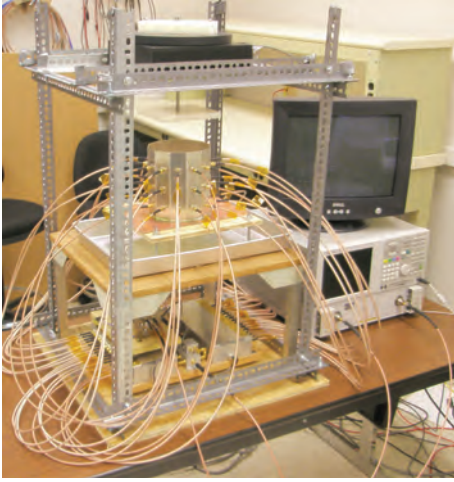


FIGURE 2: Breast imaging system prototype. The imaging cavity is connected to the VNA through a solid-state switching matrix. A rotator is mounted above and turns suspended objects for multiple transmitter views.

The task of characterizing any inverse scattering system can be divided into three parts: (1) determining the incident fields produced by the antennas in the absence of the object, (2) determining the background dyadic Green's function, that is, modeling the interactions between the object and its surroundings if necessary, and (3) linking the volume integrals in the imaging algorithms to measurable transmit and receive voltages. The purpose of this paper is to show how we use HFSS and a formalism we developed in previous work [12] to solve parts (1) and (3) of this characterization problem, in order to make a numerical characterization and inverse scattering algorithm consistent with an S-parameter based prototype breast imaging system.

The inverse scattering algorithm we use is the Born iterative method (BIM) with multivariate-covariance cost function [13–15]. This cost function allows us to experimentally choose the regularization parameters based on our prior knowledge of system noise and expected range of permittivities. The forward solver used in the BIM requires

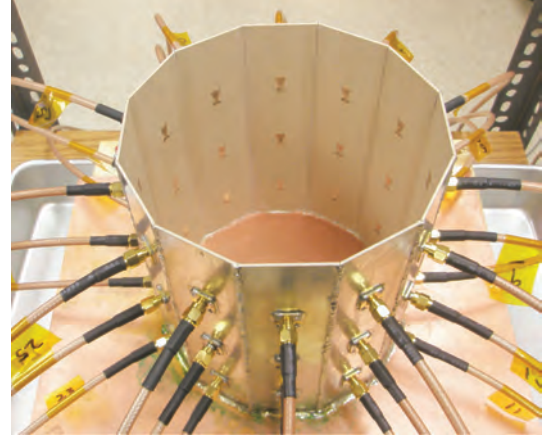


FIGURE 3: Imaging cavity. Twelve panels with three bow-tie antennas each are solder together and to a conducting plate.



FIGURE 4: HFSS CAD model of the imaging cavity. Twelve panels contain three bow-tie antennas each. The bottom of the cavity is PEC, it is filled with the coupling fluid up to the visible line, and the top surface radiates to air.

the background dyadic Green's function and finding it constitutes part (2) of the characterization problem mentioned above. For convenience we use the lossy free-space dyadic Green's function and give some numerical and experimental justification for this. Fully modeling the multiple scattering between the breast and the imaging structure in the forward solver is not trivial and we discuss it in The Appendix.

We validate our methods with a combination of simulation and experiment. We first present the formalism of [12] in the context of cavity problems. We then explain our experimental setup, which consists of a cylindrical imaging cavity with printed antennas, solid-state switching matrix, and water/oil coupling medium. The HFSS numerical model

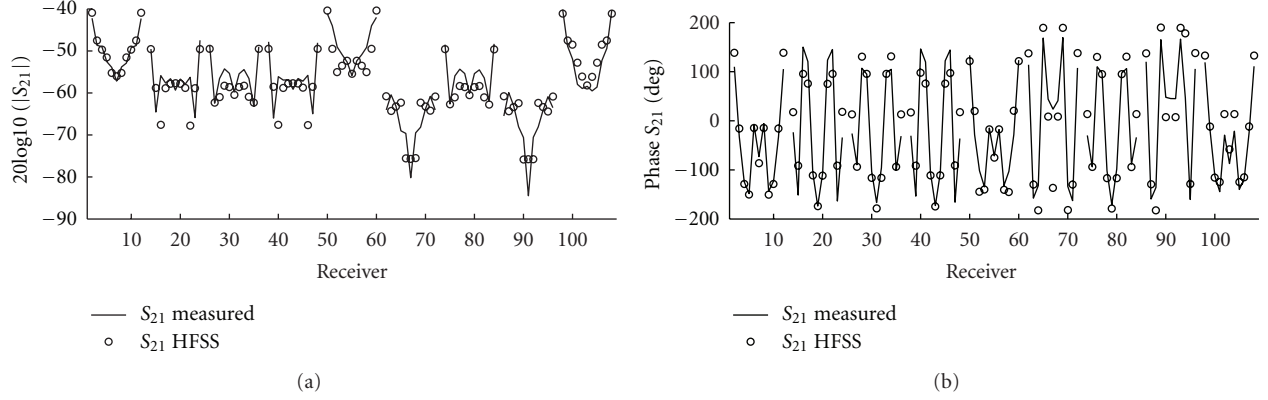


FIGURE 5: Measured and simulated magnitude and phase of incident S_{21} between each of the three transmitting antennas and all receivers. Solid: measured. Dots: HFSS. The groupings from left to right are the eleven receivers of each level (middle, top, and bottom), repeated for the three transmitters (middle, top, and bottom), plotted counterclockwise when viewed from above for a given receiver level. For example, data 38 : 48 are middle receivers and top transmitter. The magnitude and phase agree best for transmitters and receivers on the same level (i.e., data 1 : 11, 50 : 60, and 98 : 108).

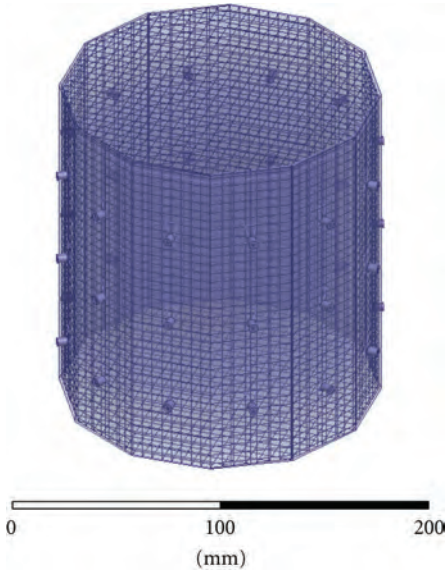


FIGURE 6: HFSS CAD model of the imaging cavity with mesh of unassigned sheets to constrain the adapting meshing of HFSS for field interpolation. Sheets are spaced every 5 mm in each direction.

is presented and the simulation results are compared to those of experiment. We form 3D images of the relative permittivity and conductivity using both HFSS synthetic data and experimental data for simple targets. We also present findings on the sensitivity of image reconstructions to the accuracy of modeling the background electrical properties.

Future work includes continuing the validation of our methodology, experimentally imaging more realistic breast phantoms, designing a hemispherical imaging cavity, investigating practical solutions to modeling the breast-cavity scattering interactions, and developing a clinical imaging system.

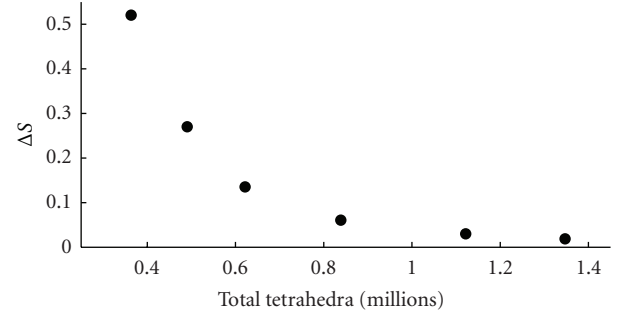


FIGURE 7: HFSS convergence with number of tetrahedra for each adaptive meshing step.

2. Formulation with Source Characterization

2.1. Traditional Volume Integral Equations. The electric field volume integral equation (VIE) for an inhomogeneous distribution of permittivity and conductivity is given by

$$\mathbf{E}(\mathbf{r}) = \mathbf{E}_{\text{inc}}(\mathbf{r}) + k_o^2 \int \overline{\mathbf{G}}(\mathbf{r}, \mathbf{r}') \cdot \left(\delta\epsilon(\mathbf{r}') + \frac{i\delta\sigma(\mathbf{r}')}{\epsilon_b\omega} \right) \mathbf{E}(\mathbf{r}') dV', \quad (1)$$

where $\mathbf{E}(\mathbf{r})$ and $\mathbf{E}_{\text{inc}}(\mathbf{r})$ are the total and incident fields, respectively, and \mathbf{r} is the position vector. The lossless background wave number is given by $k_o^2 = \omega^2\mu_o\epsilon_b$, where the background permittivity is $\epsilon_b = \epsilon_o\epsilon_{rb}$ with relative permittivity ϵ_{rb} . The object contrast functions are defined:

$$\begin{aligned} \epsilon_b\delta\epsilon(\mathbf{r}) &= \epsilon(\mathbf{r}) - \epsilon_b, \\ \delta\sigma(\mathbf{r}) &= \sigma(\mathbf{r}) - \sigma_b, \end{aligned} \quad (2)$$

where σ_b is the background conductivity. The quantity $\delta\epsilon(\mathbf{r})$ is unitless and $\delta\sigma(\mathbf{r})$ is an absolute measure of conductivity with units of Siemens per meter and $\overline{\mathbf{G}}(\mathbf{r}, \mathbf{r}')$ is the background dyadic Green's function.

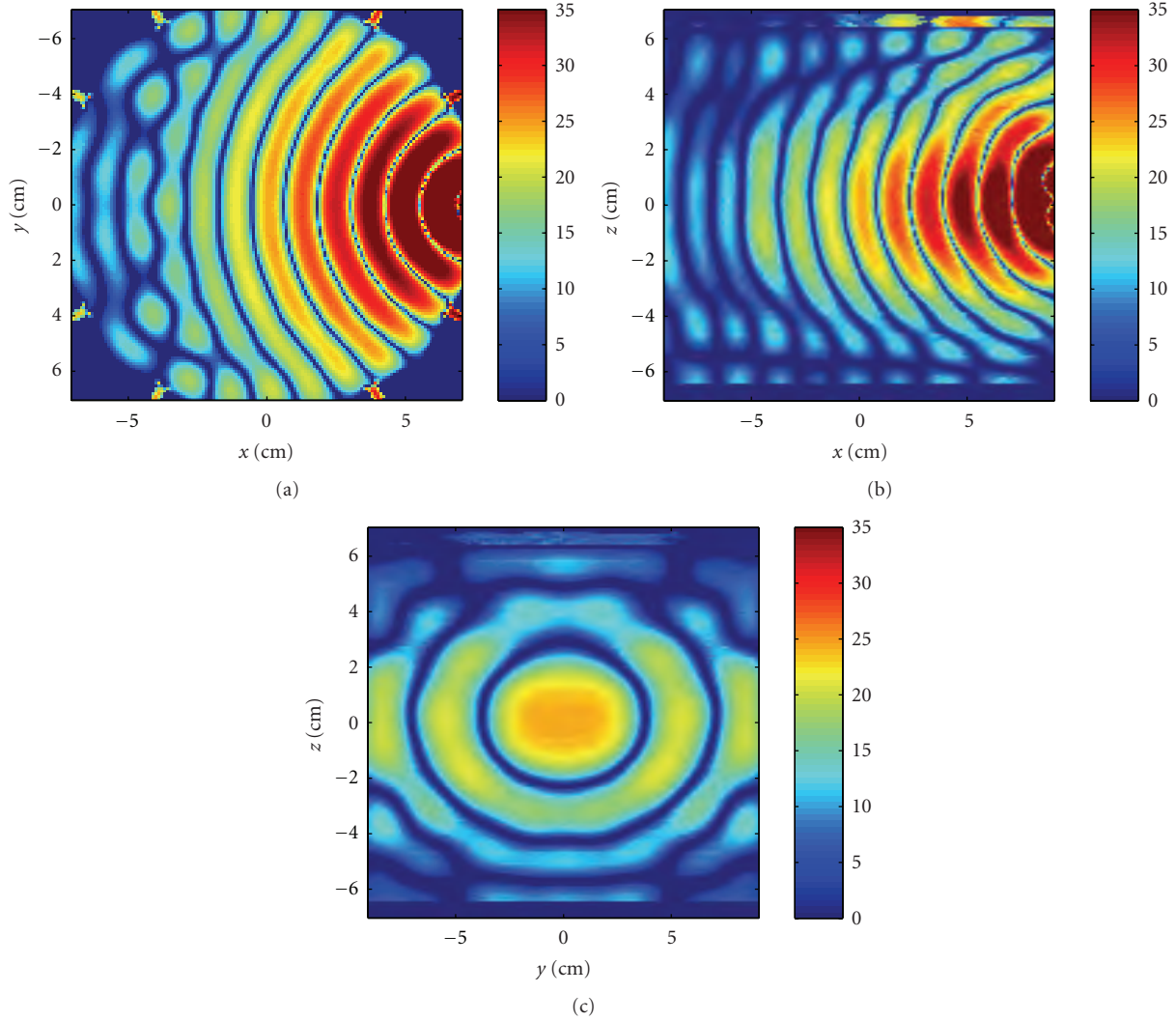


FIGURE 8: Crosscuts through the center of the cavity of the z -component of the incident electric field due to the middle transmitter. The scale is $20\log_{10}(|\text{Re}\{E_{z,\text{inc}}\}|)$ of the unnormalized field. (a) Horizontal x - y , and (b) vertical x - z , and (c) vertical y - z planes.

Defining the scattered field as

$$\mathbf{E}_{\text{sca}}(\mathbf{r}) = \mathbf{E}(\mathbf{r}) - \mathbf{E}_{\text{inc}}(\mathbf{r}) \quad (3)$$

and restricting the observation point \mathbf{r} to points outside the object region in (1), we can write the VIE for the scattered field concisely as

$$\mathbf{E}_{\text{sca}}(\mathbf{r}) = \int \bar{\mathbf{G}}(\mathbf{r}, \mathbf{r}') \cdot \mathbf{O}(\mathbf{r}') \mathbf{E}(\mathbf{r}') dV', \quad (4)$$

where we define the following object function:

$$\mathbf{O}(\mathbf{r}) = k_o^2 \left(\delta\epsilon(\mathbf{r}) + i \frac{\delta\sigma(\mathbf{r})}{\epsilon_b \omega} \right). \quad (5)$$

In the context of inverse scattering, (1) represents the solution to the wave equation in the object domain, while (4) relates the material contrasts to scattered field measurements taken outside the object domain. Depending on the inversion algorithm, these two equations are used in combination to

recover both the contrasts and the total fields. Traditionally, (1) and (4) are used as they are to develop inverse scattering algorithms.

2.2. Integral Equations for Cavity S-Parameter Measurements.

In a previous work [12], we showed that it is possible to transform (1) and (4) so that they are consistent with an S-parameter-based measurement system. We showed that the resulting equations were valid for both free-space and cavity-like geometries and went on to validate the free-space case with an inverse scattering experiment [13]. Here, we will summarize the results for a cavity geometry.

Consider the cavity depicted in Figure 1. An object to be imaged is placed in the middle of the cavity. The cavity is filled with a background material having a permittivity and conductivity of ϵ_b and σ_b , respectively. The cavity is lined with radiating apertures, which could be antennas. Each aperture has its own feeding transmission line and S-parameter reference plane.

We define the normalized incident and total fields throughout the cavity due to a transmitting aperture as

$$\begin{aligned} \mathbf{e}_{\text{inc}}(\mathbf{r}) &= \frac{\mathbf{E}_{\text{inc}}(\mathbf{r})}{a_o}, \\ \mathbf{e}(\mathbf{r}) &= \frac{\mathbf{E}(\mathbf{r})}{a_o}, \end{aligned} \quad (6)$$

where a_o is the transmit voltage measured with respect to the S-parameter reference plane. The normalized incident field captures all background multiple scattering not present between the object and the cavity.

Let transmitting apertures be indexed with i and those receiving indexed with j . We can write (1) in terms of the normalized incident and total fields produced by a transmitter by dividing both sides by $a_{o,i}$:

$$\mathbf{e}_i(\mathbf{r}) = \mathbf{e}_{\text{inc},i}(\mathbf{r}) + \int \bar{\mathbf{G}}(\mathbf{r}, \mathbf{r}') \cdot \mathbf{O}(\mathbf{r}') \mathbf{e}_i(\mathbf{r}') dV'. \quad (7)$$

This is the integral equation we will use to represent the forward scattering solution. The normalized total field is the field solution in the object domain and, with the appropriate dyadic Green's function for the cavity, includes the scattering interactions between the object and the cavity.

In [12] we showed how to transform the scattered field volume integral equation given by (4) into one that predicts S-parameters. This new integral operator allows us to directly compare model predictions to measurements in the inversion algorithm. The two-port scattered field S-parameter, $S_{ji,\text{sca}}$, measured between the transmission line reference planes of two apertures in the presence of an object is given by

$$S_{ji,\text{sca}} = \int \mathbf{g}_j(\mathbf{r}') \cdot \mathbf{O}(\mathbf{r}') \mathbf{e}_i(\mathbf{r}') dV', \quad (8)$$

where $\mathbf{e}_i(\mathbf{r})$ is the normalized total object field produced by the transmitter and $\mathbf{g}_j(\mathbf{r})$ is the vector Green's function kernel for the receiver. It was also shown in [12] by reciprocity that $\mathbf{g}_j(\mathbf{r})$ is related to the normalized incident field of the receiver as

$$\mathbf{g}_j(\mathbf{r}) = -\frac{Z_o^j}{2i\omega\mu} \mathbf{e}_{\text{inc},j}(\mathbf{r}), \quad (9)$$

where ω is the operating frequency in radians, μ is the background permeability, and Z_o^j is the characteristic impedance of the receiver transmission line.

Equations (7) and (8) are the integral equations we will use for the inverse scattering algorithm. They consistently link the electric field volume integral equations to an S-parameter measurement system. We need only to determine the normalized incident fields in the object domain and the background dyadic Green's function; no other step is required to characterize the system, except to calibrate the transmission line reference planes.

Lastly, in experiment, we never measure scattered field S-parameters directly but obtain them by subtracting the S-parameters for the total and incident fields:

$$S_{ji,\text{sca}} = S_{ji,\text{tot}} - S_{ji,\text{inc}}, \quad (10)$$

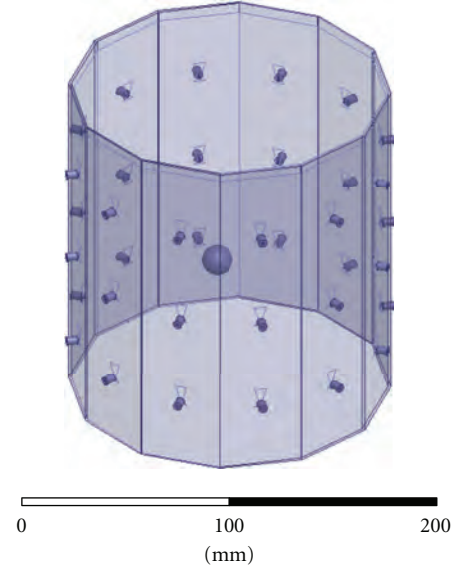


FIGURE 9: HFSS model of a simple sphere used to generate synthetic scattered field S-parameters.

where $S_{ji,\text{inc}}$ is measured in the absence of the object and $S_{ji,\text{tot}}$ is measured in the presence of the object.

2.3. Determining $\mathbf{e}_{\text{inc}}(\mathbf{r})$ and $\bar{\mathbf{G}}(\mathbf{r}, \mathbf{r}')$. The normalized incident field is required in both (7) and (9) and is required for every aperture. We can either measure it experimentally or estimate it with simulation. Experimentally mapping the fields requires proper probe calibration and has the added complication in a cavity that the probe-wall interactions cannot be neglected. An alternative approach, the one we adopt for this paper, is to estimate the normalized incident field with simulation. This can be done provided that we have a computer aided design (CAD) model that accurately represents the cavity. It is also possible in simulation to model the feeding transmission lines and line voltages in order to assign an S-parameter reference plane that is identical to the reference plane used by a vector network analyzer for the physical measurement. We will show how we use Ansoft HFSS to accomplish this.

As stated in the introduction, determining the background dyadic Green's function is nontrivial, especially for arbitrary cavity geometries. Despite this, for the immediate investigation, we use the free-space dyadic Green's function under the condition that the background medium is extremely lossy. Though not strictly correct, this approximation is convenient provided the multiple scattering throughout the cavity is limited by the background loss. It also allows us, for the time being, to retain use of an FFT-based volumetric forward solver. We give examples later evaluating this assertion. There are several approaches for determining or approximating the background dyadic Green's function for arbitrary geometries, which we discuss in The Appendix and leave for future work.

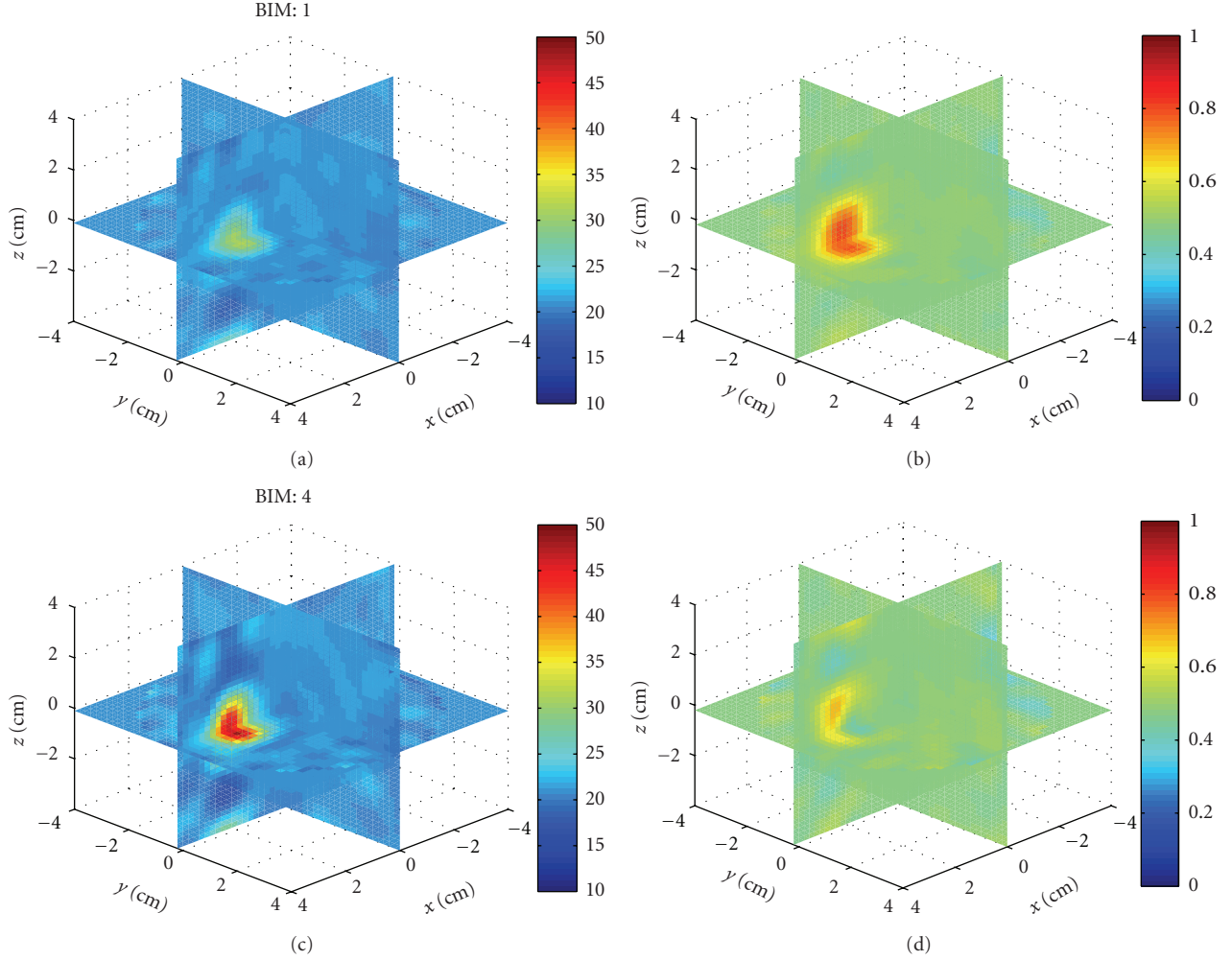


FIGURE 10: Reconstructions of a single sphere $(\epsilon_r, \sigma) = (40, 1)$ located at $(x, y, z) = (0, 0, 2 \text{ cm})$ of Example 1. (a) and (c) and (b) and (d) Relative permittivity and conductivity, respectively. (a) and (b) is the Born approximation. (c) and (d) is BIM iteration 4. Here, iterations help retrieve the relative permittivity in (c), but the Born approximation yielded better conductivity in (b).

3. Born Iterative Method

The imaging algorithm we use is the Born iterative method (BIM) [16–19]. The BIM successively linearizes the nonlinear problem by alternating estimates of the contrasts and the object fields according to the following algorithm.

- (1) Assume the object fields are the incident fields (Born approximation).
- (2) Given the measured scattered field data, estimate the contrasts with the current object fields by minimizing a suitable cost function.
- (3) Run the forward solver with current contrasts. Store the updated object field.
- (4) Repeat step 2 until convergence.

This algorithm and its implementation are described in detail in our previous work [13], where we successfully formed images of dielectric constant for plastic objects in a free-space experiment. This was done using the same BIM

and the integral equations for S-parameters given above using antennas characterized with HFSS.

We use the multivariate covariance-based cost function of [15]. The Gaussian interpretation of this cost function allows us to experimentally justify the values we use to regularize it by our *a priori* knowledge of the experimental noise and range of contrast values. For the forward solver, because we use the lossy free-space dyadic Green's function to model the internal scattering, we use the BCGFFT [20–22], which we have validated with analytic solutions. In the examples that follow, we found that 4 BIM iterations were repeatedly sufficient for the data residual and object to converge.

4. Breast Imaging System Prototype

The breast imaging system prototype we built is shown in Figure 2. The imaging structure is a cavity, shown in Figure 3, that was created by soldering twelve vertical panels of microwave substrate together and soldering the collection to a conducting base. Opposite panels are separated by 15 cm,

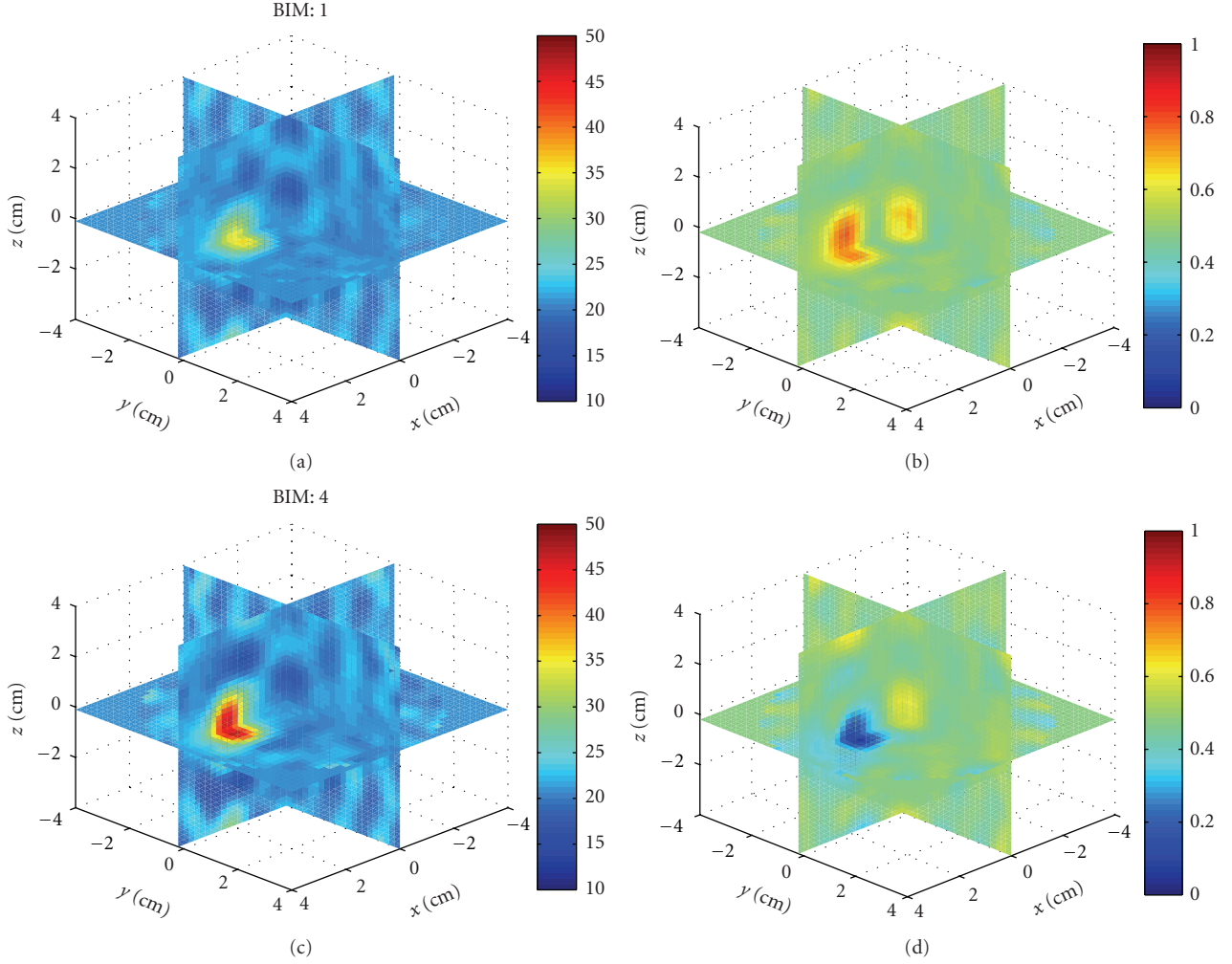


FIGURE 11: Reconstructions of a single sphere $(\epsilon_r, \sigma) = (40, 0)$ located at $(x, y, z) = (0, 0, 2 \text{ cm})$ of Example 1. Born iterations helped retrieve the relative permittivity in (c) and are essential in recovering the conductivity in (d).

and the cavity is 17 cm long. Three antennas are printed on each panel for a total of 36 antennas. In the prototype, the three antennas of one panel are used as transmitters, while all other antennas are receivers. The transmit antennas are switched with a Dowkey SP6T electromechanical switch. The receivers are connected through an SP33T solid-state switching matrix that was designed and assembled in-house. 2-port S-parameter measurements were taken with an Agilent PNA-5230A vector network analyzer (VNA) at 2.75 GHz between each transmitter and any one receiver. This frequency was chosen as a compromise between resolution and switch performance, which rolls off above 3 GHz. A rotator was mounted above the cavity and aligned in the center of the cavity. Test objects are suspended with fishline and rotated to provide multiple transmitter views.

4.1. Liquid Coupling Medium. We expect breast tissue to have a relative permittivity between 10 and 60 [23]. Without a matching medium, much of the incident power would be reflected at the breast/air interface reducing the sensitivity of the system [24]. Also, the contrast ratio between the object

and the background would be too high for the BIM inverse scattering algorithm to converge.

The matching medium we use is an oil/water emulsion developed in a previous work [25]. This fluid is designed to balance the high permittivity and high conductivity of water with the low permittivity and low conductivity of oil, in order to achieve a fluid with moderate permittivity while limiting loss as much as possible. We are also able to tune the microwave properties of this emulsion by adjusting the oil/water ratio. We aimed for a relative permittivity value around 20, which brings the maximum permittivity contrast to about 3:1. The fluid mixture we used was 65%/35% oil/water.

The electrical properties of the fluid were measured using the Agilent 85070E slim form dielectric probe. The measured properties at 2.75 GHz were $(\epsilon_r, \sigma) = (19, 0.34)$. Relative permittivity is unitless; the units of conductivity used throughout the paper are Siemens/m. When using this value in the numerical model (presented below) the magnitude of cross-cavity S_{21} required some adjustment when compared to the measurements. We obtained the best

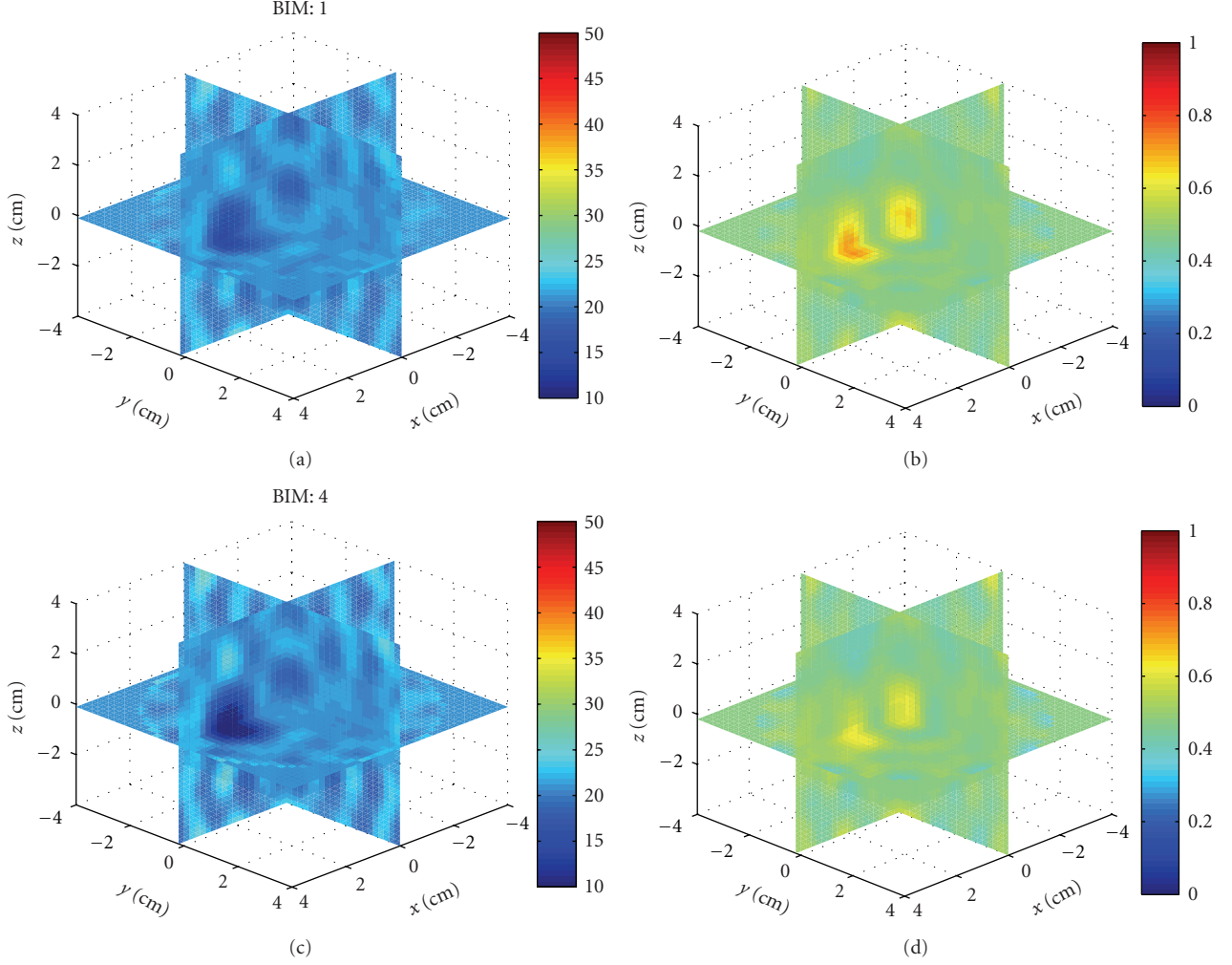


FIGURE 12: Reconstructions of a single sphere $(\epsilon_r, \sigma) = (10, 1)$ located at $(x, y, z) = (0, 0, 2 \text{ cm})$ of Example 1. Born iterations helped the recovery of the low permittivity in (c), but at the expense of the correct conductivity value which was better with the Born approximation in (b).

model agreement for $(\epsilon_r, \sigma) = (21, 0.475)$, which are the values we use throughout the paper. We suspect that the probe area may be too small to accurately measure the bulk properties of the mixture, but the fluid otherwise appears homogeneous for propagation at 2.75 GHz. We are still investigating this effect.

When taking data, we fill the cavity with the coupling fluid to a height that is 0.5 cm below the top edge. This fluid height is accounted for in the numerical model. Any fluid displacement from adding or removing test objects is compensated in order to keep the height constant. We have also found the emulsion to be stable over the course of measurements, which we confirmed by comparing transmission measurements before and after we take data for imaging.

4.2. Antenna Design. The antennas are bow-tie patch antennas, similar to the antennas in [6, 26]. They are of single frequency and vertical polarization. The bow-tie antenna was chosen to give more degrees of freedom to help

impedance match the antenna to the coupling fluid. The vertical polarization was chosen for best illumination of the object and other antennas in the cylindrical geometry. The substrate material is Rogers RO3210, with 50 mil thickness and reported dielectric constant of 10.2. The antennas were originally designed to operate at 2.8 GHz in the cavity filled with a fluid with $(\epsilon_r, \sigma) = (24, 0.34)$; however, after iterating, we found best performance at 2.75 GHz in a fluid of $(\epsilon_r, \sigma) = (21, 0.475)$.

4.3. System Parameters. In determining the system noise and isolation requirements, the minimum expected signal determines the required noise level, and the maximum relative magnitude between signals on adjacent channels determines the required switch path isolation. From previous numerical studies of cavity-like breast imaging with similar emulsion properties [27], we expect the scattered field S_{21} magnitude of small inclusions to be in the range from -100 to -50 dB, and so the relative signal strength between adjacent antennas could differ by as much as -50 dB. This

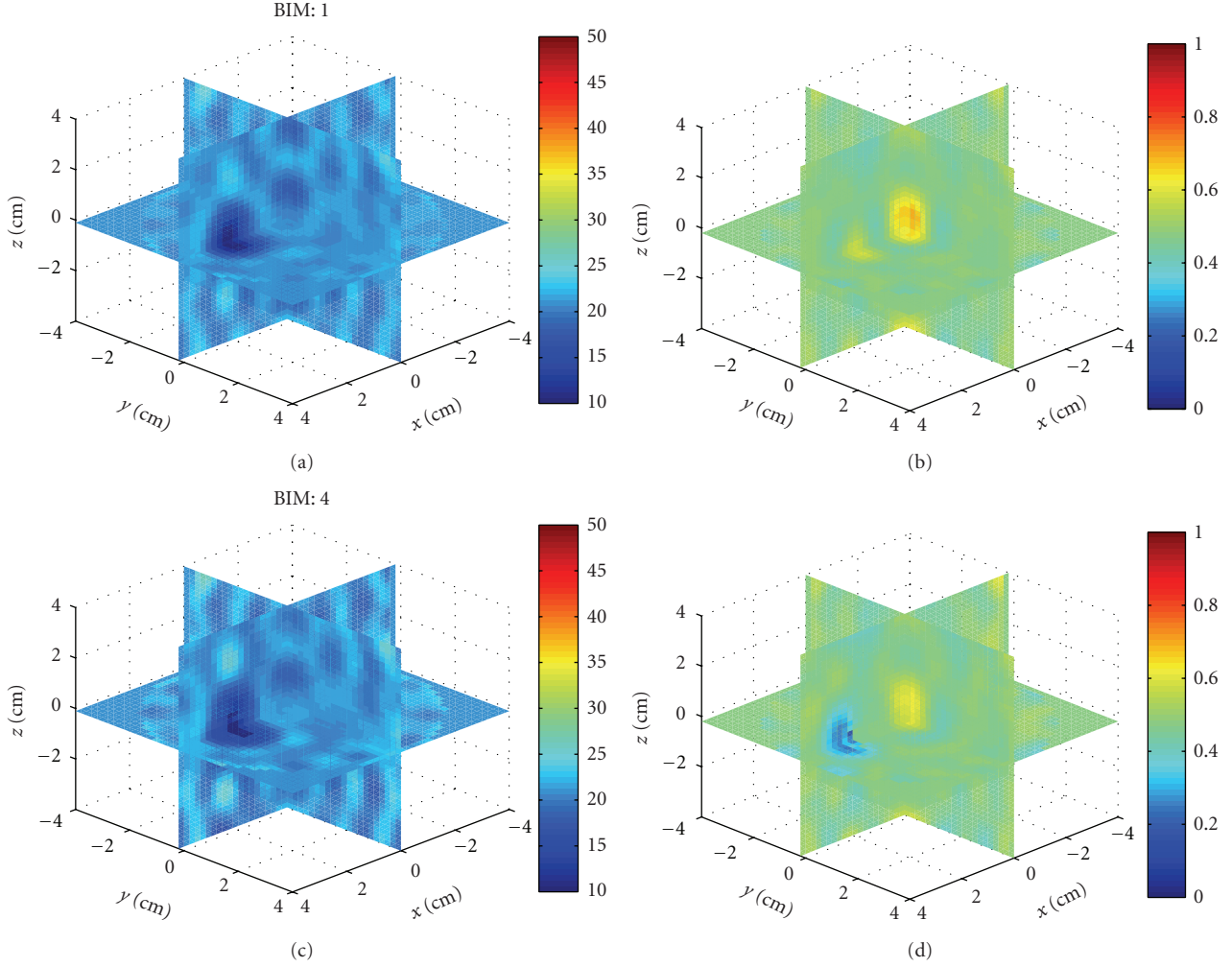


FIGURE 13: Reconstructions of a single sphere $(\epsilon_r, \sigma) = (40, 0)$ located at $(x, y, z) = (0, 0, 2 \text{ cm})$ of Example 1. Born iterations helped bring out the proper conductivity value in (d).

means that the noise of our system must be less than -100 dB , which is achievable by our VNA with averaging and an IF bandwidth of 100 kHz or less. Also, the switching matrix paths must be isolated by at least -50 dB .

4.4. Switching Matrix. The receivers were connected through a SP33T solid-state switching matrix that was designed and assembled in-house. The matrix consists of two custom SP16T solid-state switching matrices and a cascaded pair of Minicircuits SPDT switches. Each SP16T switch is composed of two layers of SP4T Hittite HMC241QS16 nonreflective switches, which are buffered at the output by a third layer consisting of a single SPDT Hittite HMC284MS8GE on each path. The buffer layer was added to increase interpath isolation. The switch is controlled with an embedded digital board and computer parallel port. The operating band of the switching matrix is between $0.1\text{--}3 \text{ GHz}$. The overall loss of a path through the SP33T matrix is no worse than 8 dB across the band. We measured the switch path isolation to be better than -55 dB between $1\text{--}3 \text{ GHz}$, which meets the criteria above.

By separating the transmitter and receiver switching, the isolation between these two operation modes is dictated by the network analyzer and the cables. In more realistic systems, where the antennas are dual mode and so object rotation is not necessary, the isolation requirements are more stringent, because the transmit amplitude will be orders of magnitude larger than the scattered field.

4.5. VNA Calibration. Two-port VNA calibrations were accomplished between each transmitter and each receiver. The S-parameter reference planes were calibrated to the points where the cables connect to the antenna. These reference planes are identical to those in the HFSS CAD model (presented below). While calibrating, we left the unused ports open with the rationale that the one-way switch isolation of -55 dB provided sufficient matching to the open ports. Short-open-load measurements for a 1-port calibration were taken for each antenna. Next, we measured the through path between the transmitter and each receiver using a connector. In software, we combined the 1-port and through measurements to accomplish a 2-port

short-open-load-through (SOLT) calibration with arbitrary through between each transmitter and receiver for a total of 99 separate 2-port calibrations. The calibration for a particular transmitter/receiver pair is recalled in the VNA before taking data.

5. Numerical Model

We use Ansoft HFSS to numerically model the cavity, similar to [27]. We use it several ways. First, we model the feeding transmission lines in order to assign S -parameter reference planes that are identical in both simulation and experiment. Second, we estimate the normalized incident fields due to the transmitters throughout the cavity for use in (7) and (9), where the normalized incident fields now include all background multiple scattering not present between the object and the cavity. Also, we use the model to generate synthetic scattered field S -parameters of numerical targets in order to study the performance of the inverse scattering algorithm given the source geometry and system parameters.

Figure 4 shows the HFSS CAD model of the 12-sided cavity. The model includes the panel thickness and dielectric constant, bottom conductor, probe feed, coupling fluid properties, and height of the fluid. Same as in the experiment, the cavity is filled to a height that is 0.5 cm below the top (seen as the line below the top edge of the cavity). The remaining 0.5 cm is air with a radiating boundary condition. The outer boundary of the cavity is PEC.

Next we compare measured and simulated incident S -parameters in order to access the accuracy of the model. Figure 5 shows the magnitude and phase, respectively, of the measured and simulated incident S -parameters between each transmitter and all receivers. The magnitude and phase agree best when the receivers are on the same level as the transmitter. In this case, the magnitude agrees generally to within 3 dB, for all three levels, and the phase agrees to within 30 degrees, which is approximately $\lambda/10$, a common metric for many microwave systems. For measurements between antenna levels in Figure 5, the agreement is not as good in magnitude, but the phase error remains similar to the previous cases. This also shows that the one-way path loss across the cavity is approximately -50 dB, so we expect any multiple scattering to be localized. This partially justifies our approximation of the cavity dyadic Green's function with the lossy free-space dyadic Green's function.

When computing the incident fields, the center of the cavity was meshed with a coarse Cartesian grid of sparse unassigned sheets, shown in Figure 6. Sheets are spaced every 5 mm in the x , y , and z directions. The spacing is approximately $\lambda/5$ at 2.75 GHz in the fluid with relative permittivity of 21. We have found that this helps constrain the adaptive meshing of HFSS when we obtain the incident fields by interpolating the FEM mesh onto a fine Cartesian grid, [12].

When simulating the structure, with or without scattering targets, we use a convergence criterion of $\Delta S = 0.02$ which is reached in 7 adaptive meshing iterations. A typical simulation completed with approximately 1.4 million tetrahedra using 23.5 GBytes of RAM and swap

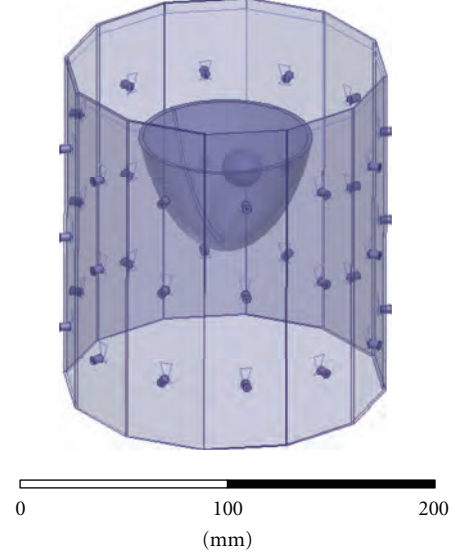


FIGURE 14: HFSS CAD numerical breast phantom of Example 2. The inclusion is 2 cm in diameter with relative permittivity and conductivity contrasts of 2 : 1. The skin layer is 2 mm thick.

space to obtain a full 36×36 S -matrix. Simulations took approximately 25 hours on a dual E5504 Intel Xeon (2x Quad Core) desktop with 24 GBytes of RAM. Figure 7 shows a typical convergence rate as a function of tetrahedra.

We obtained the incident fields for only the three transmitters. The incident fields for the receivers were obtained through rotation, where we assume the 12 panels of the experimental cavity are identical. The incident fields were sampled on a $17 \text{ cm} \times 17 \text{ cm} \times 18 \text{ cm}$ grid with 1 mm spacing, which is $\lambda/24$ at 2.75 GHz in a fluid with relative permittivity 21. In simulation, the average transmit power was 1 Watt, so, from transmission line analysis, the line voltage is given by

$$a_o = \sqrt{2P_{\text{ave}}Z_o} = \sqrt{2Z_o}, \quad (11)$$

which is used in (6). The phase of a_o is zero because the S -parameter reference planes of the HFSS model and the experimental cavity were identical.

Figure 8 shows three crosscuts of the z -component of the incident electric field through the center of the cavity for the center transmitter in a fluid of relative permittivity of 21 and conductivity 0.475 at 2.75 GHz. The coordinate origin is at the center of the cavity, and the transmitter is located on the positive x axis. The effects of the cavity on the incident field are seen in Figure 7, where the fields are guided by the walls of the cavity; the coaxial feeds are also visible; the fluid-air interface is visible in Figures 8(b) and 8(c).

6. Image Reconstructions

6.1. Synthetic Data. We first test the BIM and numerical characterization using synthetic data from HFSS. This is to assess the performance of the algorithm and source geometry under near ideal circumstances. We simulated the

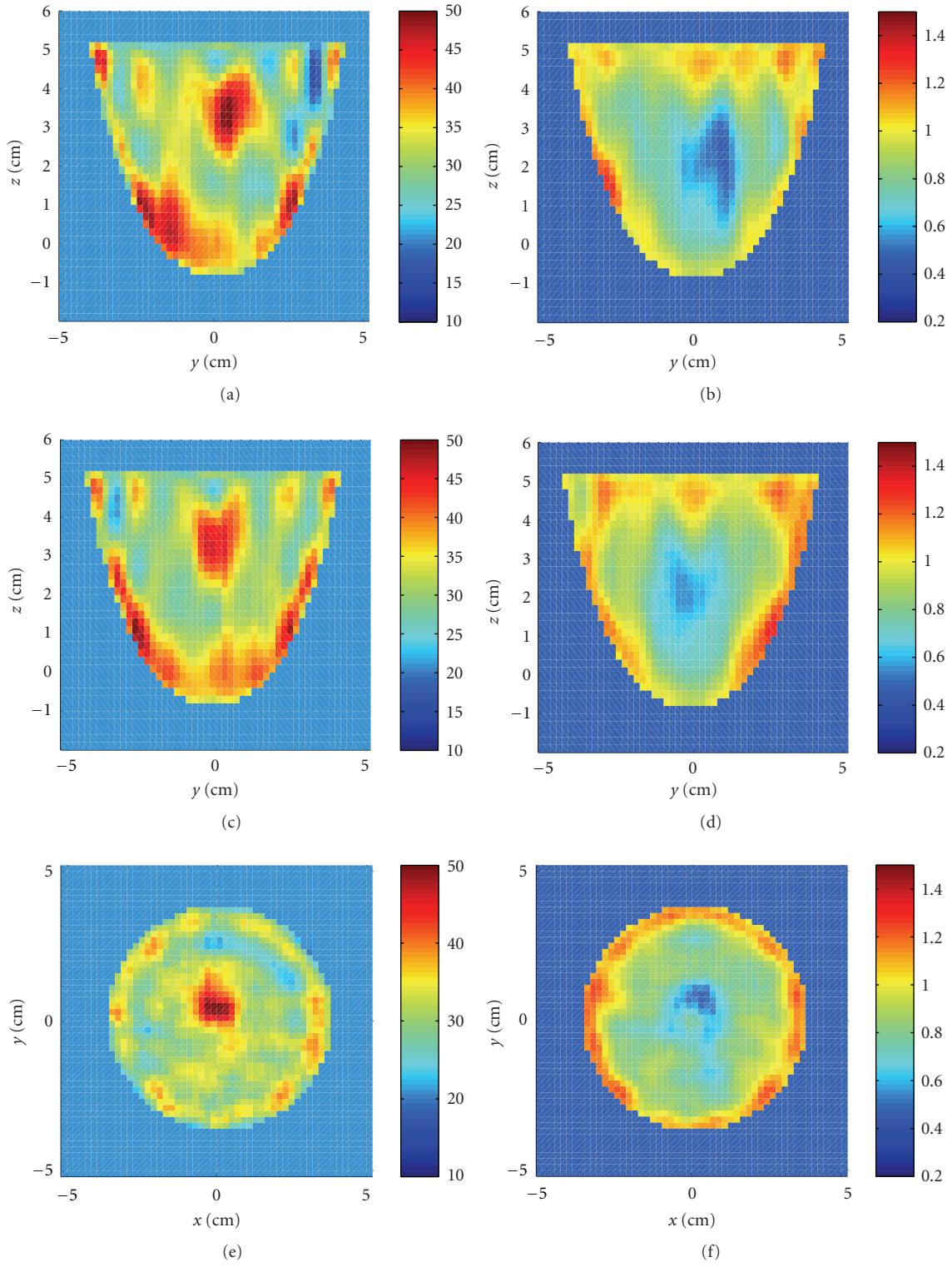


FIGURE 15: Reconstructions of the HFSS numerical breast phantom in Example 2 after four iterations. (a), (c), and (e) and (b), (d), and (f) Relative permittivity and conductivity, respectively. (a) and (b), (c) and (d), and (e) and (f) Cuts at $x = 0$ cm, $y = 0$ cm, and $z = 3$ cm. The relative permittivity of the inclusion is recovered, but both images contain many artifacts.

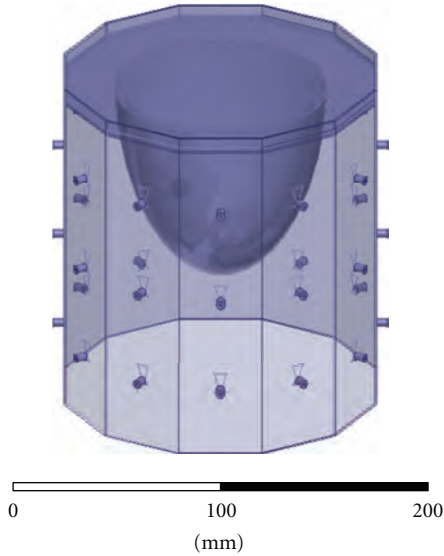


FIGURE 16: HFSS CAD numerical breast phantom with skin layer, fat layer, glandular tissue, and chest wall of Example 3. The inclusion is 1 cm in diameter with relative permittivity and conductivity contrasts of 2 : 1.

scattered field S -parameters of simple numerical objects and use these data as measurements in the inversion algorithm. HFSS scattered field data includes any multiple scattering between the object and the cavity. The background medium had a relative permittivity of 21 and a conductivity of 0.475 Siemens/m. The incident fields were computed with these background parameters and used in volume integral equations.

Example 1. We first used HFSS to simulate the scattered field S -parameters for a single 1.5 cm diameter sphere located at $(x, y, z) = (0, 0, 2 \text{ cm})$ with four combinations of relative permittivity and conductivity: (40, 1), (40, 0), (10, 1), and (10, 0). The HFSS model is shown in Figure 9. Figures 10, 11, 12, and 13 show images of the first and fourth BIM iterations for each object. As shown, in some cases, the BIM steps were essential in recovering the correct property values of the sphere; in other cases, the relative permittivity was improved at the expense of the conductivity value. These images show that the source geometry and numerical characterization are adequate for the retrieval of some object property combinations, but not others. This fact, together with the visible artifacts, suggests that the images could be improved with a denser source geometry.

Example 2. Next we imaged a more anatomical numerical breast phantom. The numerical phantom is shown in Figure 14. The breast is 9 cm at the widest point and 6 cm deep. The outer layer is a 2 mm thick skin layer, and the inclusion is 2 cm in diameter. The dielectric properties of the skin layer, glandular tissue, and inclusion, respectively, are $(\epsilon_r, \sigma) = \{(45, 1.59), (21, 0.475), \text{ and } (42, 0.8)\}$, which were obtained from [28]. We assume we know the volume region of the breast, so we mask that volume excluding all other

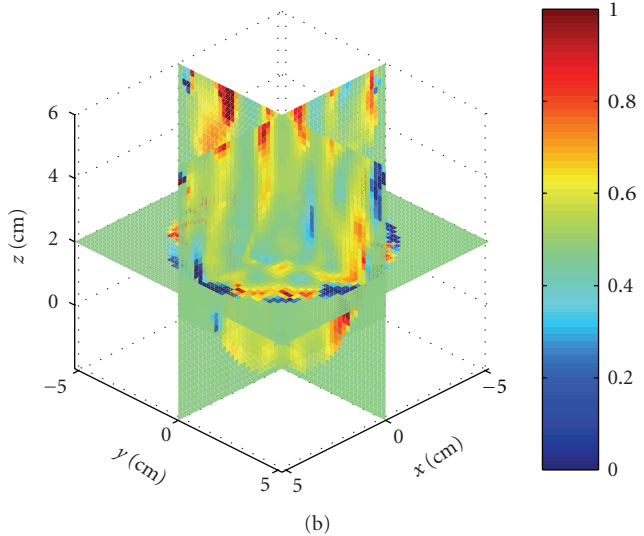
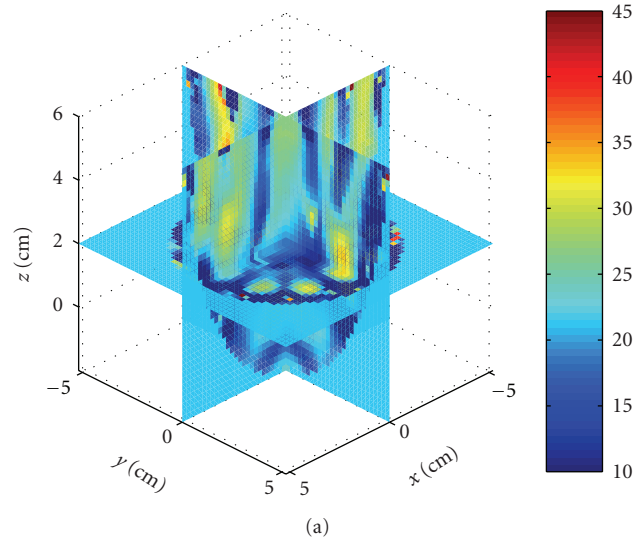


FIGURE 17: Reconstructions of the HFSS numerical breast phantom, which includes the chest wall of Example 3. (a) and (b) Relative permittivity and conductivity, respectively. The object could not be reconstructed.

points during inversion. Figure 15 shows the reconstructed relative permittivity and conductivity after 4 iterations for three cuts. The relative permittivity of the inclusion is recovered, but the conductivity of the inclusion is not recovered. The skin layer is also visible in the conductivity images. Both sets of images suffer from artifacts, which is due to the sparse spatial sampling of the antennas and indicates that the images can be improved with more angular views.

Example 3. To push the algorithm, we imaged a phantom that included a skin layer, fat layer, glandular tissue, chest wall, and inclusion, with relative permittivity and conductivity, respectively, of (45, 1.6), (5.1, 0.16), (21, 0.475), (52, 2.0), and (40, 1.0). The HFSS model is shown in Figure 16. The reconstructions are shown in Figure 17. In this case the algorithm failed to recover the contrasts. This suggests that

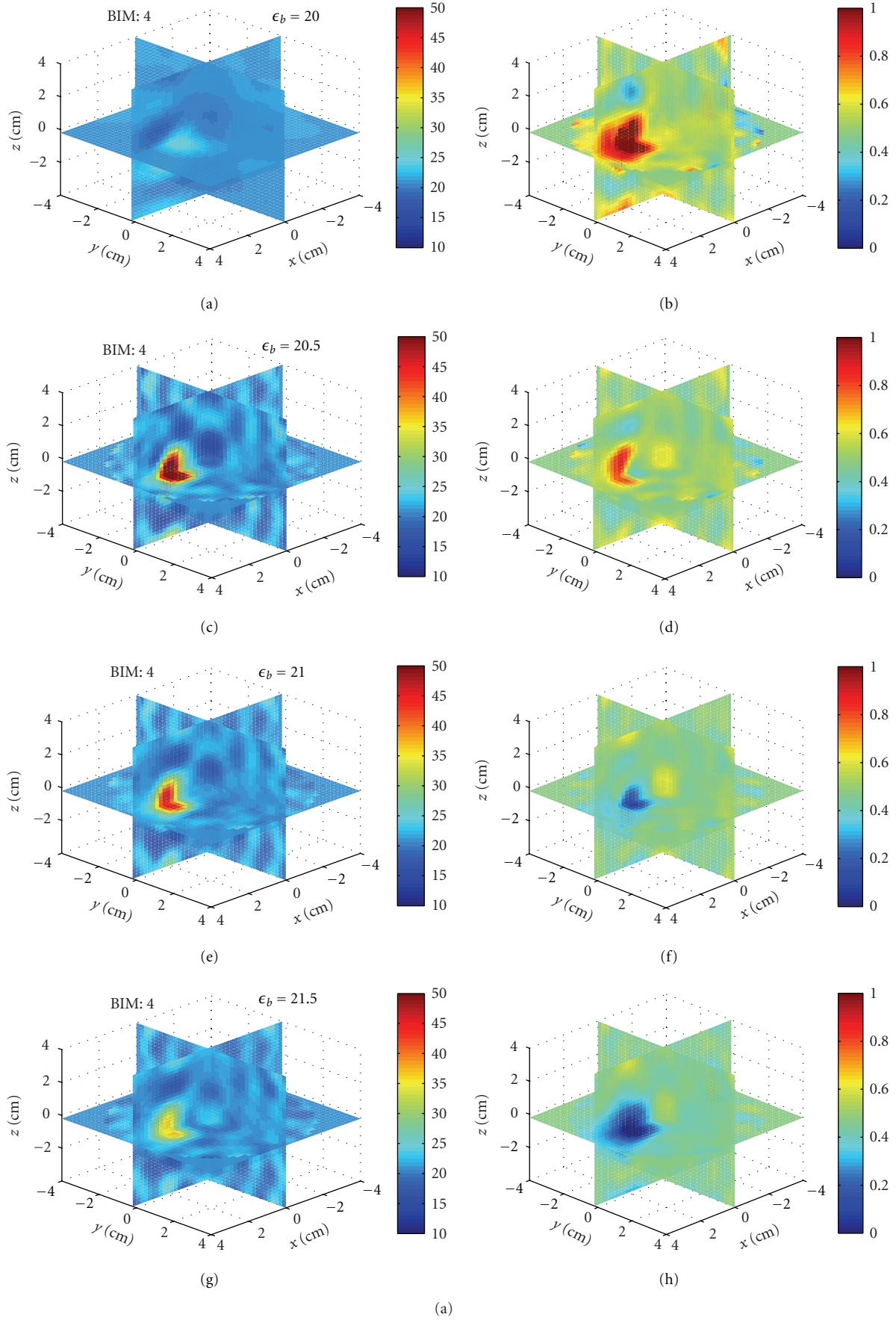


FIGURE 18: Continued.

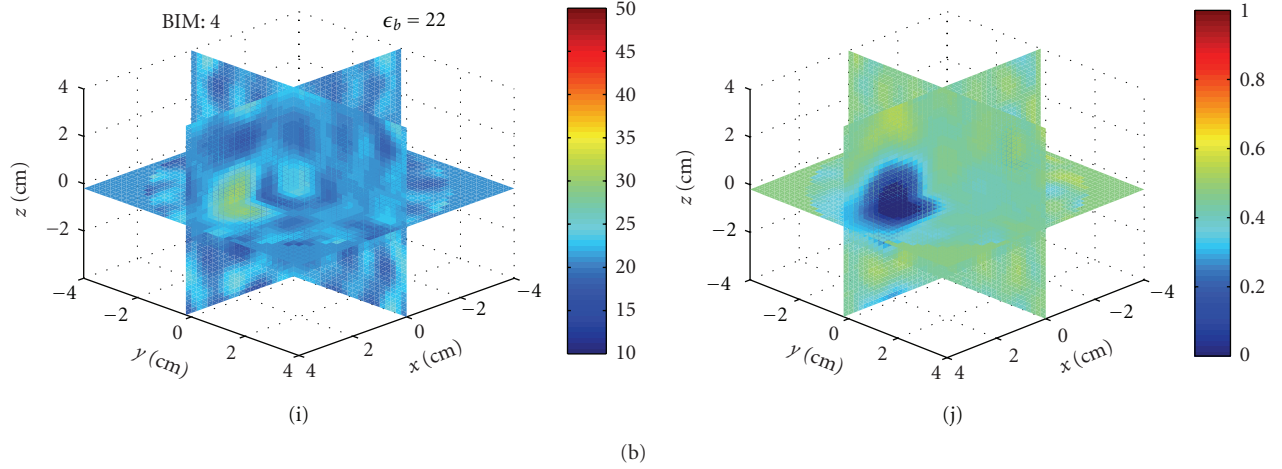


FIGURE 18: Sensitivity of image reconstructions to background permittivity for Example 4. (a), (c), (e), (g), and (i) and (b), (d), (f), (h), and (j) Relative permittivity and conductivity, respectively. The scattered field data was generated in HFSS in a background of (21, 0.475). The reconstructions are done with assumed background relative permittivities of 20, 20.5, 21, 21.5, 22 for (a) and (b), (c) and (d), (e) and (f), (g) and (h) and (i) and (j), respectively. The recovered contrasts of the sphere oscillate about the background.

(1) the object is too different from the background for the BIM to converge, (2) object-cavity interactions are too strong to use the free-space dyadic Green's function, or (3) images cannot be constructed if the chest wall is not modeled, meaning that it is necessary to model the chest wall for the incident fields and the dyadic Green's function.

Example 4. Finally, we studied the effects of different background permittivities when forming images. This represents a case in experiment where the measurements are taken in a fluid with some set of properties, but the fluid properties we use in the model are slightly off. We formed images using HFSS scattered field data of the sphere with $(\epsilon_r, \sigma) = (40, 0)$ in a background of $(\epsilon_b, \sigma) = (21, 0.475)$, but where we use incident fields from five different background permittivities: {20, 20.5, 21 (again), 21.5, 22} and the same conductivity.

Figure 18 shows 3D crosscuts at the fourth BIM iteration for all five backgrounds. Figures 18(e) and 18(f) are the correct images. Notice that an error in the background permittivity of 1, or 5%, is enough for the reconstructed object contrast to oscillate, demonstrating that reconstructions are very sensitive to our knowledge of the background properties.

6.2. Experimental Data. At this time, only simple plastic objects have been imaged with the experimental system; however, future work includes imaging more realistic breast phantoms. Among the test objects, we show the results here for several acrylic spheres. The objects were suspended from a platform and rotated to 12 positions in 30 degree increments. Scattered field S-parameter measurements from each position were combined to yield a full 36×36 S-parameter matrix, which was used in the inverse scattering algorithm.

Experiment 1. We imaged a single acrylic sphere, shown in Figure 19. The diameter of the sphere was 2.54 cm, with

properties $(\epsilon_r, \sigma) = (2.7, 0)$. The sphere was located at approximately $(x, y, z) = (1.5 \text{ cm}, 1.5 \text{ cm}, 0)$. Figure 20 shows the reconstructions after 4 iterations of the x - y plane. The inversion domain is masked so that only a cylindrical region containing the rotated object is imaged. We also imaged two acrylic spheres, shown in Figure 19. Figure 21 shows the reconstructions after 4 iterations. In both cases, the relative permittivity is recovered quite well, and the conductivity contrast is correctly valued but the shape is incorrect. There are also many artifacts present. Given that the imaging algorithm could recover the single sphere using HFSS data, we can attribute these discrepancies to differences between the experiment and the model, such as knowledge in the coupling medium properties, substrate properties, VNA calibration, cavity size measurements, or object motion.

Experiment 2. Finally, while the primary discussions in this paper concern a cavity having antennas that operate at 2.75 GHz, we also built a lower frequency cavity where the antennas operate at 915 MHz. This cavity was numerically characterized using the same methods, but the background fluid properties were $(\epsilon_r, \sigma) = (23, 0.1)$. Figure 22 shows the cavity with three acrylic spheres. Two spheres are located in the x - y plane, while the third is positioned at approximately $(x, y, z) = (4 \text{ cm}, -3 \text{ cm}, 5 \text{ cm})$. We imaged the relative permittivity and conductivity, and the results after 4 iterations are shown in Figure 23. The shape and properties of the two in-plane spheres are well recovered. The third sphere is also detected but cut off at the upper left of the imaging domain. Artifacts are also present, but this example better demonstrates that the numerical characterization, BIM, and free-space Green's function are capable of recovering objects in this cavity and source geometry. It should be noted that images formed with data at 915 MHz are less susceptible to modeling errors because the cavity and objects are electrically smaller, but the resolution is reduced.

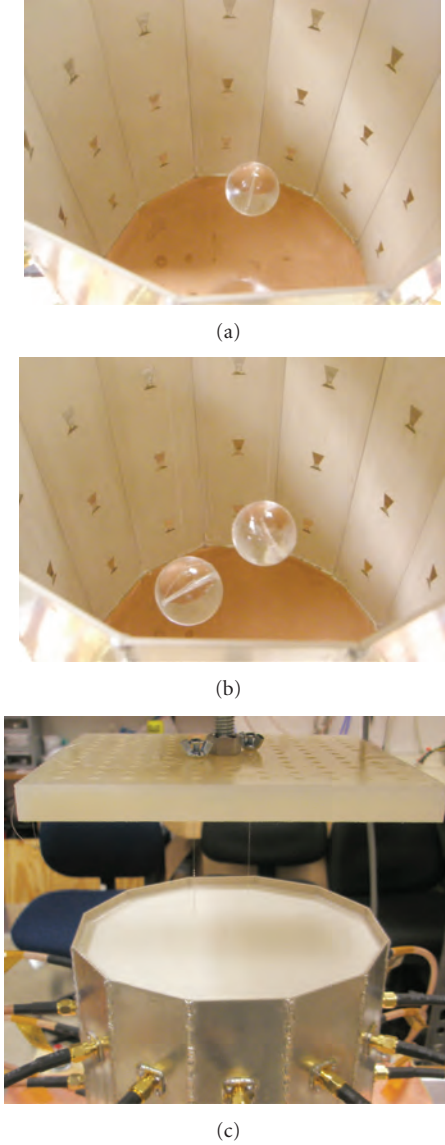


FIGURE 19: Test objects and coupling fluid for Experiment 1. (a) Single suspended acrylic sphere. (b) Two acrylic spheres. (c) Cavity filled with the coupling medium. Objects are suspended and rotated from the nylon platform.

6.3. Discussion. Overall, the imaging algorithm, numerical characterization, and experiment worked with some success, and there are several areas for continued investigation.

First, Examples 1 and 2, and also Experiments 1 and 2, validate the technique described in this paper showing that the numerical characterization of the cavity incident fields and the use of the vector Green's function formulation linking the incident fields to the inverse scattering algorithm can be used to successfully form images in a cavity geometry. Examples 1 and 2 demonstrate the consistency of the method using synthetic scattered field S-parameter data. Experiments 1 and 2 show that the characterization and experiment agreed enough for the BIM to recover the location and permittivity of the test objects. More realistic phantoms

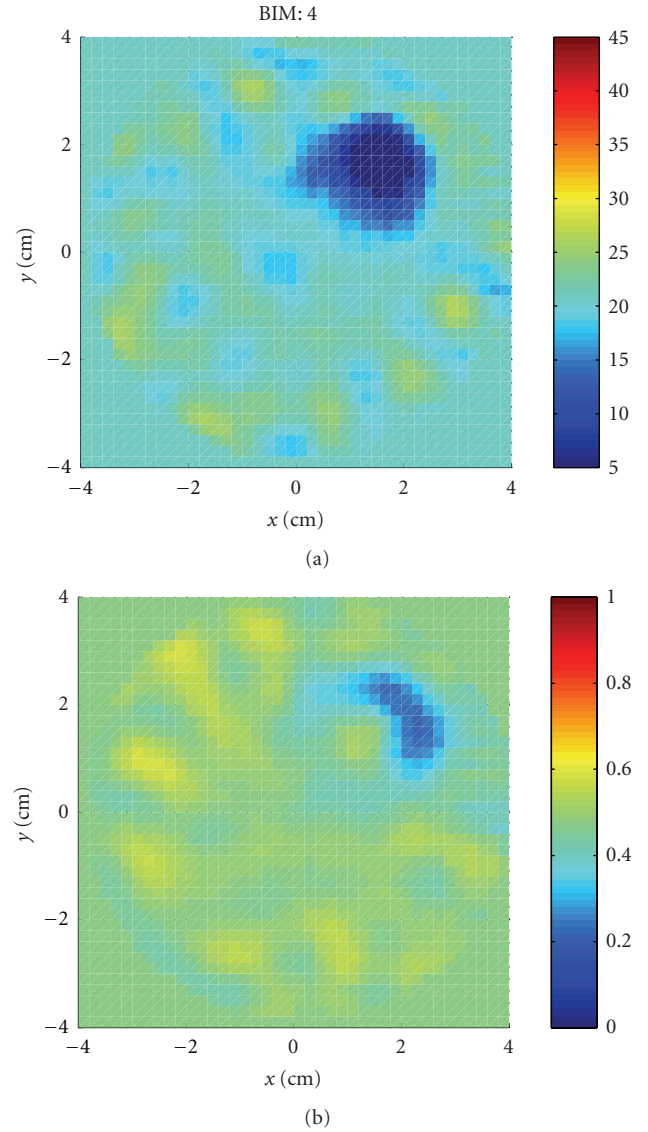


FIGURE 20: Reconstructions of the single acrylic sphere of Experiment 1 shown in Figure 19(a). (a): Relative permittivity. (b): Conductivity. The permittivity is recovered well but the shape in the conductivity is not.

and lower contrast phantoms will help further confirm the methodology.

Second, in Example 1, although some permittivity and conductivity combinations of the sphere were recovered, others were not. Given that the data was synthetic, this points to inherent imaging ambiguities in the simultaneous retrieval of both permittivity and conductivity in the inverse scattering problem. Possible solutions are increasing the number of unique data, or including prior information about the relations between permittivity and conductivity in tissue.

Third, the success of the algorithm in Example 2 in recovering the partial breast phantom suggests that our use of the lossy free-space dyadic Green's function in the forward solver of the BIM did not grossly affect image reconstruction

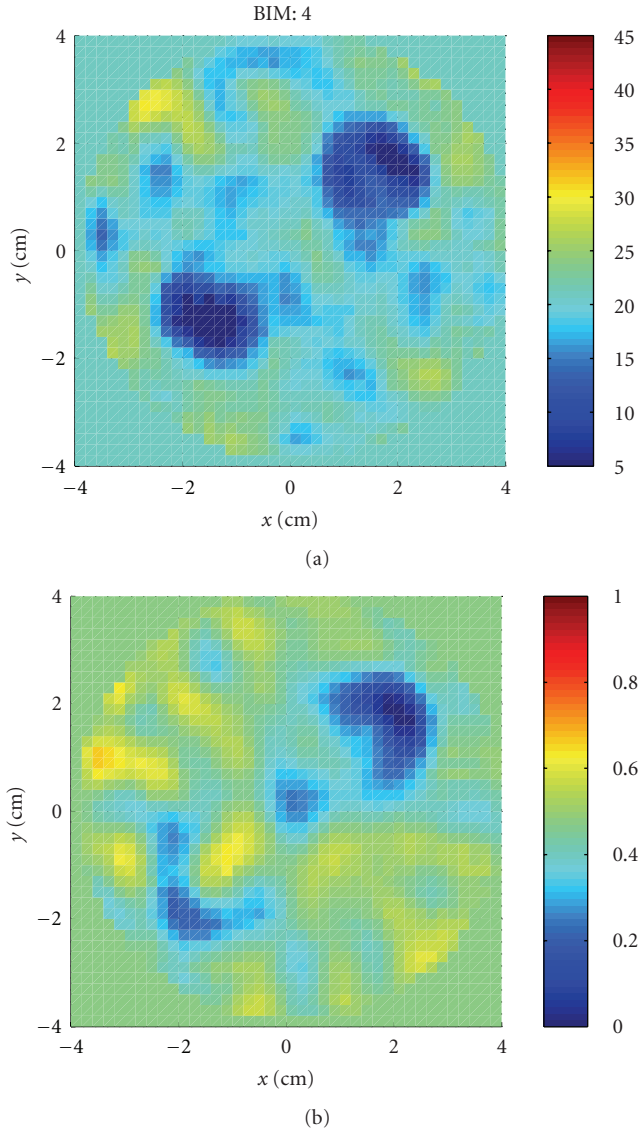


FIGURE 21: Reconstructions of the two acrylic spheres of Experiment 1 shown in Figure 19(b). (a) Relative permittivity. (b) Conductivity. The permittivity is again recovered well but the shape in the conductivity is not.

in this case. This is keeping in mind that the synthetic scattered field S -parameter data did include any multiple scattering between the phantom and the cavity.

Fourth, in light of the successful reconstruction of the simple phantom in Example 2, the failure of the algorithm to recover the more complete breast phantom in Example 3 points to the need to model the chest wall. This can be done by including it in the incident field computations but it may also be necessary in estimating the cavity dyadic Green's function. This is an area to be investigated.

Lastly, Example 4 shows that we must know the background relative permittivity to within 5% of the actual or else risk incorrectly estimating whether the contrasts are higher or lower than the background. An equivalent error can arise from a correct background permittivity but incorrectly



FIGURE 22: Second cavity with antennas designed to operate at 915 MHz of Experiment 2. Three acrylic sphere are suspended (one visible). Cavity is filled with fluid for imaging.

measuring the dimensions of the cavity. We suspect that the very high recovered conductivity values in both Experiments 1 and 2 may be due in part to these types of systematic errors. This demonstrates the difficulty in achieving the necessary consistency between the model, experiment, characterization, and imaging algorithm to accurately form microwave breast images of diagnostic quality.

7. Conclusion

We demonstrated the use of a numerical characterization technique for a breast imaging system prototype. We used HFSS to numerically estimate the incident fields of the antennas in a cavity geometry and formally linked them to an S -parameter-based inverse scattering algorithm and experimental setup. The imaging algorithm was the Born Iterative Method and recovered both numerical and experimental test objects with some success. Future work includes further validation of our methodology, imaging realistic breast phantoms, investigating practical solutions to modeling breast-cavity scattering interactions, image quality assessments with and without numerical characterization, and developing a hemispherical cavity and clinical imaging system.

Appendix

Determining the Background Dyadic Green's Function

We list the following approaches for obtaining the background dyadic Green's function as work for future investigation.

Analytical Dyadic Green's Function. There exist analytical solutions of the dyadic Green's function for some simple cavity geometries, such as cubes or cylinders, [29], which might approximately model certain cavity-based imaging setups. These solutions, however, will likely not include finer details such as antenna plating, connectors, substrate material, or open-ended cavities, such as those used for breast imaging. Analytic solutions though lend themselves to the possibility of retaining some convolution structure in the VIE so fast forward solvers can be used (e.g., fast half space solutions

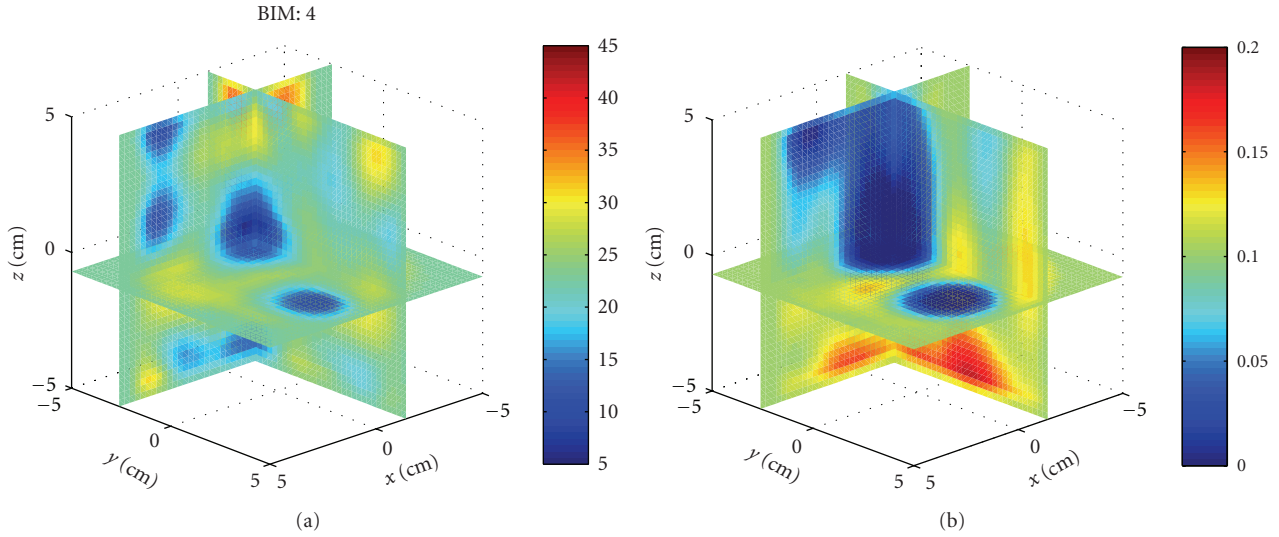


FIGURE 23: Reconstruction of the relative permittivity and conductivity of three acrylic spheres using a cavity operating at 915 MHz from Experiment 2. The two spheres in plane are well recovered and the third detected at the upper left of the image.

[30], applied to multisided cavities). Determining the dyadic Green's function analytically becomes a formidable task as the geometry complicates, where simulation may be better suited.

Full Numeric Simulation. The most complete solution is to fully simulate the object and cavity using a numeric simulator, which will capture all the multiple scattering between the object and the cavity. However, unlike a dyadic Green's function, which only needs to be found once for a particular geometry and the values of which are only needed on the interior of the object domain, this method must simulate the cavity structure outside the object domain in every instance of the simulation. When used in an inverse scattering algorithm, which might compute the domain VIE for each source, frequency, and iteration, then repeatedly simulating the cavity structure adds to the already high computational burden. In addition, one must choose a proper simulation technique to handle both antenna surfaces and inhomogeneous media.

Numerical Dyadic Green's Function. If analytical solutions are not accurate enough, then one must determine the dyadic Green's function numerically. This requires simulating three orthogonal dipoles in turn at every point in the object domain and recording the response at every other point in the domain. The dyadic Green's function is symmetric, so half of the combinations are redundant, and while the convolution nature of the VIE is destroyed, some computational speed-up is possible for symmetric operators. This technique, however, requires accurate modeling around the dipole singularity, which can be difficult. In the case of PEC structures, the technique in [31] computes the dyadic Green's function by finding an array of image dipoles outside the cavity, which avoids the complications from the singularity. The main advantage of determining the dyadic Green's function numerically is that, once found, we no longer need to simulate the cavity structure and can turn our attention to optimizing the computation of the dyadic Green's function.

Approximate Solutions. If the background loss is sufficiently high, so that the resonances of the cavity are damped, then we can approximate the dyadic Green's function. This can be done by adopting an analytical solution (e.g., free-space or cavity) or by, for instance, developing a perturbation method. Adopting the free-space dyadic Green's function (or a perturbation on it) also allows us to retain the convolution structure of the VIE- and FFT-based forward solvers, which may be more beneficial to the inverse scattering algorithm than modeling higher-order multiple scattering.

Acknowledgments

The authors would like to thank Steven Clarkson for help with data collection. They would also like to thank the Basic Radiological Sciences Ultrasound Group for the use of the positioning equipment and useful discussions. This research was supported in part by the Department of Defense, Breast Cancer Research Program, Predoctoral Traineeship Award no. BC073270, DoD/BCRP award no. BC095397, the National Institute of Health T32 EB005172, and by the National Science Foundation award no. 0756338.

References

- [1] P. M. Meaney, M. W. Fanning, D. Li, S. P. Poplack, and K. D. Paulsen, "A clinical prototype for active microwave imaging of the breast," *IEEE Transactions on Microwave Theory and Techniques*, vol. 48, no. 1, pp. 1841–1853, 2000.
- [2] T. Rubk, P. M. Meaney, P. Meincke, and K. D. Paulsen, "Non-linear microwave imaging for breast-cancer screening using Gauss-Newton's method and the CGLS inversion algorithm," *IEEE Transactions on Antennas and Propagation*, vol. 55, no. 8, pp. 2320–2331, 2007.
- [3] C. Gilmore, P. Mojabi, A. Zakaria et al., "A wideband microwave tomography system with a novel frequency selection procedure," *IEEE Transactions on Biomedical Engineering*, vol. 57, no. 4, pp. 894–904, 2010.

- [4] T. Rubk, O. S. Kim, and P. Meincke, "Computational validation of a 3-D microwave imaging system for breast-cancer screening," *IEEE Transactions on Antennas and Propagation*, vol. 57, no. 7, pp. 2105–2115, 2009.
- [5] M. Klemm, I. J. Craddock, J. A. Leendertz, A. Preece, and R. Benjamin, "Radar-based breast cancer detection using a hemispherical antenna array—experimental results," *IEEE Transactions on Antennas and Propagation*, vol. 57, no. 6, pp. 1692–1704, 2009.
- [6] J. P. Stang, W. T. Joines, Q. H. Liu et al., "A tapered microstrip patch antenna array for use in breast cancer screening," in *Proceedings of the IEEE International Symposium on Antennas and Propagation and USNC/URSI National Radio Science Meeting (APSURSI '09)*, North Charleston, SC, USA, June 2009.
- [7] C. Yu, M. Yuan, J. Stang et al., "Active microwave imaging II: 3-D system prototype and image reconstruction from experimental data," *IEEE Transactions on Microwave Theory and Techniques*, vol. 56, no. 4, pp. 991–1000, 2008.
- [8] M. Ostadrahimi, P. Mojabi, C. Gilmore et al., "Analysis of incident field modeling and incident/scattered field calibration techniques in microwave tomography," *IEEE Antennas and Wireless Propagation Letters*, vol. 10, pp. 900–903, 2011.
- [9] S. M. Aguilar, M. A. Al-Joumayly, S. C. Hagness, and N. Behdad, "Design of a miniaturized dual-band patch antenna as an array element for microwave breast imaging," in *Proceedings of the IEEE International Symposium on Antennas and Propagation and USNC/URSI National Radio Science Meeting (APSURSI '10)*, Toronto, Canada, July 2010.
- [10] M. Klemm, C. Fumeaux, D. Baumann, and I. J. Craddock, "Time-domain simulations of a 31-antenna array for breast cancer imaging," in *Proceedings of the IEEE International Symposium on Antennas and Propagation and USNC/URSI National Radio Science Meeting (APSURSI '11)*, pp. 710–713, Spokane, Wash, USA, July 2011.
- [11] E. A. Attardo, A. Borsic, P. M. Meaney, and G. Vecchi, "Finite element modeling for microwave tomography," in *Proceedings of the IEEE International Symposium on Antennas and Propagation and USNC/URSI National Radio Science Meeting (APSURSI '11)*, pp. 703–706, Spokane, Wash, USA, July 2011.
- [12] M. Haynes and M. Moghaddam, "Vector green's function for S-parameter measurements of the electromagnetic volume integral equation," in *Proceedings of the IEEE International Symposium on Antennas and Propagation and USNC/URSI National Radio Science Meeting (APSURSI '11)*, pp. 1100–1103, Spokane, Wash, USA, July 2011.
- [13] M. Haynes, S. Clarkson, and M. Moghaddam, "Electromagnetic inverse scattering algorithm and experiment using absolute source characterization," in *Proceedings of the IEEE International Symposium on Antennas and Propagation and USNC/URSI National Radio Science Meeting (APSURSI '11)*, pp. 2545–2548, Spokane, Wash, USA, July 2011.
- [14] M. Haynes and M. Moghaddam, "Large-domain, low-contrast acoustic inverse scattering for ultrasound breast imaging," *IEEE Transactions on Biomedical Engineering*, vol. 57, no. 11, Article ID 5510108, pp. 2712–2722, 2010.
- [15] A. Tarantola, *Inverse Problem Theory*, SIAM, Philadelphia, Pa, USA, 2005.
- [16] W. C. Chew, *Waves and Fields in Inhomogeneous Media*, IEEE, New York, NY, USA, 1995.
- [17] W. C. Chew and Y. M. Wang, "Reconstruction of two-dimensional permittivity distribution using the distorted Born iterative method," *IEEE Transactions on Medical Imaging*, vol. 9, no. 2, pp. 218–225, 1990.
- [18] M. Moghaddam and W. C. Chew, "Nonlinear two-dimensional velocity profile inversion using time domain data," *IEEE Transactions on Geoscience and Remote Sensing*, vol. 30, no. 1, pp. 147–156, 1992.
- [19] L. Fenghua, Q. H. Liu, and L.-P. Song, "Three-dimensional reconstruction of objects buried in layered media using Born and distorted Born iterative methods," *IEEE Geoscience and Remote Sensing Letters*, vol. 1, no. 2, pp. 107–111, 2004.
- [20] H. Gan and W. C. Chew, "Discrete BCG-FFT algorithm for solving 3D inhomogeneous scatterer problems," *Journal of Electromagnetic Waves and Applications*, vol. 9, no. 10, pp. 1339–1357, 1995.
- [21] Z. Q. Zhang and Q. H. Liu, "Three-dimensional weak-form conjugate- and biconjugate-gradient FFT methods for volume integral equations," *Microwave and Optical Technology Letters*, vol. 29, no. 5, pp. 350–356, 2001.
- [22] P. Zwamborn and P. M. van den Berg, "The three dimensional weak form of the conjugate gradient FFT method for solving scattering problems," *IEEE Transactions on Microwave Theory and Techniques*, vol. 40, no. 9, pp. 1757–1766, 1992.
- [23] M. Lazebnik, L. McCartney, D. Popovic et al., "A large-scale study of the ultrawideband microwave dielectric properties of normal breast tissue obtained from reduction surgeries," *Physics in Medicine and Biology*, vol. 52, no. 10, pp. 2637–2656, 2007.
- [24] P. M. Meaney, S. A. Pendergrass, M. W. Fanning, D. Li, and K. D. Paulsen, "Importance of using a reduced contrast coupling medium in 2D microwave breast imaging," *Journal of Electromagnetic Waves and Applications*, vol. 17, no. 2, pp. 333–355, 2003.
- [25] J. Stang, L. van Nieuwstadt, C. Ward et al., "Customizable liquid matching media for clinical microwave breast imaging," *Physics in Medicine and Biology*. In preparation.
- [26] J. P. Stang and W. T. Joines, "Tapered microstrip patch antenna array for microwave breast imaging," in *IEEE/MTT-S International Microwave Symposium Digest*, July 2008.
- [27] J. Stang, *A 3D active microwave imaging system for breast cancer screening*, Ph.D. dissertation, Department of Electrical and Computer Engineering Duke University, Durham, NC, USA, 2008.
- [28] M. Lazebnik, E. L. Madsen, G. R. Frank, and S. C. Hagness, "Tissue-mimicking phantom materials for narrowband and ultrawideband microwave applications," *Physics in Medicine and Biology*, vol. 50, no. 18, pp. 4245–4258, 2005.
- [29] C.-T. Tai, *Dyadic Green's Functions in Electromagnetic Theory*, IEEE, New York, NY, USA, 1994.
- [30] X. Millard and Q. H. Liu, "A fast volume integral equation solver for electromagnetic scattering from large inhomogeneous objects in planarly layered media," *IEEE Transactions on Antennas and Propagation*, vol. 51, no. 9, pp. 2393–2401, 2003.
- [31] F. D. Q. Pereira, P. V. Castejón, D. C. Rebenague, J. P. García, and A. A. Melcón, "Numerical evaluation of the green's functions for cylindrical enclosures by a new spatial images method," in *IEEE Transactions on Microwave Theory and Techniques*, vol. 53, pp. 94–104, January 2005.

Self-Characterization of Commercial Ultrasound Probes in Transmission Acoustic Inverse Scattering: Transducer Model and Volume Integral Formulation

Mark Haynes, *Member, IEEE*, Sacha A. M. Verweij, Mahta Moghaddam, *Fellow, IEEE*,
and Paul L. Carson, *Senior Member, IEEE*

Abstract—A self-contained source characterization method for commercial ultrasound probes in transmission acoustic inverse scattering is derived and experimentally tested. The method is based on modified scattered field volume integral equations that are linked to the source-scattering transducer model. The source-scattering parameters are estimated via pair-wise transducer measurements and the nonlinear inversion of an acoustic propagation model that is derived. This combination creates a formal link between the transducer characterization and the inverse scattering algorithm. The method is tested with two commercial ultrasound probes in a transmission geometry including provisions for estimating the probe locations and aligning a robotic rotator. The transducer characterization results show that the nonlinear inversion fit the measured data well. The transducer calibration and inverse scattering algorithm are tested on simple targets. Initial images show that the recovered contrasts are physically consistent with expected values.

I. INTRODUCTION

INVERSE scattering has received attention as a means of improving medical ultrasound by providing quantitative images of tissue material properties, such as speed of sound, without the traditional artifacts of backscatter ultrasound [1], [2]. Inverse scattering systems, however, require full-wave scattering simulations, large-scale optimization algorithms, and absolute source characterization. Despite ongoing progress in system and algorithm development [3]–[10], transducer characterization remains an open topic in making ultrasound inverse scattering experimentally viable. The effects of incomplete transducer characterization on image quality in full-wave breast ultrasound, for example, have been reported in [11].

Manuscript received October 16, 2013; accepted December 4, 2013. This research was supported in part by the Department of Defense, Breast Cancer Research Program, Predoctoral Traineeship Award number BC073270, DoD/BCRP award number BC095397; the National Institutes of Health T32 EB005172; and by the National Science Foundation award number 0756338.

M. Haynes and M. Moghaddam are with the Electrical Engineering–Electrophysics Department, University of Southern California, Los Angeles, CA (e-mail: mshaynes@usc.edu).

S. A. M. Verweij is with the Applied Physics Department, Stanford University, Stanford, CA.

P. L. Carson is with the Basic Radiological Sciences Ultrasound Group, The University of Michigan, Ann Arbor, MI.

DOI <http://dx.doi.org/TBC>

Not all transducer characterization methods are suitable for full-wave imaging. Phased-array beamforming, for instance, requires only magnitude radiation patterns measured with hydrophones. Plane wave approximations are also sufficient for many geometries. Also, recent demonstrations of hybrid speed of sound and diffraction tomography algorithms have successfully produced quantitative ultrasound images without transducer characterization [10], [12]. Full-wave inverse scattering, however, requires transducer field characterization with absolute phase; the transducer model must relate the actual radiated fields to the input/output voltages using more than an ideal transfer function. Even if a full-wave characterization exists, it is not always clear how to incorporate the information into the imaging algorithms. Thus, we seek a transducer characterization method that can capture the full-wave behavior of a transducer and can also be rigorously linked to the equations of the inverse scattering algorithm.

In previous work, we developed a formalism for microwave inverse scattering and antenna characterization in which we linked the source model, inversion algorithm, object properties, and measurements in a consistent framework [13], [14]. We proved the method in several experiments [15], [16] in which we formed quantitative images of dielectric constant without the use of calibration targets. Given the success of this method in microwave imaging, we sought to develop and test the analogous method for ultrasound inverse scattering.

Although the derivation of the acoustic formalism is straightforward, key differences between microwave and ultrasound experimentation have motivated several additional developments. First, much of the success in our microwave experiments was due to our ability to fully simulate antenna sources using commercial electromagnetic software packages. This allowed antenna characterization to be independent of the measurement setup. We are unable to do this with ultrasonic transducers given their small size and unknown construction. Without full electromechanical simulation, we must characterize the transducers from measurement alone. Second, performing hydrophone measurements that satisfy the requirements for full-wave characterization is not trivial and is complicated by the effects of the hydrophone. Assuming that simulation and hydrophone measurements are unavailable, we

DRAFT

would still like to characterize the transducers within the framework we are going to develop.

These considerations and our current interest in transmission imaging have prompted us to explore a new self-characterization technique for multi-element commercial probes in a transmission geometry. The characterization technique is based on an acoustic propagation model that relates pair-wise voltage measurements between multiple transducer elements. We use this propagation model to derive a fast, semi-analytic nonlinear optimization procedure to estimate the transducer model parameters from self-measurements. This eliminates the need for external field probes that are different from the sources themselves, and is the first such attempt within this formalism in acoustics or electromagnetics.

In Section II, we derive the acoustic formalism, which is analogous to our work in [13]–[15]. First, we explain the transducer source model, which is based on the acoustic source-scattering matrix and derive the propagation model. We further augment the transducer model for the expected electrical driving frequencies. The transducer model is then used to modify the acoustic volume integral equations of the inverse scattering algorithm. In Section III, we discuss source characterization to motivate and then derive the optimization routine for the self-calibration technique. Section IV describes our experimental setup and characterization results, including the assumptions necessary to carry out the analysis. Finally, in Section V, the inverse scattering algorithm is tested and preliminary images of simple targets are presented and discussed.

Several provisions were required to test this method in experiment, which we explain throughout Sections IV and V. We use two linear-array commercial hand probes. This limits the setup to a planar transmission geometry. We use a Verasonics data acquisition system[AU1: Please provide manufacturer name and location.], which requires several assumptions about the nature of the transmit pulse. This leads to the use of virtual sources. Finally, the implemented geometry is static, so test objects being imaged must be rotated to obtain multiple transmitter views. We use a robotic arm to rotate the objects, while aligning with reflection measurements.

II. FORMULATION

Inverse scattering algorithms are typically built with two volume integral equations (VIEs). To use the VIEs in experimental inverse scattering, we must model the fields radiated and received by the transducers, and incorporate this model into the VIEs. What follows is the acoustic analog of our previous work [13]–[15], in which we combined an antenna model and electromagnetic inverse scattering algorithm.

We first give the traditional acoustic volume integral equations. We then summarize the source-scattering matrix formulation and adapt it to ultrasound frequencies.

Then the acoustic propagation model is derived, which is the basis for the self-characterization method. Finally, we modify the volume integral equations so that they are consistent with the transducer model.

A. Traditional Volume Integral Equations

The acoustic VIE for the total pressure field in the presence of an inhomogeneous distribution of compressibility, density, and compressive loss, is given by

$$\phi(\mathbf{r}) = \phi_{\text{inc}}(\mathbf{r}) + k_o^2 \int g(\mathbf{r}, \mathbf{r}') \left(\delta\kappa(\mathbf{r}') + i \frac{\delta\alpha(\mathbf{r}')}{\kappa_o \omega} \right) \phi(\mathbf{r}') dV' + \int g(\mathbf{r}, \mathbf{r}') \nabla' \cdot \delta\rho^{-1}(\mathbf{r}') \nabla' \phi(\mathbf{r}') dV' \quad (1)$$

$$k^2 = k_o^2 \left(1 + i \frac{\alpha_o}{\kappa_o \omega} \right), \quad (2)$$

where $k_o^2 = \omega^2 \rho_o \kappa_o$ is the lossless background wave number and $g(\mathbf{r}, \mathbf{r}')$ is the free-space Green's function with wave number k . The incident field, $\phi_{\text{inc}}(\mathbf{r})$, is the field in the absence of the object. We define the following contrast functions for the density, compressibility, and compressive loss, respectively, as

$$\delta\rho^{-1}(\mathbf{r}) = \frac{\rho_o}{\rho(\mathbf{r})} - 1 \quad (3)$$

$$\delta\kappa(\mathbf{r}) = \frac{\kappa(\mathbf{r})}{\kappa_o} - 1 \quad (4)$$

$$\delta\alpha(\mathbf{r}) = \alpha(\mathbf{r}) - \alpha_o, \quad (5)$$

where ρ_o , κ_o , and α_o are the background material constants. The quantities $\delta\rho^{-1}$ and $\delta\kappa$ are unitless, and $\delta\alpha$ is an absolute measure of compressive loss with units of $\text{Pa}^{-1}\text{s}^{-1}$.

Defining the scattered field as

$$\phi_{\text{sca}}(\mathbf{r}) = \phi(\mathbf{r}) - \phi_{\text{inc}}(\mathbf{r}), \quad (6)$$

we can write the VIE for the scattered field concisely as

$$\phi_{\text{sca}}(\mathbf{r}) = \int g(\mathbf{r}, \mathbf{r}') O(\mathbf{r}') \phi(\mathbf{r}') dV', \quad (7)$$

where we define the object function $O(\mathbf{r})$ as the linear operator

$$O(\mathbf{r}) = k_o^2 \left(\delta\kappa(\mathbf{r}) + i \frac{\delta\alpha(\mathbf{r})}{\kappa_o \omega} \right) + k_o^2 \nabla' \cdot \delta\rho^{-1}(\mathbf{r}) \nabla'. \quad (8)$$

In the context of inverse scattering, (1) represents the solution to the forward scattering problem and (7) is used to relate the material contrasts to scattered field measurements outside the object domain. Traditionally, these equations are used as is to develop inverse scattering algorithms.

B. Source Model

1) *Field Expansion*: The pressure field about an acoustic source can be expanded in terms of incoming and outgoing wave functions as

$$\phi(\mathbf{r}) = \sum_{l=0}^{\infty} \sum_{m=-l}^l (a_{lm} \Re \psi_{lm}(\mathbf{r}) + b_{lm} \psi_{lm}(\mathbf{r})), \quad (9)$$

where a_{lm} and b_{lm} are the multipole coefficients for incoming and outgoing harmonics, respectively, \mathbf{r} is the position vector, and \Re means the regular part of the corresponding Bessel function. The double sum is hereafter abbreviated \sum_{lm} with the same limits. The free-space scalar wave functions are given by [17]

$$\psi_{lm}(\mathbf{r}) = z_l(kr) Y_{lm}(\theta, \phi), \quad (10)$$

where $z_l(x)$ is any one of $j_l(x)$, $y_l(x)$, $h_l^{(1)}(x)$, $h_l^{(2)}(x)$, and $Y_{lm}(\theta, \phi)$ are the spherical angular harmonics.

2) *Source Scattering Matrix Formulation*: Following the source scattering-matrix formulation [18], [19], a transducer is connected through a shielded transmission line to a voltage source or receiver, Fig. 1. We define a_o and b_o as complex outgoing and incoming modes, respectively, on the transmission line measured at a reference plane. We relate these modes to the multipole coefficients of the pressure field through a linear model

$$b_o = \Gamma a_o + \sum_{lm} u_{lm} a_{lm} \quad (11)$$

$$b_{lm} = t_{lm} a_o + \sum_{l'm'} S_{lm,l'm'} a_{l'm'}, \quad (12)$$

where t_{lm} and u_{lm} are transmit and receive coefficients, respectively. The matrix $S_{lm,l'm'}$ captures the passive scattering properties of the acoustic source and Γ is the reflection coefficient seen looking into the device.

From electro-acoustic reciprocity, the following relations can be derived between the transmit and receive coefficients [18],

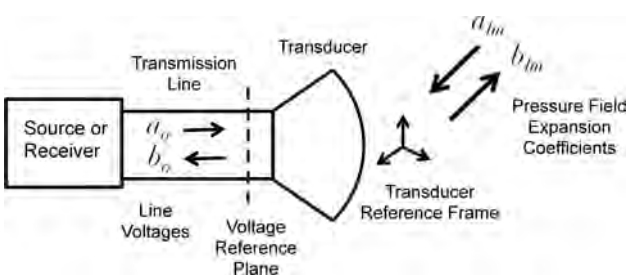


Fig. 1. Acoustic source and transmission line setup. a_o and b_o are outgoing and incoming modes on the transmission line, respectively.

$$u_{lm} = \frac{Z_o}{2\rho_o c k^2} (-1)^m t_{l,-m} \quad (13)$$

$$S_{l,m,l'm'} = (-1)^{m+m'} S_{l-m,l'-m'}, \quad (14)$$

where ρ_o , c , and k are the background density, sound speed, and wave number, respectively, and Z_o is the characteristic impedance of the line.

3) *Relation to Total Line Voltage*: The use of left and right traveling line voltages is advantageous for microwave problems, because it allows the source-scattering formulation to be naturally adapted to microwave S-parameters [13]. Given the long electrical wavelengths at ultrasound operating frequencies (1 to 10 MHz), full network analysis is not usually required. We measure only the total line voltage, so there is no need to define a phase reference plane on the transmission line. However, the electrical impedance (and thus the reflection coefficient) of the acoustic source does affect the system response. Here, we modify the source scattering formulation for use with the total line voltage.

The total line voltage is given as $V_o = a_o + b_o$. If the acoustic device is purely receiving, we expect no input mode, $a_o = 0$, so $b_o = V_o$, which we define as the total output voltage on the line, V_{out} :

$$V_{\text{out}} = b_o = \sum_{lm} u_{lm} a_{lm}. \quad (15)$$

If the device is purely transmitting and no other device is transmitting, so there are no other incoming waves in the frame of the transmitter ($a_{lm} = 0$), then $b_o = \Gamma a_o$ and $b_{lm} = t_{lm} a_o$. Defining the total line voltage now as V_{in} , we have

$$b_{lm} = t_{lm} \frac{1}{1 + \Gamma} V_{\text{in}}. \quad (16)$$

It is enough to lump the effects of the reflection coefficient into the reciprocity relations. The source model is now

$$V_{\text{out}} = \sum_{lm} u_{lm} a_{lm} \quad (17)$$

$$b_{lm} = t_{lm} V_{\text{in}}, \quad (18)$$

with

$$u_{lm} = c_r (-1)^m t_{l,-m} \quad (19)$$

$$c_r = \frac{Z_o(1 + \Gamma)}{2\rho_o c k^2}, \quad (20)$$

where we define c_r as the reciprocity constant.

The overarching assumption is that the devices do not transmit and receive simultaneously, or, if they do, the signals can be separated, for example, by time gating.

It may be difficult or impossible to measure Z_o , Γ , and possibly the other coefficients accurately (especially with commercial ultrasound probes). However, we see that u_{lm} and t_{lm} are simply linearly proportional by systematic constants. The important part of the reciprocity relation is the dependence between u_{lm} and t_{lm} on $-m$.

C. Acoustic Propagation Model

Next we derive an acoustic propagation model relating the multipole fields of two transducers to voltage measurements between them. This model will be used later for the characterization procedure. An analogous propagation model for antenna electric fields and microwave S-parameter measurements can be found in [13].

Let there be two acoustic transducers, which could be elements on different scan heads, one transmitting in a frame i , the other receiving in a frame j . Both have their own field expansion and set of transmit and receive coefficients. Assuming no multiple scattering between the sources, the fields in each frame are expanded as

$$\phi(\mathbf{r}_i) = \sum_{lm} b_{lm}^i \psi_{lm}(\mathbf{r}_i) \quad (21)$$

$$\phi(\mathbf{r}_j) = \sum_{lm} a_{lm}^j \Re \psi_{lm}(\mathbf{r}_j), \quad (22)$$

where \mathbf{r}_i and \mathbf{r}_j are frame-centered position vectors. From the addition theorem, the multipole coefficients of the two frames are related by **AU2: Please check all equation numbers and equation citations carefully. Manuscript had a blank line numbered (23).]**

$$a_{l'm'}^j = \sum_{lm} \alpha_{l'm',lm}^{ji} b_{lm}^i, \quad (23)$$

where $\alpha_{l'm',lm}^{ji}$ is the translation matrix [17], and is evaluated with the vector that points from frame i to frame j . Using (17), (18), and (23), the input/output voltages of the two transducers are related by

$$V_{\text{out}}^j = V_{\text{in}}^i \sum_{l'm'} u_{l'm'}^j \sum_{lm} \alpha_{l'm',lm}^{ji} t_{lm}^i. \quad (24)$$

Substituting (19**AU3: into (24)?**) and taking $m' \rightarrow -m'$, we have the acoustic propagation model in terms of only transmit coefficients:

$$V_{\text{out}}^j = V_{\text{in}}^i c_r^j \sum_{l'm'} (-1)^{m'} t_{l'm'}^j \sum_{lm} \alpha_{l',-m',lm}^{ji} t_{lm}^i, \quad (25)$$

where c_r^j depends on the properties of the receiver. Eq. (25) relates the transmit coefficients of two transducers to voltage measurements between them.

D. Modified Acoustic Volume Integral Equations

Before using the VIEs in the inverse scattering algorithm, we must make them consistent with the transducer model. Like [14], in which we derived a new kernel to directly link the electrical properties of an object to microwave S-parameter measurements, we can derive an analogous kernel for the acoustic problem. This kernel directly links the object acoustic properties to measured voltages. The kernel will be a single-argument scalar function specific to the receiver, which will replace the two-argument scalar Green's function. By reciprocity, we will see that it is proportional to the transducer incident field, implying that only the incident field is required to calibrate an acoustic inverse scattering experiment.

1) *Normalized Fields:* We first define the normalized incident pressure field by substituting the transducer model into (9) when the transducer is purely transmitting.

$$\phi_{\text{inc}}(\mathbf{r}) = \sum_{lm} b_{lm} \psi_{lm}(\mathbf{r}) \quad (26)$$

$$= V_{\text{in}} \sum_{lm} t_{lm} \psi_{lm}(\mathbf{r}) \quad (27)$$

$$= V_{\text{in}} \hat{\phi}_{\text{inc}}(\mathbf{r}), \quad (28)$$

where $\hat{\phi}_{\text{inc}}(\mathbf{r})$ is the normalized incident field. It is the field given by only the transmit coefficients.

We define the normalized total field,

$$\hat{\phi}(\mathbf{r}) = \phi(\mathbf{r}) / V_{\text{in}}. \quad (29)$$

This is the same total field given by (1) but due to the normalized incident field.

2) *Receiver Kernel:* To derive the receiver kernel, we first expand the scattered field from the VIE as incoming waves in the frame of the receiver. After using the transducer model, we rearrange the expression to resemble a VIE from which we can identify the new kernel.

The addition theorem for the scalar Green's function is given by [17],

$$g(\mathbf{r}, \mathbf{r}') = ik \sum_{lm} \Re \psi_{lm}(\mathbf{r}) \psi_{lm}^*(\mathbf{r}'), \quad (30)$$

where we have taken the case $|\mathbf{r}| < |\mathbf{r}'|$. The wave function ψ^* is the same as ψ , but with the angular harmonics conjugated. Substituting (30) into (7) and rearranging, we can write the scattered field in the frame of a receiver in terms of incoming waves:

$$\phi_{\text{sca}}(\mathbf{r}) = \sum_{lm} a_{lm} \Re \psi_{lm}(\mathbf{r}), \quad (31)$$

where the multipole coefficients are

$$a_{lm} = ik \int \psi_{lm}^*(\mathbf{r}') O(\mathbf{r}') \phi(\mathbf{r}') dV'. \quad (32)$$

Substituting (32) into (17), we can write the output voltage as

$$V_{\text{out}} = ik \sum_{lm} u_{lm} \int \psi_{lm}^*(\mathbf{r}') O(\mathbf{r}') \phi(\mathbf{r}') dV'. \quad (33)$$

By rearranging this, we can identify the receiver kernel, which we label $\hat{g}(\mathbf{r}')$,

$$V_{\text{out}} = \int \hat{g}(\mathbf{r}') O(\mathbf{r}') \phi(\mathbf{r}') dV' \quad (34)$$

$$\hat{g}(\mathbf{r}') = ik \sum_{lm} u_{lm} \psi_{lm}^*(\mathbf{r}'). \quad (35)$$

The function $\hat{g}(\mathbf{r}')$ directly relates the output voltage of the receiver to the material properties of the object through the transducer model. It is the acoustic analog of the receiver kernel derived in [14] for electromagnetics.

Finally, let there be two transducers, one transmitting in frame i , the other receiving in frame j . The total pressure field in the object is due to the transmitter. Dividing both sides of (34) by the transmit voltage, we can write the scattered field VIE in terms of the normalized total field of the transmitter and the input/output line voltages as

$$\frac{V_{\text{out}}^j}{V_{\text{in}}^i} = \int \hat{g}_j(\mathbf{r}') O(\mathbf{r}') \hat{\phi}_i(\mathbf{r}') dV', \quad (36)$$

where $\hat{g}_j(\mathbf{r}')$ is the kernel for the receiver.

3) *Reciprocity Relation:* By reciprocity, we can show that $\hat{g}_j(\mathbf{r}')$ is related to the incident field of the receiver. Substituting the transmit and receive coefficient reciprocity relations, (19), into (35),

$$\hat{g}(\mathbf{r}') = ikc_r \sum_{lm} (-1)^m t_{l,-m} \psi_{lm}^*(\mathbf{r}') \quad (37)$$

and using the relation $Y_{lm}^* = (-1)^m Y_{l,-m}$ in the wave function, we get

$$\hat{g}(\mathbf{r}') = ikc_r \sum_{lm} t_{l,m} \psi_{lm}(\mathbf{r}'), \quad (38)$$

which is the expansion for the normalized incident pressure field multiplied by a scaling factor

$$\hat{g}(\mathbf{r}') = ikc_r \hat{\phi}_{\text{inc}}(\mathbf{r}'). \quad (39)$$

Finally, we write the scattered field transmit/receive voltage ratio in terms of the normalized incident field of the receiver and normalized total field of the transmitter as

$$\frac{V_{\text{out}}^j}{V_{\text{in}}^i} = -\frac{Z_o(1+\Gamma)}{i2\rho_o c k} \int \hat{\phi}_{\text{inc},j}(\mathbf{r}') O(\mathbf{r}') \hat{\phi}_i(\mathbf{r}') dV'. \quad (40)$$

This equation consistently links the material properties we wish to image to the voltages we measure. Only the normalized incident fields of the transmitters and receivers are required to do this. We will use (40) in the inverse scattering algorithm when comparing forward model predictions to measurements. This is the acoustic analog of the expression derived in [14] for microwave S-parameter measurements.

III. ULTRASOUND SOURCE CHARACTERIZATION

The next step is to determine the incident fields of the transducers, which are the quantities needed to characterize an inverse scattering experiment. The incident fields can be measured directly or computed with (27) after the transmit coefficients are found. The transmit coefficients can be estimated with simulation or determined from measurement.

We would like to determine the transmit coefficients in a way that stays within the formalism of the source-scattering model because of the rigor and versatility of the preceding derivation. Here, we discuss several aspects of this problem and the motivation for our method of choice given the experimental circumstances. Keep in mind that we intend to characterize the transducer elements of commercial hand probes.

A. Hydrophone Characterization

If the pressure field from an acoustic source can be sampled with a calibrated hydrophone, then it is possible to estimate the transmit coefficients by solving a linear inverse problem. The source model is given by

$$\phi(\mathbf{r}_n) = V_{\text{in}} \sum_{lm} t_{lm} \psi_{lm}(\mathbf{r}_n), \quad (41)$$

where \mathbf{r}_n are the locations of N hydrophone pressure field measurements, and V_{in} is the frequency component of the driving voltage. With enough measurements for a given frequency, t_{lm} is estimated by solving a linear system of equations over (41).

Although direct pressure measurements lead to the simplest estimation of the transmit coefficients, the main challenges with this approach are 1) alignment and positioning, 2) obtaining the hydrophone transfer function, and 3) repeatability. Furthermore, the pattern and frequency response of the hydrophone must be taken into account.

We are interested in characterizing multi-element commercial transducer probes. Commercial probes present a challenge to the method described here because of the dif-

faculty of positioning individual elements as well as modeling the system electronics.

B. Simulation

In our previous work characterizing antennas [13], we took advantage of the fact that we could make our antenna construction and its CAD model for our commercial simulation package (Ansoft HFSS) completely consistent. This enabled us to estimate the antenna transmit coefficients using simulated electric fields and an expression similar to (41). However, complications arise when trying to simulate ultrasound transducers for the same purpose.

First, we do not fabricate ultrasound transducers ourselves. They are an assortment of piezoelectric resonators, matching layer (to water), impedance matching (to driving circuit), grounding layer, plastic membrane, water proofing, and focusing lens [20]. It is possible to obtain a rough mechanical layout by obtaining an X-ray image of a transducer, but the exact material properties and boundary conditions are difficult to obtain. Even if all of the mechanical properties are known, simulating the electro-acoustic response requires a multi-physics simulation package which can model anisotropic piezoelectric material.

Second, the open-access package Field II [21] simulates the free-space radiation patterns of transducer apertures and arrays. However, it is based simply on the linear impulse response of ideal apertures, and does not account for the driving circuits or any mechanical features of the transducers. Thus, the simulated fields are not suitable for full-wave characterization.

Although piezoelectric transducers are difficult to fully simulate, the simplicity of CMUT transducers has allowed successful electro-mechanical simulations which agree with measurements [22]. The transmit coefficients of these devices might be estimated from simulation, which we note as possible future work.

C. Nonlinear Inversion of the Propagation Model

Without full electromechanical simulation or hydrophone measurements of our commercial transducers, the final option is to obtain the transmit coefficients by inverting the propagation model. This allows us to stay within the formalism of both the source-scattering model and modified VIEs, and estimate the transmit coefficients directly from measurement. It represents a hydrophoneless, multi-source self-calibration technique. Two or more transducers are required, with known locations and measured transmit and receive line voltages, from which pair-wise transducer responses are used to build an inverse problem around (25).

The advantage of this approach is that all the necessary physics are contained in the propagation model: translation matrices capture wave propagation, and reciprocity relates the transmit coefficients of different transducers to each other. The need for multiple pair-wise measure-

ments is satisfied by imaging setups with multi-element commercial probes. The disadvantage is that, because the transmit coefficients inherently capture the absolute phase of the radiated fields, the locations of the transducer reference frames must be known or assumed with submillimeter accuracy. We must also sample the fields throughout the region in which we intend to compute the incident field.

The propagation model is a nonlinear function of the transmit coefficients, but only polynomial to second order. The weakly nonlinear form allows us to derive a semi-analytic conjugate gradient search for the minimum of a least-squares function. This is advantageous for large data sets and fast optimizations. We develop this in the next section and will use it to estimate the transmit coefficients from measurements.

1) *Cost Function and Forward Model:* We estimate the transmit coefficients by minimizing a cost function comparing measured voltages to propagation model predictions.

Following [23], the least squares cost function for a general nonlinear problem is

$$2F(\mathbf{m}) = \|\mathbf{g}(\mathbf{m}) - \mathbf{d}\|_{\mathbf{D}}^2 + \|\mathbf{m} - \mathbf{m}_a\|_{\mathbf{M}}^2. \quad (42)$$

The vector norms are defined over model and data spaces through their respective inverse covariance matrices, \mathbf{C}_M^{-1} and \mathbf{C}_D^{-1} . The elements of the forward model vector, $\mathbf{g}(\mathbf{m})$, and data vector, \mathbf{d} , are given by

$$g^{ji}(\mathbf{m}) = c_r^j \sum_{l'm'} (-1)^{m'} t_{l'm'}^j \sum_{lm} \alpha_{l',-m',lm}^{ji} t_{lm}^i, \quad (43)$$

$$d^{ji} = \frac{V_{\text{out}}^j}{V_{\text{in}}^i}, \quad (44)$$

with the self term excluded. The vector of model parameters \mathbf{m} contains the transmit coefficients of all N transducers, written in vector form over all harmonics as

$$\mathbf{m} = \begin{bmatrix} \mathbf{t}_1 \\ \mathbf{t}_2 \\ \vdots \\ \mathbf{t}_N \end{bmatrix}. \quad (45)$$

In the case in which all the transducers in the problem are identical, the model has quadratic form, and we essentially solve the problem $c = x^2$. However, for multiple distinct transducer elements, for which each transducer has its own set of transmit coefficients, the forward model takes the form $c = xy$. In the former case, the answer is unique to within a sign. For the latter, it is impossible to uniquely separate the product of two unconstrained variables.

The properties of the forward model suggest: 1) that we should attempt to solve a self-characterization problem only when we can assume all the transducers are identi-

cal, and 2) the polynomial form enables us to derive an analytical expression for the step length in a conjugate gradient minimization, enabling a fast gradient search.

To facilitate the derivations here and in the appendix, we write the forward model in matrix notation as

$$g^{ji}(\mathbf{m}) = \mathbf{t}_j^T \mathbf{N} \mathbf{a}_{ji} \mathbf{t}_i, \quad (46)$$

where $()^T$ is vector transpose, \mathbf{N} is a diagonal matrix containing $c_T(-1)^m$, and the rows of \mathbf{a}_{ji} are evaluated at $m' \rightarrow -m'$.

2) *Gradients*: Assuming the data are independent, the gradient of the cost function with respect to the model parameters is given by

$$\hat{\gamma} = \sum_{ji} \left(\frac{\partial g^{ji}}{\partial \mathbf{m}} \right)^* \frac{1}{\sigma_{ji}^2} (g^{ji}(\mathbf{m}) - d^{ji}) + \mathbf{C}_M^{-1}(\mathbf{m} - \mathbf{m}_a), \quad (47)$$

where $\partial g^{ji}/\partial \mathbf{m}$ is the vector of partial derivatives of the forward model with respect to the model parameters.

The partial derivatives of (47) are computed with the help of these matrix identities: **[AU4: Is the superscript capital T supposed to be a superscript lowercase t to indicate a vector transpose as in (46)?]**

$$\frac{\partial \mathbf{x}^T \mathbf{B} \mathbf{x}}{\partial \mathbf{x}} = (\mathbf{B} + \mathbf{B}^T) \mathbf{x} \quad (48)$$

$$\frac{\partial \mathbf{x}^T \mathbf{a}}{\partial \mathbf{x}} = \frac{\partial \mathbf{a}^T \mathbf{x}}{\partial \mathbf{x}} = \mathbf{a}. \quad (49)$$

If the transducers are identical, $\mathbf{t} = \mathbf{t}_j = \mathbf{t}_i$, for all i and j , then

$$\frac{\partial g^{ji}}{\partial \mathbf{t}} = (\mathbf{N} \mathbf{a}_{ji} + (\mathbf{N} \mathbf{a}_{ji})^T) \mathbf{t}. \quad (50)$$

If the transducers are different, then the gradients are

$$\frac{\partial g^{ji}}{\partial \mathbf{t}_i} = (\mathbf{N} \mathbf{a}_{ji})^T \mathbf{t}_j \quad (51)$$

$$\frac{\partial g^{ji}}{\partial \mathbf{t}_j} = \mathbf{N} \mathbf{a}_{ji} \mathbf{t}_i. \quad (52)$$

3) *Conjugate Gradient Updates*: Regardless of whether we are solving for identical or different transducer transmit coefficients, the conjugate gradient updates are defined

$$\mathbf{m}_n = \mathbf{m}_{n-1} - \alpha_n \mathbf{v}_n \quad (53)$$

$$\mathbf{v}_n = \gamma_n + \beta_n \mathbf{v}_{n-1}, \quad (54)$$

where α_n is the step length and γ_n is the steepest decent vector. β_n is given by

$$\beta_n = \frac{\langle \mathbf{C}_M^{-1}(\gamma_n - \gamma_{n-1}), \gamma_n \rangle}{\langle \mathbf{C}_M^{-1} \gamma_{n-1}, \gamma_{n-1} \rangle}, \quad (55)$$

where $\langle \cdot \rangle$ is a simple dot product.

The step length α_n is found by minimizing the cost function at each step. Given the form of the forward model, this can be done analytically as described in the appendix.

4) *Summary of Optimization Routine*: We derived a nonlinear optimization routine to invert the acoustic propagation model for the transducer transmit coefficients given pair-wise voltage responses. All of the preceding steps were used to implement this routine. Experimental results follow in the next section.

Much time was spent analyzing this inversion routine in simulation. Results obtained in our simulations were consistent with the algorithm presented here. With perfect data and perfect knowledge of the source locations, the transmit coefficients for multiple identical sources could be recovered uniquely to within a sign, from a wide range of initial conditions. It was also determined that when solving for multiple different transducer transmit coefficients, that the synthetic measured data could be fit quite well, but the solution was not correct and dependent on the initial condition, demonstrating non-uniqueness.

IV. ULTRASOUND PROBE CHARACTERIZATION EXPERIMENT

To test the nonlinear source characterization in the previous section, we built the setup shown in Fig. 2. This setup was also used for the inverse scattering (see next section) so that the characterization and imaging were performed in identical geometries. Two commercial Phillips ATL L7-4 transducers **[AU5: Please provide manufacturer name and location.]** were mounted facing each other in a water tank. Each probe had 128 transducer elements in a linear array. The probes were connected to a Verasonics data acquisition system, which was programmed to collect all combinations of transmit and receive signals between the opposite-side elements. The mount was custom made out of king starboard. **[AU6: Please provide manufacturer name and location.]** The mounting holes are separated by 1 cm to allow linear translation of the probes relative to one another. The blue holders were created with the help of the University of Michigan 3-D Lab. The probes were laser scanned and the scan was used to create a 3-D CAD model of the holders. The holders were then fabricated with a 3-D printing system.

We took transmission measurements in probe positions that would sweep out the imaging domain. This allowed us to sample the field both at points in the imaging domain as well as at the receiver locations. This setup, however, restricts our field samples to a plane, which is a compromise we made to avoid more involved 3-D geometries. The

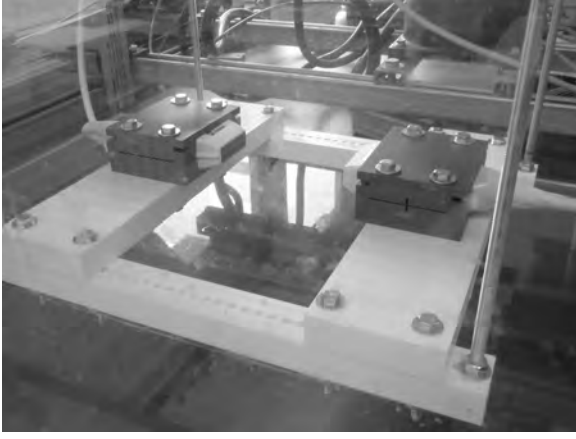



Fig. 2. Photo of setup for nonlinear source characterization and inverse scattering experiment. 

transducer elements of the L7-4 probe are known to be 4 mm tall, 0.3 mm wide, with a spacing of 0.4 mm.

Transmitted signals were two cycle pulses with a 5 MHz center frequency, which was the center frequency used for the position optimization in the next section. The Verasonics system was set to sample at 4 samples per wavelength, giving a sample rate of 20 MHz. In water, the wavelength at 5 MHz is 300 μm . The characterization and imaging were performed at 3.75 MHz, where the wavelength is 400 μm in water.

A. Position Inversion and Virtual Sources

Before performing the characterization, we must know or assume the locations and orientations of the transducer reference frames. This is not easily done mechanically because of the probably imprecise positioning of the transducer elements in the transducer housing, so we use time of flight. The time of flight is recorded between all (or many) elements on the opposing probes and used to solve a triangulation problem for the position and orientation of one array relative to the other. We assume we know the spacing of the array elements and that all the elements lie on a line.

We mention several experimental conditions. We use time zero of the time traces as a common reference, because the receive channels of the Verasonics begin recording at the same time on each occurrence of a transmit pulse. The identical timing of the channels is the only common reference between all transmit and receive data. Second, this allows measurements of the delay in firing of the transmit pulse equivalent to about one wavelength. Third, each transducer has a lens on its face with a lower speed of sound. This lens is designed to focus the radiation from each element in the elevation direction, so that focused beams used for everyday diagnostic ultrasound are restricted to a thin plane out to a modest distance from the transducer. This lens introduces a delay on both the transmit and receive signals. Last, the pulse may be de-

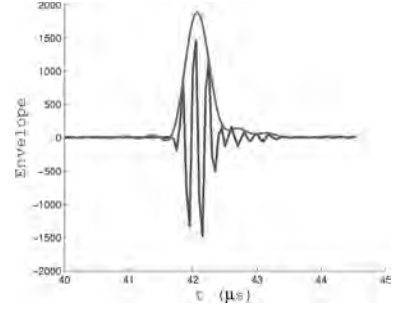



Fig. 3. Envelope of time trace. The time of flight is determined by the time of the envelope maximum less half the pulse width. 

layed either by the system, the cables, or probe head, and we may not be able to quantify this delay.

We measured the time of flight relative to the beginning of the time trace using an envelope-max, shown in Fig. 3. The firing delay was accounted for by subtracting half a pulse length in water from the time of flight measured at the peak of the envelope. To properly account for the delay induced by the lenses, one approach is to solve Fermat's least action integral for the two-layered boundary, which we did not do here because the properties of the lens were not known.

The effects of not accounting for the lenses, or other delays, in a time of flight position estimation are that we will find the location of a virtual source behind the actual source location. We rationalize this as follows: 1) accounting for the lens in the propagation model inversion is not trivial, and 2) if the lenses do not adversely affect the radiation pattern in the azimuth plane (the plane of the array), then, using the virtual positions, we can solve for the transmit coefficients of equivalent sources at the virtual locations. In doing so, the effects of the lenses are accounted for by a free-space spatial offset. Finally, if we are finding virtual source locations and transmit coefficients, we can now also lump the effects of miscellaneous system delays into the virtual source location. This was the reasoning going forward and the assumptions under which we performed the following computations and experiments. Fig. 4 shows a diagram of the transition from what we believe to be the actual system to the virtual source configuration.

The forward model for the position inversion is diagrammed in Fig. 5 and is given by

$$t_{ij} = r_{ij}/c \quad (56)$$

$$r_{ij} = |-(\mathbf{c}_1 + d_i \hat{\mathbf{v}}_1) + \mathbf{c}_2 + d_j \hat{\mathbf{v}}_2| \quad (57)$$

$$d_i = ((128 + 1)/2 - i)d, \quad i = 1 \dots 128 \quad (58)$$

$$d_j = ((128 + 1)/2 - j)d, \quad j = 1 \dots 128, \quad (59)$$

where t_{ij} is the time of flight between two elements, c is the speed of sound in water, and r_{ij} is the distance between two elements. The vectors \mathbf{c}_1 and \mathbf{c}_2 point to the centers of each array. The vectors $d_i \hat{\mathbf{v}}_1$ and $d_j \hat{\mathbf{v}}_2$ point to

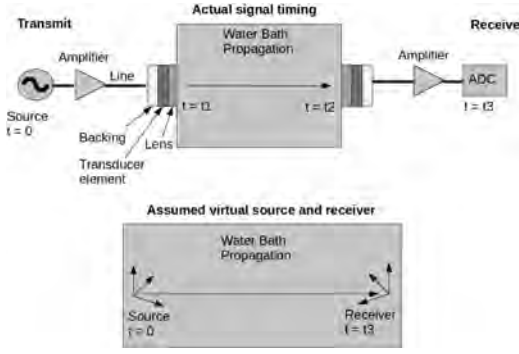


Fig. 4. Actual and virtual sources and receivers. The signal fires at t_0 , emanates from the transducer at t_1 , arrives at the receiving transducer at t_2 , and is recorded at t_3 . The virtual source and receiver lump any delays into a spatial offset.

the locations of the array elements, with d being the separation of the elements.

B. Speed of Sound in Water

The speed of sound of the water bath was determined by the temperature at the time the data were taken and the lookup table in [24]. This was periodically cross checked with pulse-echo reflections off a plate for a transducer stepped on a micrometer. The two methods agreed to within 0.1% at 3.75 MHz for speeds around 1495 m/s at 24.3°C.

C. Position Inversion Results

After determining the times of flight between all elements, we minimized an L1 cost functional over (56); the L1 norm was used to automatically eliminate outliers in the time of flight data created by the envelope search.

We solved for the location and orientation of the second transducer relative to the first. Thus, we let $\mathbf{c}_1 = 0$ and $\hat{\mathbf{v}}_1 = \hat{\mathbf{x}}$ and the six model parameters are then the elements of the vectors \mathbf{c}_2 and $\hat{\mathbf{v}}_2$. The initial conditions used were $\mathbf{c}_{2,0} = c * t_{\text{center}} \hat{\mathbf{y}}$, where t_{center} is the time of flight between the two center elements and $\hat{\mathbf{v}}_{2,0} = -\hat{\mathbf{x}}$, which assumes that the arrays are initially parallel and centered.

This optimization was performed for seven positions. The results are shown in Fig. 6. The probe position separations were consistent with our 1 cm spacing, but the re-

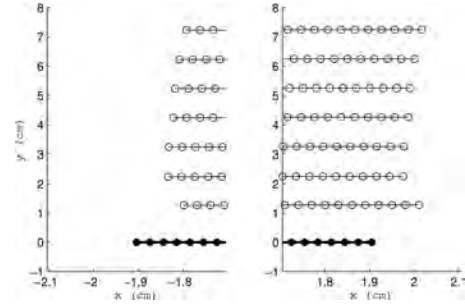


Fig. 6. Split plot of the probe element positions. Filled circles are the element locations of probe 1 (reference). Open circles are the element locations of probe 2 for all seven positions based on the position inversion. The y -axis is compressed.

ceive array was shifted along the array direction by nearly a millimeter. This was confirmed visually, and corresponds to a translation equivalent to several array elements. We ignored the z coordinate offset and z orientation component, because 1) the position inversion is not sensitive to that dimension unless the array is grossly tilted in the x - z plane, and 2) these variations are small compared with variation in the element radiation patterns in the elevation direction.

D. Characterization Results

Having estimated the locations of the sources, we then estimated the transmit coefficients using the method outlined in Section III-C. We did this in the frequency domain at 3.75 MHz, which was then the frequency used for imaging. Although more frequencies ultimately help the inverse scattering algorithm, a single frequency is sufficient to confirm that the characterization and imaging algorithm work together. This frequency was the lowest at which we could drive the transducers for clean signals; lower frequencies allow more freedom for phase and position errors.

Although the derivation of (40) is rigorous, we mention the problem of determining the systematic constants in the context of this experiment. These include Z_0 , Γ , and the Verasonics system electronics transfer functions, which would convert sampled signals to absolute voltages. We did not measure these for the following reasons. By determining the transmit coefficients in the same system configuration used to take data for the inverse scattering, the constants carry through to the computation of the normalized incident field in the VIE. In other words, we estimate scaled transmit coefficients using digitized voltage data. The same transmit coefficients are used to compute the normalized incident fields in the VIEs. To port the transmit coefficients to another system, new constants would have to be determined.

Because we cannot take data out of plane, we only need to describe the element radiation pattern in the imaging plane, and so we chose to invert for multipole harmonics up to $l = 8$. We assumed all transducer elements are identical.

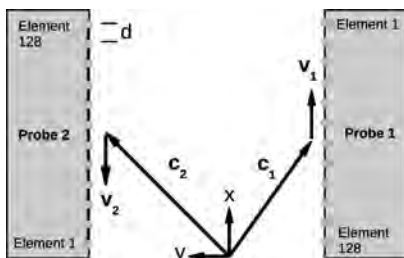


Fig. 5. Diagram for position estimation problem. The vectors \mathbf{c}_2 and \mathbf{c}_1 point to array centers, \mathbf{v}_1 and \mathbf{v}_2 point from the array centers to element locations, and d is the element spacing.

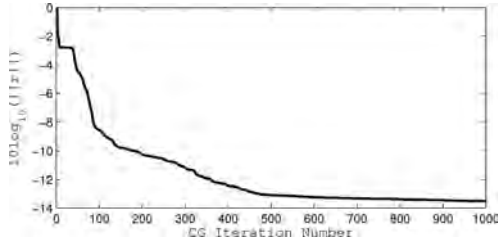


Fig. 7. Normalized residual as a function of conjugate gradient iteration number.

The frames of elements on the second probe were rotated by means of rotation matrices in the propagation model [13]. After many trials, we found the best results by using data from a subset of elements from each probe and a few positions. For the presented examples, we used data from every tenth element and two positions to obtain the results below. These were chosen to subsample each array and avoid underfitting.

Fig. 7 shows the residual with each iteration of conjugate gradient minimization. The residual drops monotonically, meaning that our algorithm was coded correctly. The behavior of the residual is more complicated than for a typical linear problem; the residual of a linear problem would look smoothly logarithmic.

Fig. 8 shows the real and imaginary parts of the estimated transmit coefficients. This plot is essentially the spectral power of each multipole index in the radiation pattern of the elements.

Fig. 9 shows the measured and predicted magnitude and phase of the data for a small subset of transmitter-receiver pairs after the transmit coefficients were found. The groups are receivers per transmitter. We see that the overall shape of the magnitude is well fitted, and that the

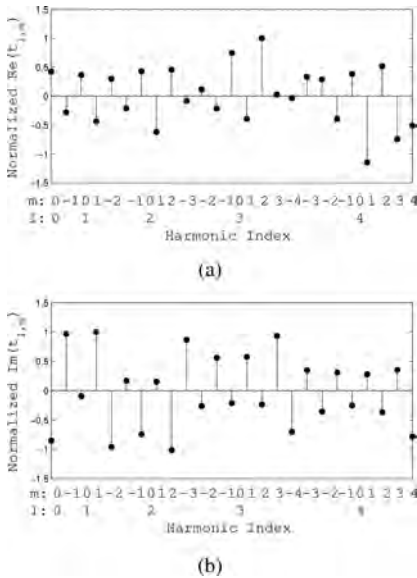


Fig. 8. Normalized transmit coefficients: (a) real part and (b) imaginary part. Horizontal axis is the (l, m) harmonic index.

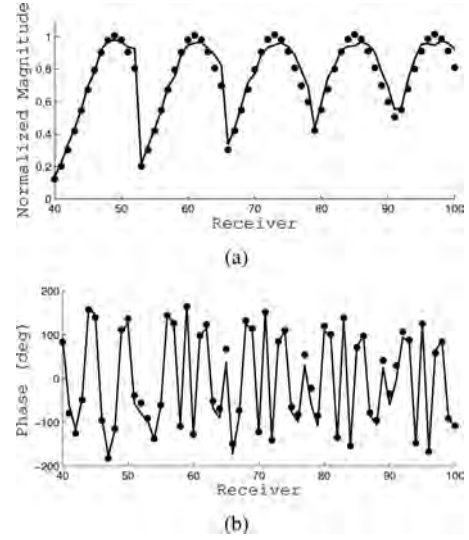


Fig. 9. (a) Magnitude and (b) phase of measured and predicted data for a sampling of transmit and receive elements. The apparent groups in the magnitude plot are receivers for a given transmit element.

phase is fit well, to within 20° . This indicates that the inversion was working to correctly fit the data.

The normalized pressure field computed with the transmit coefficients is shown in Fig. 10. This is the normalized magnitude in the plane of the probes, and is the incident field we will use in the inverse scattering algorithm. The asymmetric side lobes come from having incomplete information in those directions; the fields are only constrained where we took data with the second probe.

V. ULTRASOUND INVERSE SCATTERING EXPERIMENT

We formed images of compressibility and absorption with the acoustic inverse scattering algorithm in [9]. The algorithm is based on the Born iterative method (BIM) with Neumann series forward scattering solver. We replaced the scattered field VIE in that algorithm with the modified VIE of (40), and used normalized incident fields computed with the estimated transmit coefficients.

We formed images of the 2-D cross section of cylindrical targets using the full 3-D inverse scattering algorithm using transmission data only. Because of the limited angle

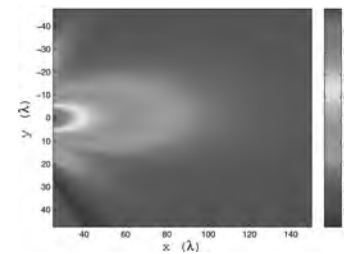


Fig. 10. Normalized magnitude of acoustic field in the transducer plane computed with the solved transmit coefficients. Colorscale is normalized acoustic field magnitude (unitless).



Fig. 11. Photo of 6-axis positioning arm used to place and rotate objects and close-up of metal rod.

acquisition geometry of the opposing probes, we rotated the objects to adequately sample the scattered fields. The objects hung from the metal rod and are weighed down. We assumed the imaging domain was very thin and ignored out-of-plane scattering. The modified algorithm was tested in simulation with this geometric configuration and the transmit coefficients estimated previously, which confirmed that the inversion algorithm and forward solver were self-consistent, the details of which are not included here.

Several objects were used to test the inverse scattering algorithm. The objects consisted of metal, plastic, and worm rubber cylinders. The hard objects tested resolution. Worm rubber has a speed of sound less than water and attenuation greater than water and was used to test the contrast.

A. Rotator Alignment

We rotated the objects using the six-axis robotic arm shown in Fig. 11. Given the sensitivity of the algorithm to position errors, we aligned the center of rotation as best we could at the coordinate center of the object domain. A smooth metal cylindrical rod was attached to the center of the last arm axis. This rod was used for attaching objects and was aligned in the x - and y -directions using pulse echo measurements.

B. Image Reconstructions

We formed images at 3.75 MHz using 12 or 36 object rotations and a subset of transmitters and receivers on each probe. The imaging domain was about 2 cm on a side.

1) *Example 1: Worm Rubber Cylinder:* An approximately 4-mm diameter cylinder of worm rubber was imaged [Fig. 12(a)]. From mass/volume measurements of the worm rubber samples, their density was 1.02 g/cm³. The speed of sound was estimated from differential time of flight to be 1406 m/s. From this, the compressibility was determined to be 4.98e-10 1/N, which equates to a contrast with water of 0.102. Attenuation coefficient was measured separately at 3.75 MHz as 3.2 dB/cm/MHz [25]. Twelve rotations of 30° each were used for this object.

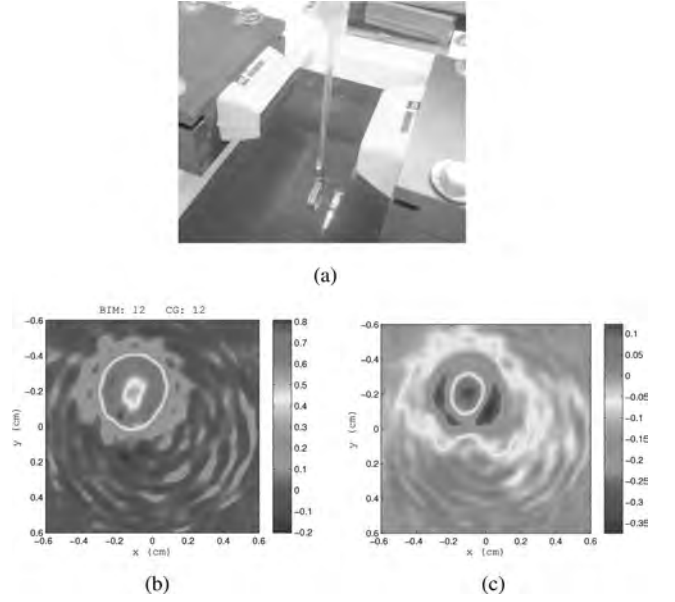


Fig. 12. (a) Photo of worm rubber target. (b) Recovered compressibility contrast, $\delta\kappa$, (colormap: unitless), and (c) absorption contrast, $\delta\alpha$, (colormap: units of compressive loss Pa⁻¹s⁻¹).

Figs. 12(b) and 12(c) show images formed by the inverse scattering algorithm of compressibility contrast, $\delta\kappa$, and absorption contrast, $\delta\alpha$, respectively, as defined by (4) and (5). The inverse scattering algorithm was terminated after 12 BIM steps with 12 conjugate gradient steps per iteration. The object location, shape, and approximate size are recovered. The value of compressibility is too large by a factor of six and the absorption shows a ring artifact. These are most likely due to the thin imaging domain, in which the recovered values are trying to compensate the predicted scattered fields. This effect is discussed in more detail in the next section. However, the signs of the two contrasts are correct, which indicates that (40) was derived correctly. Similar effects are present in the examples that follow. The streaks along the outside of the imaging domain are rotation artifacts.

2) *Example 2: Two Metal Filaments:* We imaged two thin metal filaments to test resolution, even though the material hardness is not captured by the physics of the inverse scattering algorithm. The filaments are shown in Fig. 13(a). The rods were brass with 0.5 mm diameter and separated by approximately 2 mm.

Figs. 13(b) and 13(c) show images formed by the inverse scattering algorithm of compressibility contrast, $\delta\kappa$, and absorption contrast, $\delta\alpha$, respectively. The inverse scattering algorithm was terminated after 5 BIM steps. The object location and shape of the object are recovered. The compressibility contrast is negative and absorption is positive. This is the correct direction for compressibility, because we expect the compressibility of brass to be less than water. The ringing artifacts and streaks are due to the use of only twelve rotations.

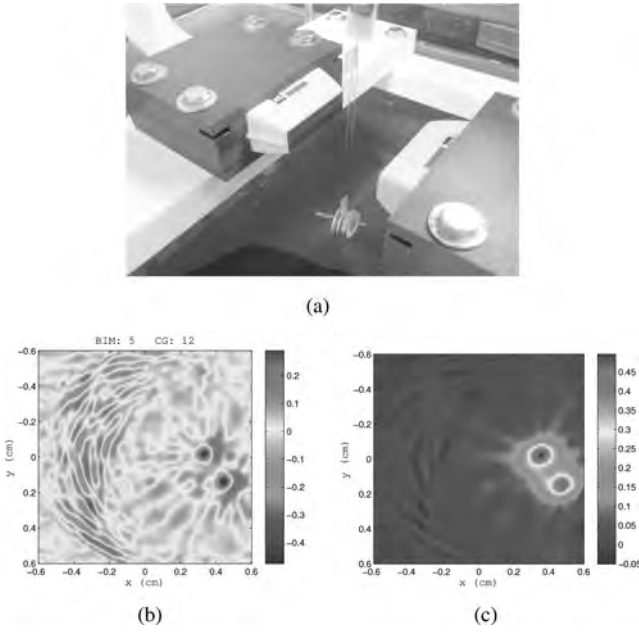


Fig. 13. (a) Photo of two metal filaments. (b) Recovered compressibility contrast, $\delta\kappa$, (colourscale: unitless), and (c) absorption contrast, $\delta\alpha$, (colourscale: units of compressive loss $\text{Pa}^{-1}\text{s}^{-1}$).

VI. DISCUSSION

The goal of this work was to extend our source characterization work in experimental microwave inverse scattering [13]–[15] to the problem of characterizing commercial transducer probes for transmission acoustic inverse scattering. The two main challenges were 1) the small spatial scales of acoustic waves and 2) the need to characterize transducers using measurements instead of simulation. These two differences motivated the derivation of a self-characterization method for commercial probes based on nonlinear inversion of an acoustic propagation model. We derived the propagation model in Section II-C and the nonlinear inversion in Section III-C. The method allowed us to estimate the transducer transmit coefficients from pair-wise measurements. We further derived a modified scattered field VIE in Section II-D so that, once the transmit coefficients were estimated, the incident fields computed with them were rigorously linked to volume integrals of the inverse scattering algorithm. We also used an additional optimization with time of flight to solve for the positions of the two probes. Several experimental assumptions were necessary given the available setup, but these were limited as much as possible.

From the results of the characterization and imaging, together with the assumptions of the experiment, the method showed reasonable success. The characterization inversion fit the data well. The targets were mostly recovered and the signs of their quantitative values followed physical expectations. Without the transducer model, the inversion produced contrasts with flipped signs and contrasts that were too large by an order of magnitude.

A major assumption affecting image quality and interpretation was imaging 2-D slices of inherently 3-D objects. This was necessary given the limited data acquisition geometry, where we assumed the cylindrical geometry and long distances would allow us to ignore out of plane scattering. This assumption likely contributed to the contrast values being too high. To illustrate this, we ran an idealized simulation showing the effects of object reconstruction in a thin-3-D domain when scattered fields are generated from a thick-3-D domain. Ideal point-sources in the same geometry as the experiments are used. The object consists of two cylinders, both with compressibility contrast of 0.1, shown in Fig. 14(a). The thick-3-D domain is $8 \times 8 \times 10 \lambda$, whereas the thin-3-D domain is $8 \times 8 \times 1 \lambda$, where $\lambda = 0.4 \text{ mm}$. Scattered fields are generated from the cylinders in the thick domain. Fig. 14(b) is the 2-D profile of the object reconstructed in the thick-3-D domain; Fig. 14(c) shows the object reconstructed in the thin domain. The peak contrast of the object reconstructed in the thin domain is overestimated by a factor of 9. In simulated examples, such as this, overestimation scales with the ratio of domain thicknesses, because the algorithm is trying, in effect, to conserve the scattered field power radiated by the objects in each domain.

Finally, we did not have independent confirmation of the accuracy of the forward-scattering model, i.e., the combination of the estimated transmit coefficients, computed incident fields, and scattered field predictions by the new VIE. This would have required the precise position and material properties of known targets, which was not possible with this experimental setup. Motion undoubtedly contributed to image artifacts as well.

VII. CONCLUSION

We derived and provided initial experimental testing of a new self-characterization method for commercial ultrasound probes which was designed for transmission inverse scattering. We first modified the traditional volume integral equations to make them consistent with the transducer model. This was an extension of our previous work modeling antennas for electromagnetic inverse scattering. We then derived an optimization procedure based on the nonlinear inversion of an acoustic propagation model to obtain the transducer transmit coefficients from measured data. We described our two-probe experiment, including provisions to estimate the probe locations and align a robotic rotator. The characterization results showed that the inversion fit the measured data well. We then tested our inverse scattering algorithm with modified volume integral equations. The images showed that the values of the contrasts of simple objects were physically consistent with expected values, but image quality suffered from assumptions inherent in the experimental setup. This is the groundwork for future better versions of full-wave calibration with other transducers and imaging algorithms, with-

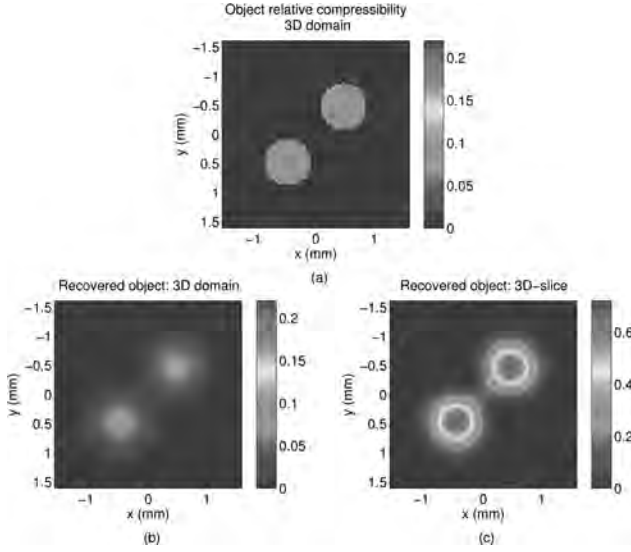


Fig. 14. Comparison of reconstructions on domains of different thickness given identical scattered fields. (a) Object: two cylinders with compressibility contrast of 0.1. Scattered fields are generated from a domain with a thickness of 10λ . (b) 2-D profile of the reconstruction on a 10λ -thick domain. (c) 2-D profile of the same object reconstructed on a 1λ -thick domain; the contrasts are overestimated by a factor of 6 (note an increased colorscale).

out which we will not be able to improve ultrasound much beyond what has been the state of the art for many years.

The transducer model and modified VIE are rigorous and versatile, but further investigation is required to better evaluate the performance of the nonlinear characterization and acoustic imaging algorithm. In future work, we will explore using simulation to obtain the transducer transmit coefficients, and explore viable options for independent validation of the forward-scattering model at ultrasound spatial scales. The propagation model could also be used to include the full radiation and phase patterns of hydrophones for hydrophone characterization of transducers.

APPENDIX STEP LENGTH

We choose α_n to minimize the cost function at each step. Substituting the expression for \mathbf{m}_n into the cost function,

$$2F(\mathbf{m}_n) = \|\mathbf{g}(\mathbf{m}_{n-1} - \alpha_n \mathbf{v}_n) - \mathbf{d}\|_D^2 + \|\mathbf{m}_{n-1} - \alpha_n \mathbf{v}_n - \mathbf{m}_a\|_M^2. \quad (60)$$

Because this forward model is only polynomial nonlinear, we will obtain a polynomial in α , the minimum of which can be found using standard algebraic techniques. To help the bookkeeping, we first write the forward model in matrix notation with two generic model vectors representing receivers and transmitters

$$g^{ji}(\mathbf{a}, \mathbf{b}) = \mathbf{a}_j^t \mathbf{N} \mathbf{a}_{ji} \mathbf{b}_i, \quad (61)$$

where \mathbf{a} and \mathbf{b} are model vectors for receiver and transmitter positions, respectively. After substituting the update step, and rearranging,

$$\mathbf{g}(\mathbf{m}_n) = \mathbf{g}(\mathbf{m}_{n-1}, \mathbf{m}_{n-1}) - \alpha_n (\mathbf{g}(\mathbf{m}_{n-1}, \mathbf{v}_n) + \mathbf{g}(\mathbf{v}_n, \mathbf{m}_{n-1})) + \alpha_n^2 \mathbf{g}(\mathbf{v}_n, \mathbf{v}_n). \quad (62)$$

Substituting this into the cost function, we have

$$2F(\mathbf{m}_n) = \|\mathbf{r}_{n-1} - \alpha_n \mathbf{g}_1 + \alpha_n^2 \mathbf{g}_2\|_D^2 + \|\mathbf{c}_{n-1} - \alpha_n \mathbf{v}_n\|_M^2, \quad (63)$$

where

$$\mathbf{r}_{n-1} = \mathbf{g}(\mathbf{m}_{n-1}, \mathbf{m}_{n-1}) - \mathbf{d} \quad (64)$$

$$\mathbf{g}_1 = \mathbf{g}(\mathbf{m}_{n-1}, \mathbf{v}_n) + \mathbf{g}(\mathbf{v}_n, \mathbf{m}_{n-1}) \quad (65)$$

$$\mathbf{g}_2 = \mathbf{g}(\mathbf{v}_n, \mathbf{v}_n) \quad (66)$$

$$\mathbf{c}_{n-1} = \mathbf{m}_{n-1} - \mathbf{m}_a. \quad (67)$$

The term $\mathbf{g}(\mathbf{m}_{n-1}, \mathbf{v}_n)$ treats \mathbf{m}_{n-1} as receivers and \mathbf{v}_n as sources, whereas $\mathbf{g}(\mathbf{v}_n, \mathbf{m}_{n-1})$ does the opposite. Writing out the vector norms

$$\begin{aligned} 2F(\mathbf{m}_n) = & \|\mathbf{r}\|_D^2 - \alpha \mathbf{r} \cdot \mathbf{g}_1 + \alpha^2 \mathbf{r} \cdot \mathbf{g}_2 \\ & - \alpha \mathbf{g}_1 \cdot \mathbf{r} + \alpha^2 \|\mathbf{g}_1\|_D^2 - \alpha^3 \mathbf{g}_1 \cdot \mathbf{g}_2 \\ & + \alpha^2 \mathbf{g}_2 \cdot \mathbf{r} - \alpha^3 \mathbf{g}_2 \cdot \mathbf{g}_1 + \alpha^4 \|\mathbf{g}_2\|_D^2 \\ & + \|\mathbf{c}\|_M^2 - \alpha \mathbf{c} \cdot \mathbf{v} - \alpha \mathbf{v} \cdot \mathbf{c} + \alpha^2 \|\mathbf{v}\|_M^2 \end{aligned} \quad (68)$$

and using the fact that $(\mathbf{a}, \mathbf{b}) = (\mathbf{b}, \mathbf{a})^*$, we can write this as a quartic polynomial in α_n :

$$F(x) = ax^4 + bx^3 + cx^2 + dx + e, \quad (69)$$

where

$$x = \alpha \quad (70)$$

$$a = \|\mathbf{g}_2\|_D^2 \quad (71)$$

$$b = -2\Re(\mathbf{g}_1, \mathbf{g}_2)_D \quad (72)$$

$$c = \|\mathbf{g}_1\|_D^2 + 2\Re(\mathbf{r}, \mathbf{g}_2)_D + \|\mathbf{v}\|_M^2 \quad (73)$$

$$d = -2\Re(\mathbf{r}, \mathbf{g}_1)_D - 2\Re(\mathbf{c}, \mathbf{v})_M \quad (74)$$

$$e = \|\mathbf{r}\|_D^2 + \|\mathbf{c}\|_M^2. \quad (75)$$

Next, we must find the minimum of $F(x)$ with respect to x . The first and second derivatives of the quartic are given by

$$F'(x) = 4ax^3 + 3bx^2 + 2cx + d \quad (76)$$

$$F''(x) = 12ax^2 + 6bx + 2c. \quad (77)$$

The leading term of the second derivative shows us that this quartic will, globally, always be convex, because a is a square vector norm and always greater than zero. For a convex quartic, there is either one global minimum, or there are at most 2 local minima and 1 local maximum. We can separate these cases by finding the zeros of $F'(x)$, for which there is either 1 real root and two complex conjugate roots (i.e., 1 global minimum of the quartic), or 3 real roots (i.e., 2 local minima and 1 local maximum of the quartic). In the latter case, we find the global minimum by back substitution; any ambiguity that might arise from identical local minima (i.e., different possible step lengths) has not been observed in practice to be a problem. A cubic is one of the few polynomials for which the zeros can be determined analytically. There are several methods, which can be found in standard math texts.

ACKNOWLEDGMENTS

The authors thank the University of Michigan Basic Radiological Sciences Ultrasound Group for the use of laboratory space, the Verasonics data acquisition systems, and the positioning equipment. The authors also thank F. M. Hooi for help with the experiments.

REFERENCES

- [1] F. Simonetti, L. Huang, and N. Duric, "Transmission and reflection diffraction tomography in breast imaging," in *Int. Conf. Biol. Medical Eng. and Info.*, 2008, pp. 723–727. **[AU7: Please spell out all conference names.]**
- [2] D. Borup, S. Johnson, B. Hanover, K. Callahan, M. Andre, and J. Wiskin, "Performance of an automated whole-breast ultrasound imaging system employing full-wave 3D inverse-scattering CT," *RSNA*, 2008, art. no. LL-PH2151-R09. **[AU8: Is this a conference paper? Please spell out name of source.]**
- [3] S. A. Johnson, D. T. Borup, J. W. Wiskin, F. Natterer, F. Wubeling, Y. Zhang, and S. C. Olsen, U.S. Patent No. 6005916, 1999. **[AU9: Please provide patent title and date of issue.]**
- [4] C. Li, N. Duric, and L. Huang, "Breast imaging using transmission ultrasound: Reconstructing tissue parameters of sound speed and attenuation," in *Int. Conf. BioMedical Eng. and Info.*, 2008, pp. 708–712.
- [5] M. P. Andre, H. S. Janee, P. J. Martin, G. P. Otto, B. A. Spivey, and D. A. Palmer, "High-speed data acquisition in a diffraction tomography system employing large-scale toroidal arrays," *Int. J. Imaging Sys. Tech.*, vol. 8, no. 1, pp. 137–147, 1997.
- [6] N. Duric, L. Cuiping, C. Glide-Hurst, P. Littrup, L. Huang, J. Lupinacci, S. Schmidt, O. Rama, L. Bey-Knight, and Y. Xu, "Breast imaging with ultrasound tomography: Clinical results at the Karmanos Cancer Institute," in *Int. Conf. Biol. Medical Eng. and Info.*, 2008, pp. 713–716.
- [7] N. Duric, P. Littrup, A. Babkin, D. Chambers, S. Azevedo, K. Arkady, R. Pevzner, M. Tokarev, and E. Holsapple, "Development of ultrasound tomography for breast imaging: Technical assessment," *Med. Phys.*, vol. 32, no. 5, pp. 1375–1386, 2005.
- [8] R. Leach, Jr., S. G. Azevedo, J. G. Berryman, H. Bertete-Aguirre, D. H. Chambers, J. E. Mast, P. J. Littrup, N. Duric, S. A. Johnson, and F. Wuebbeling, "Comparison of ultrasound tomography methods in circular geometry," in *Proc. SPIE, Med. Img.: Ultra. Img. and Sig. Proc.*, 2002, pp. 362–377.
- [9] M. Haynes and M. Moghaddam, "Large-domain, low-contrast acoustic inverse scattering for ultrasound breast imaging," *IEEE Trans. Biomed. Eng.*, vol. 57, no. 11, pp. 2712–2722, 2010.
- [10] P. Huthwaite and F. Simonetti, "High-resolution imaging without iteration: A fast and robust method for breast ultrasound tomography," *J. Acoust. Soc. Am.*, vol. 130, no. 3, pp. 1721–1734, 2011.
- [11] G. R. Pratt, H. Lianjie, N. Duric, and P. Littrup, "Sound-speed and attenuation imaging of breast tissue using waveform tomography of transmission ultrasound data," in *SPIE Proc. Medical Imaging*, 2007, vol. 6510, art. no. 65104S.
- [12] P. Huthwaite, F. Simonetti, and N. Duric, "Combining time of flight and diffraction tomography for high resolution breast imaging: Initial in vivo results," *J. Acoust. Soc. Am.*, vol. 132, no. 3, pp. 1249–1252, 2012.
- [13] M. Haynes and M. Moghaddam, "Multipole and S-parameter antenna and propagation model," *IEEE Trans. Antenn. Propag.*, vol. 59, no. 1, pp. 225–235, 2011.
- [14] M. Haynes and M. Moghaddam, "Vector Green's function for s-parameter measurements of the electromagnetic volume integral equation," *IEEE Trans. Antenn. Propag.*, vol. 60, no. 3, pp. 1400–1413, 2012.
- [15] M. Haynes, S. Clarkson, and M. Moghaddam, "Electromagnetic inverse scattering algorithm and experiment using absolute source characterization," *IEEE Trans. Antenn. Propag.*, vol. 60, no. 4, pp. 1854–1867, 2012.
- [16] M. Haynes, J. Stang, and M. Moghaddam, "Microwave breast imaging system prototype with integrated numerical characterization," *Int. J. Biomed. Imaging*, vol. 2012, art. no. 706365, 2012.
- [17] W. C. Chew, *Waves and Fields in Inhomogeneous Media*. Piscataway, NJ: IEEE Press, 1995.
- [18] A. D. Yaghjian, "Scattering-matrix analysis of linear periodic arrays," *IEEE Trans. Antenn. Propag.*, vol. 50, no. 8, pp. 1050–1064, 2002.
- [19] R. A. Shore and A. D. Yaghjian, "Scattering-matrix analysis of linear periodic arrays of short electric dipoles," Technical Report AF-RL-SN-HS-TR-2004-045, Air Force Research Laboratory In-House Report, 2004.
- [20] E. P. Papadakis, *Ultrasonic Instruments and Devices*. San Diego, CA: Academic Press, 1999, ch. 1, pp. 1–45.
- [21] J. A. Jensen and N. B. Svendsen, "Calculation of pressure fields from arbitrarily shaped, apodized, and excited ultrasound transducers," *IEEE Trans. Ultrason. Ferroelectr. Freq. Control*, vol. 39, no. 2, pp. 262–267, 1992.
- [22] G. G. Yaralioglu, S. A. Ergun, and B. T. Khuri-Yakub, "Finite-element analysis of capacitive micromachined ultrasonic transducers," *IEEE Trans. Ultrason. Ferroelectr. Freq. Control*, vol. 52, no. 12, pp. 2185–2198, 2005.
- [23] A. Tarantola, *Inverse Problem Theory*. Philadelphia, PA: SIAM Press, 2005.
- [24] N. Bilaniuk and G. S. K. Wong, "Speed of sound in pure water as a function of temperature," *J. Acoust. Soc. Am.*, vol. 93, no. 3, pp. 1609–1612, 1993.
- [25] F. M. Hooi, "Optimized beamforming and limited angle tomography of the compressed breast," Ph.D. Dissertation, Dept. of Biomedical Engineering, University of Michigan, Ann Arbor, MI, 2012.

Authors' photographs and biographies were unavailable at time of publication. **[AU10: Do you wish to submit bios?]**

Acceleration of ultrasound thermal therapy by patterned acoustic droplet vaporization

Oliver D. Kripfgans,^{a)} Man Zhang,^{b)} Mario L. Fabiilli, Paul L. Carson, Frederic Padilla,^{c)} Scott D. Swanson, Charles Mougenot, and J. Brian Fowlkes
Department of Radiology, University of Michigan Health System, 1301 Catherine Street,
Med Sci 1, Room 3218D, Ann Arbor, Michigan 48109-5667

Charles Mougenot

Philips Healthcare, 281 Hilmount Road, Markham, Ontario L6C 2S3, Canada

(Received 27 September 2012; revised 11 September 2013; accepted 21 October 2013)

One application of acoustic droplet vaporization (ADV), a method of converting biocompatible microdroplets into microbubbles, is to enhance locally high intensity focused ultrasound (HIFU) therapy. Two objectives are pursued here: (1) the controlled creation of a bubble trench prior to HIFU using ADV and (2) use of the trench for increasing ablation volumes, lowering acoustic powers, and decreasing therapy duration. Thermally responsive phantoms were made with perfluorocarbon emulsion. Compound lesions were formed in a laboratory setting and a clinical magnetic resonance imaging (MRI)-guided HIFU system. Linear and spiral patterned compound lesions were generated in trenches. A larger fraction of the HIFU beam is contained to increase the generation of heat. Using the laboratory system, a 90 mm linear length spiral trench was formed in 30 s with mechanical beam steering. Comparatively, the clinical HIFU system formed a 19.9 mm linear length spiral trench in approximately 1 s with electronic beam steering. Lesions were imaged optically and with MRI. A uniform thermal ablation volume of 3.25 mL was achieved in 55.4 s (4-times faster than standard clinical HIFU and 14-times larger volume versus sum of individual lesions). Single lesions showed a 400% volume increase.

© 2014 Acoustical Society of America. [<http://dx.doi.org/10.1121/1.4828832>]

PACS number(s): 43.80.Sh, 43.80.Vj, 43.35.Ei, 43.35.Wa [CCC]

Pages: 537–544

I. INTRODUCTION

High intensity focused ultrasound (HIFU) therapy is a non-invasive and non-ionizing technique wherein focused ultrasound beams are emitted from a high-powered transducer to thermally ablate the tissue volume of interest (Crouzet *et al.*, 2010). HIFU systems commonly operate in a frequency range of 0.5–5 MHz, generating high focal intensities up to 1–10 kW/cm² (Shaw and Hodnett, 2008). Such intensities can increase tissue temperature beyond 60 °C within the focal volume in seconds, resulting in irreversible protein denaturation, cell destruction, and associated coagulative necrosis (Hill and ter Haar, 1995). Two principal mechanisms, direct absorption of the transmitted pressure wave and acoustic cavitation, can cause tissue heating synergistically (Coussios and Roy, 2008). The bioeffects of focused ultrasound on tissues have been investigated for decades (Bamber and Hill, 1979; Parker, 1983; Frizzell, 1988) and the physical principles associated with HIFU are becoming better understood as HIFU becomes an accepted modality for treatment (ter Haar and Coussios, 2007).

Focused HIFU energy is sufficient to induce thermal coagulation in a small volume within seconds, and therefore blood perfusion effects acting as thermal sinks are minimal (Billard *et al.*, 1990). Although promising and effective for small tumors, attempts to expand the application of HIFU thermal ablation to larger masses have had limited success (Yamakado *et al.*, 2006; Gervais *et al.*, 2003). A major difficulty has been creating homogenous, reproducible, and uniformly shaped lesions in a time period that is clinically manageable for treating large volumes. In addition, some patients complain about local pain after HIFU therapy, which indicates normal tissue overheating, especially at sites of large acoustic impedance mismatch (Li *et al.*, 2009; Zhang *et al.*, 2010b). Therefore, methods localizing treatment and thus protecting sensitive tissues would greatly benefit HIFU and potentially yield new treatment locations.

It is well known that the thermal contribution of microbubbles can be significant. Ultrasound contrast agents (UCAs) have been investigated for the enhancement of thermal effects at the HIFU focus (e.g., Tung *et al.*, 2006). However, UCAs also move the greatest heating position from the focus by up to 2 cm for a given transducer geometry and aberrating tissues intervening the acoustic path as well as create surface lesions for concentrations greater than 0.1% (v/v), with some damage well outside the lesion (Tung *et al.*, 2006). Alternatively, acoustic droplet vaporization (ADV) is an ultrasound-based method of converting biocompatible microdroplets (Fabiilli *et al.*, 2013) into microbubbles. When exposed to acoustic pressures above the

^{a)} Author to whom correspondence should be addressed. Electronic mail: greentom@umich.edu

^{b)} Current address: Providence Hospital and Medical Center, 16001 West 9 Mile Road, Southfield, MI 48075.

^{c)} Current address: LabTau Laboratory, Inserm Unit 1032, 151 Cours Albert Thomas, 69424 Lyon Cedex 03, France.

vaporization threshold, injected perfluorocarbon microdroplets—which are similar in size to UCAs—produce microbubbles that are more than 100-fold larger in volume than the original microdroplets, resulting in a local increase in the acoustic absorption. Hence, the increased heating with ADV can be limited to the acoustic focus where pressures exceed the ADV threshold, allowing for lower source intensities and/or shorter exposure times for given therapeutic effects at the focus. Increased absorption by bubbles at the focus also reduces risk to distal tissues by decreasing the transmitted acoustic energy (Lo *et al.*, 2006).

ADV bubbles are stable for several minutes or longer and can cause vascular occlusion when lodged in a capillary or other small vessels (Kripfgans *et al.*, 2000), which is favorable for HIFU therapy. These microbubbles are highly echogenic (Zhang *et al.*, 2010a, Kripfgans, 2002), thus facilitating real-time image-guided therapy. Therefore, the ultrasonic monitoring of microbubbles created during the ADV process may offer opportunities to visualize the location and spatial extend of the HIFU process. Additionally, a dense bubble plane forms a barrier for acoustic waves and impedes wave propagation to distal tissues and can double pressure amplitudes proximal to the bubble wall (Lo *et al.*, 2006). Similar studies by Zhang *et al.* (2013) demonstrated *in vitro* that the inclusion of 0.008% (v/v) phase-shift nanoemulsion (PSNE) in phantoms significantly reduced the power required to generate 9 mm³ lesions compared to HIFU without PSNE.

This study is focused on substantially enhancing HIFU by increasing thermal lesion volume (or equivalently shortening treatment time) through precisely controlled production of ADV microbubbles from micrometer-sized droplets. This technology is expected to be applicable across a broad range of current and future uses of HIFU ablative therapy.

II. MATERIALS AND METHODS

A. Thermal phantom preparation

Thermally responsive phantoms were fabricated based on previously described methods (Takegami *et al.*, 2004). The phantoms consisted of 33% (v/v) of an aqueous acrylamide solution (30% wt/vol, Sigma-Aldrich, St. Louis, MO), 31.4% (v/v) of degassed deionized water, 35% (v/v) of egg white, 0.5% (v/v) of 10% ammonium persulfate (Sigma-Aldrich), and 0.1% (v/v) tetramethylethylenediamine (Sigma-Aldrich). Lipid droplets were made according to a previously described protocol (Fabiilli *et al.*, 2009) and stored in the refrigerator (5 °C) for up to 4 weeks. Prior to use, the droplet size distribution and number density were measured with a Coulter counter (Multisizer 3, Beckman Coulter Inc., Fullerton, CA). Approximately 99% of droplets in the emulsion were smaller than 8 μm in diameter. The mean diameter of the droplets was 2.0 ± 0.1 μm.

During phantom preparation, the gel solution was degassed before the addition of droplets to minimize spurious gas inclusions that could act as cavitation nuclei. The concentration of droplets within the phantom was 10⁵ droplets/mL, which corresponds to 0.00004% (v/v). These egg white-based phantoms were optically transparent. If HIFU increased the

temperature in a portion of the phantom to >60 °C for >5 s, the egg white protein would denature and coagulate, resulting in a permanently opaque, optically observable lesion. The acoustic attenuation of these phantoms was approximately 0.3 dB/cm at the resonance frequency of our HIFU transducer (1.44 MHz), which is also very close to the frequency of the clinical HIFU system of 1.45 MHz.

B. Laboratory HIFU lesion generation

The HIFU therapy system consisted of a high power spherical section transducer (63.5 mm diameter, f-number of 1, resonance frequency 1.44 MHz, Etalon 940501, Lebanon, IN) driven with a power amplifier (A-300, ENI Inc., Rochester, NY). Low power pulse-echo operation of the HIFU transducer allowed for focal localization in the phantom by detection of phantom boundaries by use of a micro positioning system. Also under pulse-echo guidance, a needle thermocouple (300 μm diameter, Omega, Stamford, CT) was inserted through a guide into the side of the phantom 2 mm away from the transducer focus, and a data logger (TC-08, Pico Technology, Cambridge, UK) was used to record the temperature. A function generator (3314A, Agilent, Palo Alto, CA) was gated with a secondary function generator (33120A, Agilent) to produce continuous wave (CW) signals to the amplifier for ultrasound exposures with durations of 5 s. The lateral beam width and axial depth of field at the focus [full-width at half maximum (FWHM) pressure] were 1.6 mm and 8.2 mm, respectively. The therapy transducer was calibrated using a membrane hydrophone (ST223, Sonic Industries, Hatboro, PA) in degassed water at room temperature, and the output waveforms from the hydrophone were digitized (9314L, LeCroy Corp., Chestnut Ridge, NY). A peak negative pressure of 7.4 MPa and a peak positive pressure of 17.7 MPa were measured at the focus. The maximum focal intensity was then estimated from the measured peak positive pressure (Shaw and Hodnett, 2008) by approximating the 2D acoustic beam profile with a Gaussian function and assuming linear acoustic (first order assumptions)

$$p(x, y) = p_+ e^{-(x^2/2\sigma_x^2 + y^2/2\sigma_y^2)},$$

$$P_{\text{acoustic}} = \iint_{-\infty}^{\infty} \frac{p(x, y)^2 dx dy}{Z},$$

$$I_{\text{SPTP}} = \frac{P_{\text{acoustic}}}{\pi(FWHM/2)^2},$$

where $p(x, y)$ is the focal plane pressure distribution, p_+ is the peak positive pressure amplitude of 17.7 MPa, σ_x and σ_y are related to the FWHM beam width by $\sigma_{x/y} = FWHM/2.35$, P_{acoustic} is the acoustic power to be determined, Z is the wave impedance of 1.5 MRayl, dx times dy compose an area element dA in the focal plane and I_{SPTP} is the spatial peak, temporal peak, acoustic intensity derived from the total acoustic power over the FWHM focal plane area. For the laboratory HIFU system, P_{acoustic} is computed to 304 W and I_{SPTP} to 15.1 kW/cm².

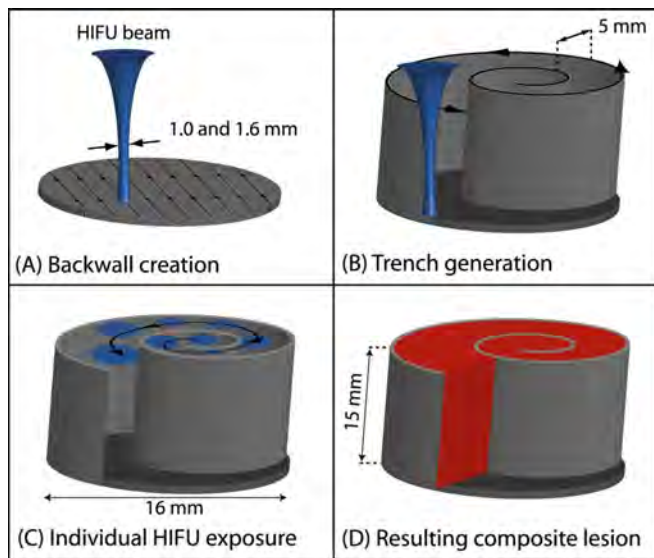


FIG. 1. (Color online) Three-dimensional schematic depiction of the acoustic trench created for HIFU. (A) First a back wall bubble layer is created by means of Acoustic Droplet Vaporization. (B) Then a bubble spiral wall is created on top of it to form a trench. (C) Inside the bubble trench, the acoustic field of a HIFU beam is used to create thermal lesions. Discrete lesions are placed along the spiral track of the trench and result in a solid lesion of the shape of a thick disk of 15 mm height (D). Trench geometries depend on the HIFU point spread function and steering capabilities of the HIFU beam. Note: Approximate aspect ratios are shown. The beam widths of the clinical and laboratory HIFU systems are 1.0 and 1.6 mm, respectively, and the trench walls are spaced approximately 5 mm. A 3.25 mL lesion can be created in 55.4 s. Actual heating required 40 s while the creation of the acoustic trench required 15.4 s.

A programmable 3-axis positioning system was used to translate the focused transducer in a spiral pattern as illustrated in Fig. 1. A short tone burst of 10 cycles at 1.44 MHz with a 0.25% duty cycle was applied to the therapy transducer to vaporize the droplets in thermal phantom blocks (5.5 cm \times 5.5 cm \times 6.5 cm), forming a bubble back wall [10 mm in thickness, Fig. 1(A)] and then a spiral sidewall [3 mm in thickness, Fig. 1(B)]. The purpose of the back and sidewalls is to reflect and largely contain the fraction of the incoming and bubble-scattered HIFU beam, confining a greatly increased fraction of the heat generation within the trench.

The formation of the spiral shaped trench was achieved within 30 s. Subsequently, compound lesions were formed by 5 s exposures of the HIFU beam inside the trench [Fig. 1(C)] separated by 5 s delays. As shown here, ultrasound was focused at discrete locations along the trench thereby generating a solid thermal lesion disk [Fig. 1(D)]. Center-to-center spacing between neighboring lesions within the trench was 5.5 mm (right column in Fig. 2). The geometry of the acoustic trenches was verified prior to HIFU exposure, using a GE Logiq 9 ultrasound scanner (GE Ultrasound, Milwaukee, WI) with a 7 L array operating at 7 MHz.

C. Lesion size estimation using visible macroscopic imaging and MRI

All lesions were imaged at 2 T with T_2 -weighted magnetic resonance imaging (MRI) with 1 mm \times 0.5 mm \times 0.25 mm

resolution, and optical macroscopic observations in sliced phantoms. In MRI, the transverse magnetization relaxation time constant, T_2 , is sensitive to slow molecular motions of water. The denatured and cross-linked proteins caused a significant decrease in the water proton mobility and thereby a decrease in the water proton T_2 (Lambelet *et al.*, 1991), which was observed as a darker region in Fig. 2. Therefore, MRI provided an alternative, independent, and direct method of measuring protein coagulation, and it was utilized to assess the uniformity of compound thermal lesions. The spin-echo MRI imaging sequence with T_2 weighting was performed within 1 h after thermal lesion production in the phantoms.

The repetition time TR, the amount of time between successive pulse sequences applied to the same slice, was 4.5 s. The echo time TE, the time between the 90° pulse and the peak of the spin echo signal and inversion recovery pulse, was 120 ms. After MRI, the lesions were sliced and dissected based on the visible color change. Lesion volumes of the laboratory HIFU system were also estimated by a fluid displacement method.

D. Lesion formation using an MRI guided clinical HIFU system

A Philips Sonalleve MRI-HIFU system utilizing a 256-element phased array was used to generate HIFU lesions. For the generation of spiral shaped trenches a first generation Sonalleve V1 system with a 120 mm HIFU transducer focal length, implemented on a 1.5 T MR scanner, was employed. A newer system, a Sonalleve V2 (3 T MR scanner, 140 mm HIFU transducer focal length), was employed for the generation of single lesions. Both Sonalleve systems, while not identical, are capable of generating either lesion shape. At the employed transmit center frequency of 1.45 MHz, a maximum electronic steering of ± 10 mm was achieved at a depth of 10 cm for spiral pattern generation analogous to that of the single element transducer. Emulsions were vaporized by use of continuous wave excitation. For the creation of the bubble back wall and bubble spiral trench using the Sonalleve V1 system, an exposure of 50 W was employed for 100 ms. For the creation and characterization of single thermal lesions, the Sonalleve V2 system was employed using exposures ranging from 30 to 200 W for 20 s at 1.45 MHz center frequency. Calibrations under free field conditions and 1 W excitation in a water tank yielded a pressure amplitude of 1.12 MPa and a point spread function FWHM intensity of 1.00 mm lateral and 7.99 mm axial. Under the assumption of linear propagation, 200 W excitation in water would result in a pressure amplitude of 15.9 MPa. Assuming that 66% of the beam intersects the FWHM of the focus as a planar wave traveling in water with 1.5 MRayl impedance, this pressure corresponds to 12.7 kW/cm² (16.2 MPa).

Lesion volumes were measured by MRI and computed as all volumetric pixels with T_2 values deviating from background as described by Zhang *et al.* (2011). Lesion volume increases due to the presence of perfluorocarbon emulsions in the phantoms during HIFU were quantified as the ratios of

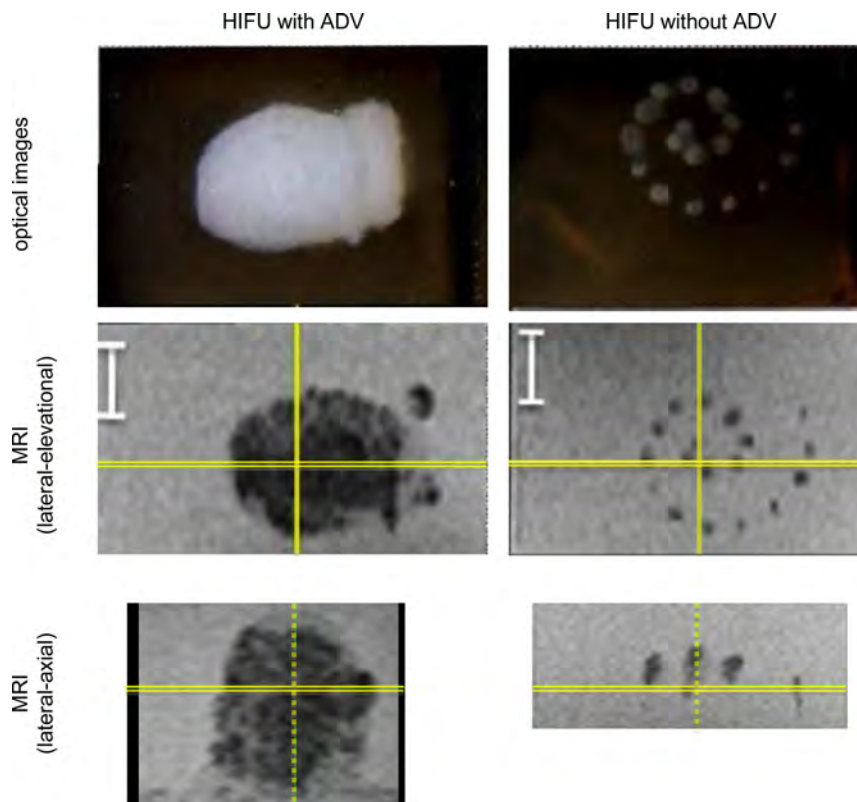


FIG. 2. (Color online) Optical (top row) and T₂-weighted MR images (bottom two rows) of lesions (i.e., denatured protein) generated within thermal phantoms using the laboratory HIFU system. The left and right columns depict lesions generated with and without ADV-enhancement (see Fig. 1), respectively. The scale bar is 1 cm. The solid, double and dashed lines superimposed to the middle and bottom row MRI scans indicate where the lateral-elevational and the lateral-axial images intersect.

lesion volume with and without emulsions present. Lesion sizes were quantified as a function of applied acoustic power ranging from 30 to 200 Watts and *in situ* temperature monitoring with a therapeutic endpoint of 75 °C (see Fig. 3). Statistically significant differences between lesions sizes (i.e., with and without ADV) were determined using a Student's *t*-test. A significance level of 0.05 was used for all comparisons.

In Fig. 3(A), real-time heating is assessed and then displayed via a pseudo color map whose scale is shown on the right colorbar. The temperature map is overlaid on the continuously updated magnitude image resulting from the gradient echo sequence that is used to measure temperature. Since

the thermal map scan sequence is not optimized for good contrast, but rather for fast acquisition and good signal to noise at the center, the image appears gray and is subject to some zebra artifacts (Stadler *et al.*, 2007) at the edge of image. In this sequence, ADV was performed at an output of 100 W. A temperature of 83 °C was reached in part of the lesion. Conversely, Fig. 3(B) displays the real-time temperature mapping employing a static T₂ weighted spin echo image sequence acquired before the heating sequence. The T₂ weighted spin sequence is slow but provides better contrast without artifact or image distortion, which allows discrimination of the various layers in the phantom and its surroundings more clearly.

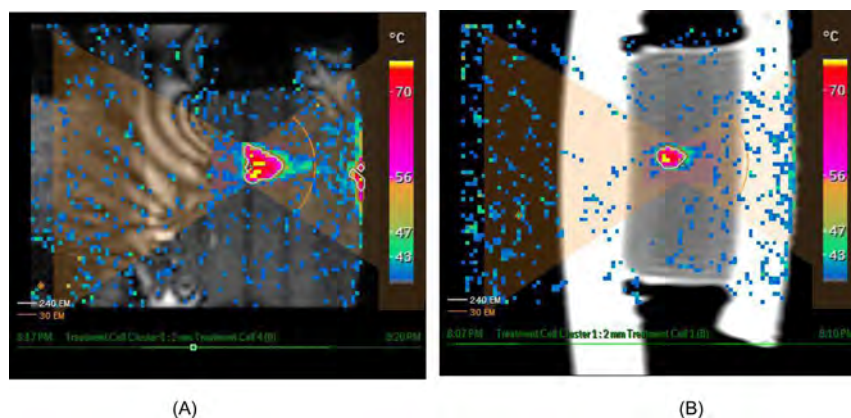


FIG. 3. (Color online) MRI-guided temperature readout during HIFU exposure. (A) A temperature map, scale bar on the right side, is overlaid on the magnitude image of the MRI gradient echo sequence. The gradient echo sequence is optimized for fast acquisition and signal-to-noise at the center. (B) Conversely, using a T₂ weighted spin sequence once, a static background image is generated and placed behind the continuously updated heating color map, therefore providing better contrast for distinguishing phantom details and other important structures. Note: The HIFU beam enters from the left into the phantom and the spatial extent of the beam is illustrated by the two shaded opposing triangles.

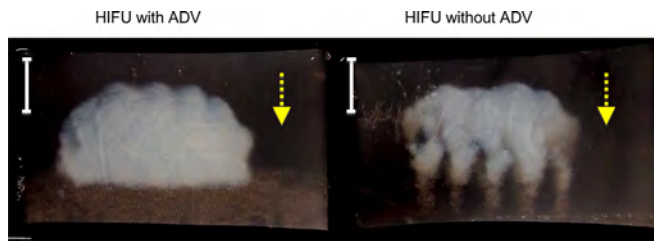


FIG. 4. (Color online) Optical images (side view) of linear compound lesions (white) in doped phantoms, generated with the laboratory system, with (left) and without (right) a bubble wall. The bubble back wall is visible below the lesion on the left. Note that the tadpole shape characteristic of bubble-enhanced HIFU lesions is not evident with the bubble wall. A thermal ablation volume of 15 mL was achieved in 4 min with ADV and the acoustic trench. The scale bar is 1 cm. The dashed arrowhead line shows propagation direction of the HIFU.

III. RESULTS AND DISCUSSION

A. Laboratory HIFU lesion generation

Compound lesions in a spiral pattern were formed in phantoms with and without droplets, in the following referred to as “doped phantom” and “control phantom,” respectively. Initial results, shown in Fig. 2, were similar for both optical macroscopic and T_2 -weighted MR images. In MR images, a high contrast between the mean gray levels inside the lesions and the surrounding background was observed, which showed a difference of at least nine standard deviations. The coefficients of variance were found to be similar in the lesion and in the background medium (i.e., the standard deviations did not exceed 5% of the mean value). Therefore, a simple amplitude thresholding was applied in each section to discriminate pixels included in the lesions from pixels of the background, with a threshold set to the mid-value between the mean gray level values in the lesion and in the background.

For lesions generated in a spiral pattern (Fig. 2), a 2.5-fold increase in the axial dimension of the lesion was obtained with the acoustic trench. Figure 4 shows optical images of linear compound lesions. Given the homogeneously complete filling of the treatment space, there is a considerably larger volume that is treated when using the ADV enhancement and acoustic trench approach. For instance, here a uniform thermal ablation volume of 15 mL was

achieved in 4 min with ADV and the acoustic trench. A common term in the HIFU literature is the time spent on a lesion of a given volume. Here 4 min for a 15 mL lesion yields 16 s/mL.

In both optical and MR images of the HIFU lesion in the presence of ADV bubbles, the back bubble wall was visible below the lesion. The tadpole shape characteristic of bubble-enhanced HIFU lesions was not evident with the bubble wall in place (Fig. 4). As seen in Fig. 4, the thermal lesion, indicated by the opaque denatured egg-white, ended abruptly and uniformly across the back wall. The layer of this exposure plane (i.e., proximal to the transducer) can then be the back wall for the next layer. It is expected that ADV occurs during lesion formation as both ADV and lesion formation were executed with the same pressure amplitudes though longer exposure times were required for lesion formation. The function of the acoustic trench sidewalls is to reflect the lateral and elevational beam components hereby resulting in a homogeneous lesion versus the tadpole shape.

B. Lesion formation results using a clinical HIFU system

Rapid repetition of electronically steered therapy pulses (40 pulses per second, 50 W) in the clinical HIFU system allowed for the generation of nearly homogeneous composite lesions at 17.0 s/mL or better (Fig. 5). The volume of compound lesion (3.24 mL) is 14-times larger than the sum total single volumes ($8 \times 28.4 \mu\text{L} = 227 \mu\text{L}$). The time to create a spiral compound lesion is 55 s (i.e., 17.0 s/mL), versus 40 s (i.e., 176 s/mL) to create eight individual lesions with no back wall and no spiral trench. Thus, a 1400% increase in lesion volume was achieved with only a 37% increase in treatment time.

Consistent with earlier results on the laboratory system (see also Zhang *et al.*, 2011), for acoustic power levels ranging from 30 to 200 W, lesion volumes of doped phantoms increased compared to lesion volumes in control phantoms (see Fig. 6). Lesion temperature was recorded in real-time and used as the therapy end-point while insonifying at the employed acoustic power. Lesion size was measured over a range of power levels and axial as well as lateral lesion dimensions. The minimum power level at which lesions

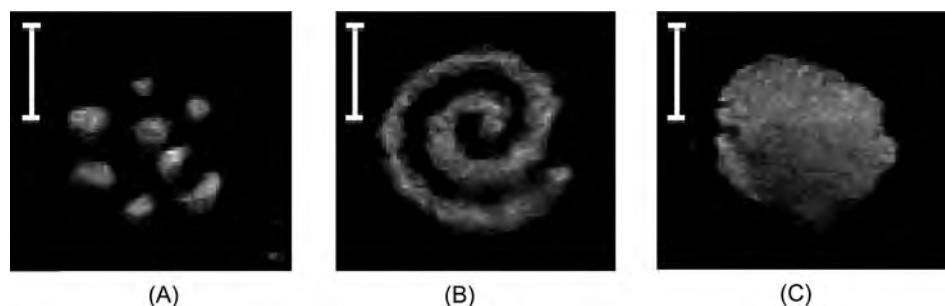


FIG. 5. B-mode images of single and compound lesions from the clinical HIFU system are shown in panels (A), (B), and (C), respectively. (A) Eight individual bubble clouds and HIFU from ADV produced with a 5 s per cloud sweep speed and illustrate the extent of single lesions. (B) A spiral shaped trench wall is created within 4 s by rapid succession of individual acoustic electronically steered pulses for ADV. Forty-four individual beam positions were targeted with 100 ms each to form the shown spiral. (C) In a second step, as schematically illustrated in Fig. 1, the formed acoustic trench was filled-in by eight additional individually positioned HIFU beams (50 W, 5 s each), which then created the solid lesion that is shown. A backside wall (not shown) was created before the spiral with 110 beams in 11 s. The total lesion (3.25 mL) creation time including bubble clouds was 55 s (see Fig. 1) or 17.0 s/mL.

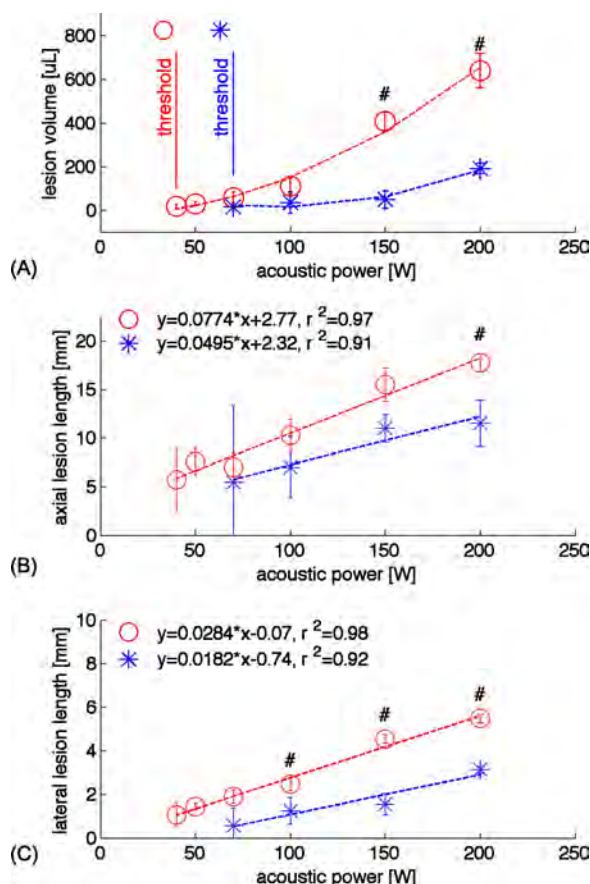


FIG. 6. (Color online) (A) Lesion sizes were estimated using T_2 -weighted MR imaging. Doped phantoms (open circles) showed larger lesion volumes than control phantoms (stars). To reach an average lesion volume of 0.105 mL in the control phantom, the acoustic power must be more than doubled (213%). At 150 W acoustic power the lesion volume ratio of doped versus control exceeds 8-times. Vertical lines indicate the thresholds, below which lesions are not observed. (B) and (C) Axial and lateral lesion diameters were measured. Lesion volumes in doped phantoms showed a greater functional gradient with applied acoustic power compared to control phantoms. Data are shown as the mean \pm standard deviation for $n = 4$. “#” indicate $p < 0.05$ versus control phantoms.

were observed was 40 W (doped phantom), which corresponded to a lesion volume of $17 \pm 11 \mu\text{L}$. Figure 6 shows that at 150 W acoustic power, doped phantoms yielded eight-times larger lesions for the same acoustic power than control phantoms. To reach an average lesion volume of 0.105 mL in the control phantom, the acoustic power must be more than doubled (213%) compared to the power used in the doped phantom. Doped lesions with volumes statistically different from controls are marked with a “#” symbol in Fig. 6(A). Regression analyses [Figs. 6(B) and 6(C)] show that both the lateral and axial lesion lengths increase with $\sim 56.0\%$ greater slope when comparing doped to control phantoms. A constant offset of the fitting function over the tested acoustic power possibly indicates the larger depth of field compared to the lateral beam diameter.

As shown in Fig. 7, the lesion shapes within control and doped phantoms differed, with lesions within control phantoms showing higher symmetry along the axial direction. Doped phantoms exhibited lesions that progressed toward the sound source and were cone shaped, except for a tail distal to the triangle. At each axial position of a lesion the

lateral-elevational cross-sectional area A was measured. Then an effective radius was calculated as $r_{\text{eff}} = \sqrt{A/\pi}$. Line plots of r_{eff} are shown as a function of axial position to illustrate the three-dimensional character of the lesions.

The acceleration of HIFU procedures by use of administered or induced gas bodies has been investigated by numerous research groups. Peng *et al.* (2012) compared ultrasound-guided HIFU treatment for uterine fibroids to treatment enhanced by SonoVue, administered 10 min before HIFU as a bolus of 2.0 mL normal saline with 10.0 mg SonoVue via the hand vein. For fibroids smaller than 4 cm in diameter, average sonication times decreased from 69 s/mL (HIFU only) to 34 s/mL (HIFU + SonoVue), meanwhile the range decreased as well 2–619 s/mL versus 15–334 s/mL, but is not significantly different at $p = 0.354$. For ADV accelerated HIFU, in comparison, single lesion formation was achieved in the clinical HIFU system in less than 20 s, resulting in a 0.67 mL volume, hence allowing for approximately 30 s/mL lesioning rates. For lesions based on spiral trenches, the rate improved to 17.0 s/mL.

During image-guided ultrasound therapy, the rate of massive gray scale changes during lesion formation was 50.0% (HIFU only) versus 77.8% (HIFU + SonoVue) (Peng *et al.*, 2012). Chung *et al.* (2012) reported that the volume of coagulative necrosis was significantly larger for contrast-assisted HIFU in comparison to HIFU alone. Here the volume increased from 0.83 mL to 1.75 mL ($p < 0.05$). Simultaneously, tissue ablation times significantly decreased from 12.1 s to 8.6 s ($p < 0.05$). Illing *et al.* (2005) stated that observed adverse events were localized to the area of treatment. Following HIFU treatment, skin toxicity occurred in 27% of the cases (8/30). These were not clinically relevant (except for one case) and resolved spontaneously. Ablation at large depth (e.g., kidney tumors) may be more difficult and less reliable than at more superficial depths (e.g., liver tumors). Illing *et al.* speculated that this decreased reliability “may be due to the greater depth of renal tumor[s] and the presence of a perinephric fat layer, both of which attenuate the ultrasonic beam.”

To treat rapidly enough for efficient use of expensive facilities and staff as well as reasonable duration of anesthesia, it is essential to enhance heating without damaging the skin and other overlying tissues. For example, a single uterine fibroid with a volume of 17 mL requires approximately 20 min of treatment time using current standard HIFU. Using ADV enhanced trenches, this time would decrease to 5 min. The treatment time for a 6 cm diameter hepatocellular adenoma, which currently requires 2 h, would be reduced to 30 min.

ADV shows the potential to provide local control of heat deposition while minimizing tissue damage caused by microbubbles in the path of therapeutic ultrasound beams, as is the case in use of UCAs. In this study, an appropriate bubble density was achieved consistent with therapeutic ultrasound while providing uniform ablation. The required droplet concentration was comparable to diagnostic UCA use. While the emulsion core material, dodecafluoropentane (C_5F_{12}), is an inert fluid with high biocompatibility, *in vivo* administration of large quantities may cause bioeffects (Zhang *et al.*, 2011). In this paper, 10^5 droplets/mL were used to enhance HIFU

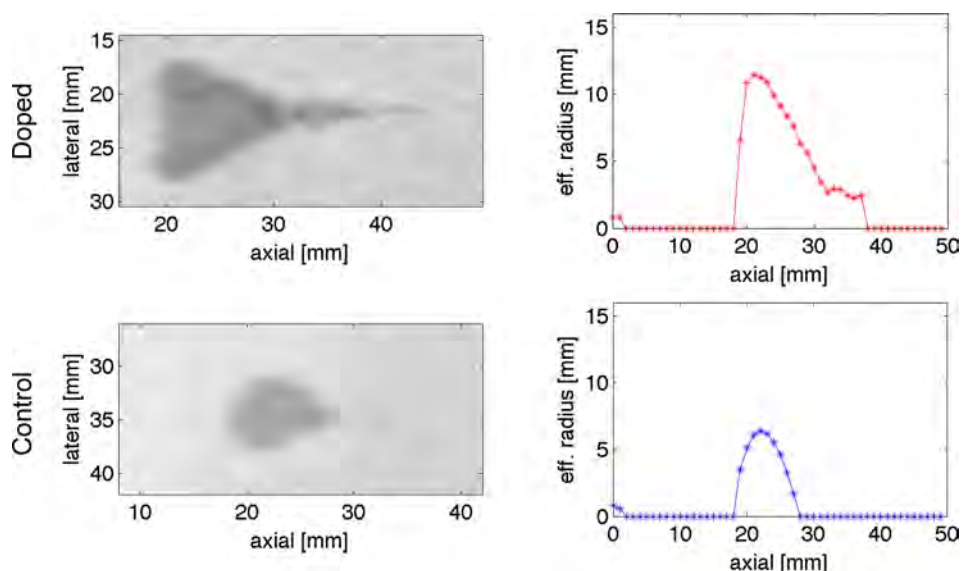


FIG. 7. (Color online) (Left) MRI images showing coronal cross-sections of generated HIFU lesions at 200 W acoustic power and 20 s exposure for doped and control phantoms. The propagation direction of the HIFU was from left to right. Achieved lesion volumes and volumetric creation speeds were 0.654 mL and 30.6 s/mL as well as 0.185 mL and 108 s/mL for doped (top) and control (bottom) phantoms, respectively. (Right) For each lesion the lateral-elevational cross-section was fit to a circle. The radius of the fitted circle is plotted as a function of axial position through the lesion. Lesion geometry asymmetries between doped and control phantoms can be seen.

lesions. In a highly perfused organ such as liver, with an average fractional blood volume of 31% (Schwickert *et al.*, 2005), 3.23×10^5 droplets/mL of blood are required for HIFU lesions in a 70 kg human with 5 L blood volume. Systemically, this yields 2.3×10^7 droplets/kg, which is 282-times lower in concentration than a recent biodistribution study where a similar emulsion was safely tolerated at 6.5×10^9 droplets/kg (Fabiilli *et al.*, 2013).

Our phantom experiments demonstrated no heating effects such as protein denaturation in the pre-focal or post-focal ultrasound propagation pathway (see Fig. 3). In addition, use of an ADV-bubble back wall limits distal ultrasound propagation, thus limiting damage beyond the wall. It is possible to create these distal barriers prior to treatment as an additional layer of protection for sensitive tissues such as nerves in clinical implementations. It is therefore hypothesized that, building upon previously produced lesions with ADV bubbles should allow for the reduction of the transmitted acoustic energy, which can be advantageous in sensitive tissue regions. These bubble walls can be created using low duty cycle, microsecond pulses that will not generate thermal lesions. Further investigations of the requisite bubble wall characteristics and the level of protection afforded by the wall are warranted as are studies of the optimal location of the ultrasound beam focus for heating in front of the barrier wall. Our results also indicated that for the treatment of a large volume, the ADV-enhanced HIFU would require fewer targeting sites to create a compound lesion throughout a predetermined volume, because the size of the individual lesions was increased. Lesion size diminishes with decreasing acoustic power, as seen when treating tissues at large depth. Compensatory increase in acoustic power is limited due to its consequential damage of overlying tissues. However, an increase in the maximum depth of treatment is achievable by means of ADV enhanced HIFU as the required acoustic power is on average lowered by 47% for the same depth lesion of 0.1 mL volume, when compared to non-ADV HIFU (Fig. 6). Therefore, currently untreatable regions due to depth or restricted aperture should be realizable by the use of ADV.

Another parameter warranting further study is the optimum size for the emulsion. In this paper, a micron-sized emulsion, similar in size to UCA, was used. A previous *in vitro* study (Zhang *et al.*, 2013) utilized a 50-fold higher concentration of submicron-sized emulsion, which could ultimately accumulate within a tumor via extravasation through leaky vasculature. This type of passive targeting could further enhance localized heating effects, though the relationship between emulsion size and the concentration required for enhanced heating is not fully elucidated.

IV. SUMMARY AND CONCLUSION

ADV greatly enhanced HIFU therapy by increasing the efficiency of focal energy deposition. Large, compound lesions can be generated at a rate of 17 s/mL of lesion volume. Uniform stacking of spiral lesions occurred without the distal gaps characteristic of lesions using bubble enhancement, which allows for efficient stacking of compound lesions. The thermal lesion had a sharp back wall margin, allowing precise protection of tissue structures distal to the targeted region. Perfluorocarbon emulsions demonstrate great potential for enhancing clinically relevant HIFU performance, with four-times faster treatment times as well as improved lesion homogeneity. This initial phantom study serves as an appropriate test of our methods and also provides preliminary indications for *in vivo* animal study and clinical trials. Efficient lesion formation with real-time imaging feedback at droplet concentrations less than 1% of tested safety limits supports feasibility for high biocompatibility of this mechanism to accelerate thermal therapy. This technology may be applicable across a broad range of HIFU applications.

ACKNOWLEDGMENTS

The study was supported in part by NIH Grant No. 5R01EB000281, DOD/BCRP Grant No. BC095397P1 and University of Michigan (UM)–Shanghai Jiao Tong University (SJTU) Collaboration on Biomedical Technologies grant award.

- Bamber, J. C., and Hill, C. R. (1979). "Ultrasonic attenuation and propagation speed in mammalian tissues as a function of temperature," *Ultrasound Med. Biol.* **5**, 149–157.
- Billard, B. E., Hynynen, K., and Roemer, R. B. (1990). "Effects of physical parameters on high temperature ultrasound hyperthermia," *Ultrasound Med. Biol.* **16**(4), 409–420.
- Chung, D. J., Cho, S. H., Lee, J. M., and Hahn, S. T. (2012). "Effect of microbubble contrast agent during high intensity focused ultrasound ablation on rabbit liver in vivo," *Eur. J. Radiol.* **81**(4), e519–e523.
- Coussios, C., and Roy, R. (2008). "Applications of acoustics and cavitation to noninvasive therapy and drug delivery," *Annu. Rev. Fluid. Mech.* **40**, 395–420.
- Crouzet, S., Rebillard, X., Chevallier, D., Rischmann, P., Pasticier, G., Garcia, G., Rouviere, O., Chapelon, J. Y., and Gelet, A. (2010). "Multicentric oncologic outcomes of high-intensity focused ultrasound for localized prostate cancer in 803 patients," *Eur. Urol.* **58**, 559–566.
- Fabiilli, M. L., Haworth, K. J., Nasir, F., Kripfgans, O. D., Carson, P. L., and Fowlkes, J. B. (2009). "The role of inertial cavitation in acoustic droplet vaporization," *IEEE Trans. Ultrason. Ferroelectr. Freq. Control.* **56**, 1006–1017.
- Fabiilli, M. L., Piert, M. R., Koeppe, R. A., Sherman, P. S., Quesada, C. A., and Kripfgans, O. D. (2013). "Assessment of the biodistribution of an [18F]FDG-loaded perfluorocarbon double emulsion using dynamic micro-PET in rats," *Contrast Media Mol. Imaging* **8**(4), 366–374.
- Frizzell, L. A. (1988). "Threshold dosages for damage to mammalian liver by high-intensity focused ultrasound," *IEEE Trans Ultrason Ferroelectr Freq Control.* **35**, 578–581.
- Gervais, D., McGovern, F., Arellano, R., McDougal, W. S., and Mueller, P. (2003). "Renal cell carcinoma: Clinical experience and technical success with radio-frequency ablation of 42 tumors," *Radiology* **226**, 417–424.
- Hill, C. R., and ter Haar, G. R. (1995). "Review article: High intensity focused ultrasound-potential for cancer treatment," *Br. J. Radiol.* **68**(816), 1296–1303.
- Illing, R. O., Kennedy, J. E., Wu, F., ter Haar, G. R., Protheroe, A. S., Friend, P. J., Gleeson, F. V., Cranston, D. W., Phillips, R. R., and Middleton, M. R. (2005). "The safety and feasibility of extracorporeal high-intensity focused ultrasound (HIFU) for the treatment of liver and kidney tumours in a Western population," *Br. J. Cancer* **93**, 890–895.
- Kripfgans, O. D. (2002). "Acoustic droplet vaporization for diagnostic and therapeutic applications," Ph.D. thesis, University of Michigan, Ann Arbor, Michigan.
- Kripfgans, O. D., Fowlkes, J. B., Miller, D. L., Eldevik, O. P., and Carson, P. L. (2000). "Acoustic droplet vaporization for therapeutic and diagnostic applications," *Ultrasound Med. Biol.* **26**(7), 1177–1189.
- Lambelet, P., Ducret, F., Leuba, J., and Geoffroy, M. (1991). "Low-field nuclear magnetic resonance relaxation study of the thermal denaturation of transferrins," *J. Agric. Food Chem.* **39**, 287–292.
- Li, J.-J., Gu, M.-F., Luo, G.-Y., Liu, L.-Z., Zhang, R., and Xu, G.-L. (2009). "Complications of high intensity focused ultrasound for patients with hepatocellular carcinoma," *Technol. Cancer Res. Treat.* **8**(3), 217–224.
- Lo, A. H., Kripfgans, O. D., Carson, P. L., and Fowlkes, J. B. (2006). "Spatial control of gas bubbles and their effects on acoustic fields," *Ultrasound Med. Biol.* **32**(1), 95–106.
- Parker, K. J. (1983). "Ultrasonic attenuation and absorption in liver tissue," *Ultrasound Med. Biol.* **9**(4), 363–369.
- Peng, S., Xiong, Y., Lia, K., He, M., Deng, Y., Li Chen, Zou, M., Chen, W., Wang, Z., He, J., and Zhang, L. (2012). "Clinical utility of a microbubble-enhancing contrast ('SonoVue') in treatment of uterine fibroids with high intensity focused ultrasound: A retrospective study," *Eur. J. Radiol.* **81**(12), 3832–3838.
- Schwickert, H. C., Roberts, T. P. L., Shames, D. M., van Dijke, C. F., Disston, A., Miihler, A., Mann, J. S., and Brasch, R. C. (2005). "Quantification of liver blood volume: Comparison of ultra short TI inversion recovery echo planar imaging (ULSTIR-EPI), with dynamic 3D-gradient recalled echo imaging," *Magn Reson Med.* **34**(6), 845–852.
- Shaw, A., and Hodnett M. (2008). "Calibration and measurement issues for therapeutic ultrasound," *Ultrasonics* **48**, 234–252.
- Stadler, A., Schima, W., Ba-Ssalamah, A., Kettenbach, J., and Eisenhuber, E. (2007). "Artifacts in body MR imaging: Their appearance and how to eliminate them," *Eur Radiol.* **17**, 1242–1255.
- Takegami, K., Kaneko, Y., Watanabe, T., Maruyama, T., Matsumoto, Y., and Nagawa, H. (2004). "Polyacrylamide gel containing egg white as new model for irradiation experiments using focused ultrasound," *Ultrasound Med. Biol.* **30**, 1419–1422.
- ter Haar, G., and Coussios, C. (2007). "High intensity focused ultrasound: Physical principles and devices," *Int. J. Hyperthermia* **23**(2), 89–104.
- Tung, Y., Liu, H., Wu, C., Ju, K., Chen, W., and Lin W. (2006). "Contrast-agent-enhanced ultrasound thermal ablation," *Ultrasound Med. Biol.* **32**, 1103–1110.
- Yamakado, K., Nakatsuka, A., Kobayashi, S., Akeboshi, M., Takaki, H., Kariya, Z., Kinbara, H., Arima, K., Yanagawa, M., Hori, Y., Kato, H., Sugimura, Y., and Takeda, K. (2006). "Radiofrequency ablation combined with renal arterial embolization for the treatment of unresectable renal cell carcinoma larger than 3.5 cm: Initial experience," *Cardio. Vascular Inter. Radiology* **29**(3), 389–394.
- Zhang, L., Chen, W.-Z., Liu, Y.-J., Hu, X., Zhou, K., Chen, L., Peng, S., Zhu, H., Zou, H.-L., Bai, J., and Wang, Z.-B. (2010b). "Feasibility of magnetic resonance imaging-guided high intensity focused ultrasound therapy for ablating uterine fibroids in patients with bowel lies anterior to uterus," *Eur. J. Radiol.* **73**(2), 396–403.
- Zhang, M., Fabiilli, M. L., Fowlkes, J. B., Padilla, F., Kripfgans, O. D., Swanson, D. S., and Carson, P. L. (2011). "Acoustic droplet vaporization for enhancement of thermal ablation by high intensity focused ultrasound," *Acad. Rad.* **18**(9), 1123–1132.
- Zhang, M., Fabiilli, M. L., Haworth, K. J., Fowlkes, J. B., Kripfgans, O. D., Roberts, W. W., Ives, K. A., and Carson, P. L. (2010a). "Initial investigation of acoustic droplet vaporization for occlusion in canine kidney," *Ultrasound Med. Biol.* **36**(10), 1691–1703.
- Zhang, P., Kopechek, J. A., and Porter, T. M. (2013). "The impact of vaporized nanoemulsions on ultrasound-mediated ablation," *J. Therapeutic Ultrasound* **1**(2), 1–13.

A Preclinical System Prototype for Focused Microwave Thermal Therapy of the Breast

John Stang*, *Member, IEEE*, Mark Haynes, *Member, IEEE*, Paul Carson, *Senior Member, IEEE*, and Mahta Moghaddam, *Fellow, IEEE*

Abstract—A preclinical prototype of a transcutaneous thermal therapy system has been developed for the targeted treatment of breast cancer cells using focused microwaves as an adjuvant to radiation, chemotherapy, and high-intensity-focused ultrasound. The prototype system employs a 2-D array of tapered microstrip patch antennas operating at 915 MHz to focus continuous-wave microwave energy transcutaneously into the pendent breast suspended in a coupling medium. Prior imaging studies are used to ascertain the material properties of the breast tissue, and these data are incorporated into a multiphysics model. Time-reversal techniques are employed to find a solution (relative amplitudes and phase) for focusing at a given location. Modeling tests of this time-reversal focusing method have been performed, which demonstrate good targeting accuracy within heterogeneous breast tissue. Experimental results using the laboratory prototype to perform focused heating in tissue-mimicking gelatin phantoms have demonstrated 1.5-cm-diameter focal spot sizes and differential heating at the desired focus sufficient to achieve an antitumor effect confined to the target region.

Index Terms—Hyperthermia, microstrip patch antennas, microwave imaging, microwave therapy, time reversal.

I. INTRODUCTION

THERMAL therapies—particularly the use of thermal ablation (including microwave, RF, cryoablation, and high-intensity-focused ultrasound [1]), hyperthermia, and heat activated drug delivery in the treatment of cancer—have been the focus of increasing laboratory and clinical research. In the various ablation methods, either significantly elevated temperatures (typically above 50 °C) generated by electromagnetic waves or ultrasound, or freezing temperatures generated by cryogens are used to cause very rapid and localized tissue destruction. In the case of hyperthermia, moderately elevated temperatures (typically between 40 °C and 45 °C) have been shown to achieve

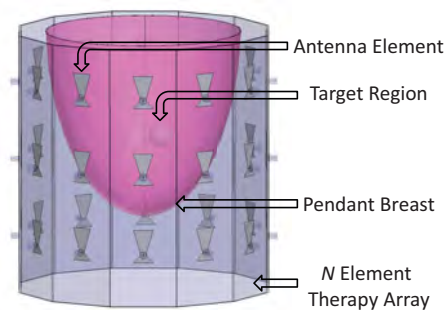


Fig. 1. Focused microwave therapy of the breast: General approach.

cytotoxic effects that render cancer cells more vulnerable to radiotherapy [2] and chemotherapy [3], as well as inducing both apoptotic and necrotic cell death given a sufficient thermal dose [4]–[6].

Motivated by this knowledge, researchers have developed microwave systems capable of inducing localized hyperthermia as an adjuvant cancer treatment modality. Laboratory and clinical studies of a system using a two-element adaptive phased array and an invasive electric-field probe to focus within a compressed breast have been reported by Dooley *et al.* [7] and Vargas *et al.* [8]. In addition, Stauffer *et al.* [9], [10] and Dewhurst *et al.* [11] have demonstrated MR-guided phased arrays for the treatment of locally advanced breast cancer, chest wall recurrence, and osteosarcomas. Several groups have also begun clinical testing of temperature-triggered drug delivery using low temperature-sensitive liposomes activated with hyperthermia [12] and RF ablation [13]. A summary of the methods and recent progress in heat-activated drug delivery can be found in [14].

With these potential applications in mind, a preclinical prototype of a noninvasive thermal therapy system has been developed for the targeted treatment of breast cancer cells using focused microwaves. In this system, an array of antennas operating at 915 MHz is used to focus continuous-wave microwave energy transcutaneously into the pendent breast suspended in a coupling medium (shown in Fig. 1). Prior imaging studies are used to ascertain the material properties of the breast tissue, and these data are incorporated into a multiphysics model. Time-reversal techniques (described in Section II-A) are then employed to find a solution (relative amplitudes and phase) for focusing at a given location, resulting in maximal thermal dose at the tumor location. Using this system, focal spot sizes in the array plane of approximately 1.5 cm in diameter have been achieved (discussed in Section III-B), and significant differential heating in the target region has been observed in focused

Manuscript received December 19, 2011; revised February 16, 2012; accepted April 10, 2012. Date of publication May 15, 2012; date of current version August 16, 2012. This work was supported in part by the Department of Defense peer-reviewed Breast Cancer Research Program (W81XWH-10-1-0514; BC095397) and by the National Institutes of Health (T32 EB005172). Asterisk indicates corresponding author.

*J. Stang is with the Basic Radiological Sciences Ultrasound Group, Applied Physics Program, and the Radiation Laboratory, Department of Electrical Engineering and Computer Science, The University of Michigan, Ann Arbor, MI 48109-2122 USA (e-mail: john.stang@gmail.com).

M. Haynes, P. Carson, and M. Moghaddam are with the Basic Radiological Sciences Ultrasound Group, Applied Physics Program, and the Radiation Laboratory, Department of Electrical Engineering and Computer Science, The University of Michigan, Ann Arbor, MI 48109-2122 USA (e-mail: mshaynes@umich.edu; pcarson@umich.edu; mmoghadd@eecs.umich.edu).

Color versions of one or more of the figures in this paper are available online at <http://ieeexplore.ieee.org>.

Digital Object Identifier 10.1109/TBME.2012.2199492

heating tests within tissue-mimicking gelatin phantoms (details in Section III-C).

Based on these results, this system has the potential to offer improved targeting and delivery of focused heating over current microwave thermal therapy systems, without the need for invasive probes. Upon completion of an optimized clinical version, this system will have the potential to be used in neoadjuvant thermal treatment for presurgical tumor reduction, noninvasive tumor ablation, locally enhanced drug delivery, and in postoperative adjuvant therapy to reduce local recurrence.

II. METHODS

Development of the preclinical microwave thermal therapy prototype system was completed in a series of stages. First, an initial 2-D antenna array was designed, and a full-wave forward model of the microwave therapy array was created. Following that, modeling tests of the time-reversal focusing method were performed to ensure good targeting accuracy within heterogeneous breast tissue. Next, the focusing ability of the system was characterized by measuring the microwave power distribution within the therapy chamber using a coaxial probe. Finally, tissue-mimicking gelatin phantoms were developed and experiments were performed to test differential heating capability at the desired focus, along with the system's ability to achieve a tumoricidal thermal dose confined to the target region.

A. Image-Based Time-Reversal Focusing

An early study by Surowiec and Bicher [15] proposed a three-element-focused hyperthermia system that identified the need to account for the various effects of source and array geometry on focusing. Since that study, researchers have developed various methods of computing the relative magnitude and phase parameters necessary to focus microwave energy at the target. In the clinical system reported by the authors in [16] and [17], an invasive electric-field probe placed within the compressed breast is used to focus a two-element adaptive phased array. Recent theoretical studies have also reported less invasive methods including the use of a deformable mirror method [18] and transmit beamforming methods [19]. Finally, there are time-reversal techniques which are rooted in theory previously developed for ultrasound focusing [20], such as those discussed in [21] and [22].

In the patient-specific variant of the time-reversal method employed here, the predicted microwave tissue properties from a prior imaging study (e.g., ultrasound, MRI, CT, or possibly microwave imaging) are incorporated into a full-wave forward model of the microwave therapy array [see Fig. 2(a)]. A synthetic dipole point source polarized along the axis of the cylindrical cavity is then excited at the target location within the breast [as shown in the field distribution on the left in Fig. 2(b)]. The relative phase of the electric field at each antenna feed location after traveling from the point source excitation through the intervening breast tissue and coupling fluid is computed and stored. The complex phase information is then conjugated (time-reversed) to produce the phase delays needed to electronically steer the focus of the microwave antenna array back to the inclusion location [as shown in the field distribution on the right in Fig. 2(b)].

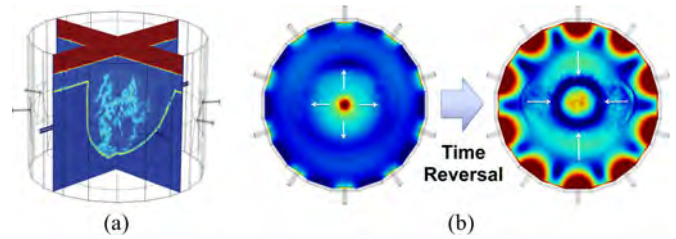


Fig. 2. (a) Sample imported MR image of fatty breast. (b) Patient-specific time-reversal focusing using imported MR image. (Left) Outgoing field distribution due to synthetic dipole placed at the center of the array. (Right) Incoming field distribution focused using time-reversed phase data.

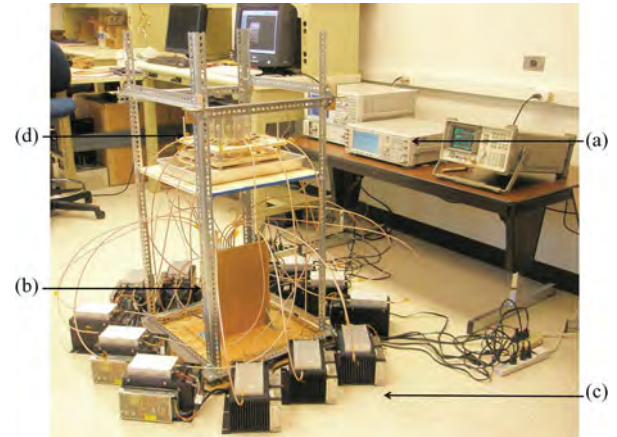


Fig. 3. Two-dimensional microwave thermal therapy system prototype. (a) Signal generator, (b) 12-channel electronic phase control, (c) 10-W per channel amplifiers (120 W total), and (d) 12-element therapy array.

A table of phase delays needed to focus within the therapy chamber can then be generated by repeating this procedure for the set of desired focal locations. In the experiments that follow, this was done on a 1.5-cm uniform grid of 49 possible focal states.

B. System Design

As shown in Fig. 3, the prototype microwave therapy system consists of a signal generator, a 12-channel power divider and electronically controlled phase shifter network, 12 microwave amplifiers providing 10 W of power per channel, and a 15-cm-diameter cylindrical cavity containing a 12-element antenna array. The signal generator provides a low-power 915-MHz continuous microwave source, which is first equally divided to each channel using the Minicircuits power divider (ZN12PD-252-S+). Each channel is then simultaneously phase-delayed using a series of two electronically controlled phase shifters (Minicircuits JSPH-1000) by an amount determined with the time-reversal focusing method discussed previously. Each of the appropriately delayed signals are then amplified with a 10-W Minicircuits broadband amplifier (ZHL-10W-2G+) and transmitted into the therapy chamber using a microstrip patch antenna designed to operate with maximum efficiency at 915 MHz. The loss through the power divider/phase shifter network was measured to be 14.5 dB and is compensated for using the signal generator. The power at the output of each amplifier was measured to be 40.7 dBm (11.75 W) using a spectrum analyzer.



Fig. 4. (a) Initial temperature measurements with digital probe thermometers in 50/50 oil-in-water gelatin phantom with 30/70 oil-in-water cylindrical inclusion. (b) Thermistor array above homogeneous 50/50 oil-in-water gelatin phantom in 60/40 matching fluid.

1) *Microstrip Antenna Array*: In microwave thermal therapy, as in near-field microwave imaging, antennas must be designed to radiate either directly into tissue, or into a matching fluid medium designed to mimic the dielectric properties of the tissue. Also, mutual impedance effects can negatively impact antenna performance in a variety of ways (shift resonant frequency, alter radiation pattern, reduce matching performance). Furthermore, these effects can influence each antenna in an array differently, depending on the geometry of the antenna and the array. Since it is not feasible to account for all of these effects analytically, the general strategy was to use an iterative combination of analytical methods and computer simulation in order to design the proof of concept array. First, a standard model of a rectangular patch antenna was used to make an initial design intended to resonate at 915 MHz (ISM Band). Then, the geometry was modified with a linear taper to account for the effect of the dielectric loading of the biological tissue on the input impedance. This taper was subsequently optimized through an iterative process of simulations guided by the analytical model. Finally, the array geometry and antenna spacing were optimized using a similar iterative process of computer simulation. Further details can be found in [23] and [24].

2) *Emulsion Matching Medium and Gelatin Phantoms*: A surfactant-stabilized two-phase oil-in-water emulsion is used as a matching medium designed for optimal coupling of microwave power between the array and the breast. Oil-in-water emulsions were chosen due to their straightforward fabrication from readily available, inexpensive materials, their relatively low attenuation, low viscosity for ease of circulation, and the ability to adjust their dielectric properties to match the tissue of interest simply by varying the ratio of oil and water. The emulsion coupling medium used in the current therapy system is composed of 60% vegetable oil, 36% DI water, and 4% HLB10 surfactant (46% SPAN 80 and 54% TWEEN 80) and was emulsified using an ultrasonic sonicator. The dielectric properties of the emulsion coupling medium were measured using the Agilent 85070E open-ended coaxial dielectric probe kit to be $\epsilon_r = 22.9$ and $\sigma = 0.07$ at 915 MHz. In order to dissipate the heat generated by the absorption of the significant electromagnetic energy present in the immediate near field of the antenna elements, the emulsion matching medium was circulated and cooled using an ice water bath. Both heterogeneous [see Fig. 4(a)] and homogeneous [see Fig. 4(b)] solid phantoms were created with a range of dielectric properties by adding unflavored gelatin to

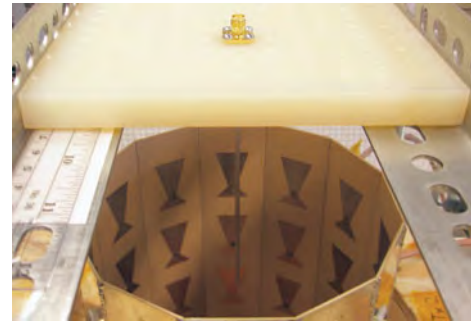


Fig. 5. Coaxial probe for mapping microwave power distribution in the plane of the therapy array (shown in photo without coupling fluid for clarity).

emulsions with varying ratios of oil/water that were heated to slightly below boiling. Further details of the emulsion coupling fluid and tissue-mimicking phantoms can be found in [25].

C. System Characterization

1) *Characterization of Microwave Power Delivery*: In order to evaluate the focusing ability of the system, the microwave power distribution within the therapy chamber filled with homogeneous coupling fluid was measured using a coaxial probe (shown in Fig. 5). The probe was manually positioned on a 2-D grid with 5-mm spacing, and the field for 49 electronically scanned focal states was measured at each position. From these data, microwave power distribution maps were created for each focal state, and the results are discussed in Section III-B.

2) *Characterization of Thermal Distribution*: A series of focused heating experiments was conducted on a number of tissue-mimicking gelatin phantoms. To initially confirm that focused heating was occurring at the desired location, temperature measurements were taken after a series of heating times using simple digital probe thermometers at several sample locations within a gelatin phantom and surrounding emulsion matching medium [shown in Fig. 4(a)]. Following these simple temperature probe experiments, a linear array of thermistors [as shown in Fig. 4(b)] was used to map the temperature distribution throughout the therapy array for a number of gelatin phantoms, focal locations, and heating times. This was accomplished by first orienting the seven-element thermistor array along one of the principal axes of the cavity. The array was continually lowered by hand to 20 points in depth at 0.5-cm increments, where the temperature measured by each thermistor was recorded. This was done for seven different positions across the cavity, spaced at 1.5-cm increments, in order to create a $7 \times 7 \times 20$ array of temperature samples which span the volume of the gelatin phantoms as well as a portion of the surrounding coupling medium.

While temperature probes are used here, in the clinical setting, an integrated noninvasive method of real-time thermal monitoring will be needed. One possible method would involve using a ring array of transducer elements integrated into the current microwave array to perform ultrasonic transmission tomography. Using this method, the opposite sign of the thermal dependence of speed of sound in fat- and water-bearing tissues can be accounted for given the substantially different speeds of sound of these two tissue classes [26], [27]. Imaging temperature with

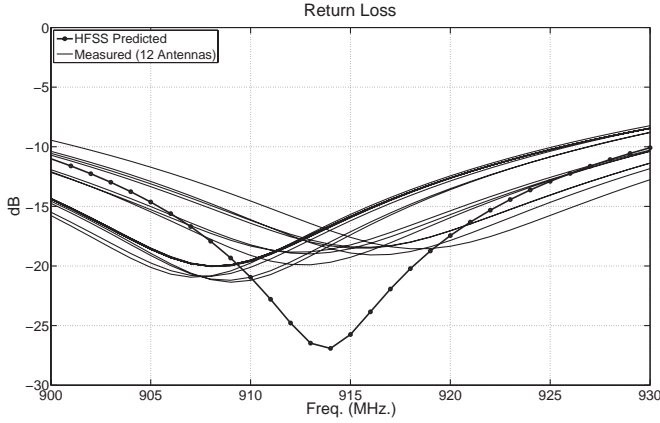


Fig. 6. HFSS predicted versus measured antenna reflection coefficients.

TABLE I
DIELECTRIC VALUES USED IN NUMERICAL BREAST PHANTOMS

Material	ϵ_r	σ (S/m)
Glandular Tissue (1.1, 1.2, 1.3)	55, 45, 35	0.6, 0.5, 0.4
Transitional Tissue (2)	25	0.3
Adipose Tissue (3.1, 3.2, 3.3)	15, 10, 5	0.2, 0.15, 0.1
Skin	40	1.0
Muscle (Chest Wall)	65	2.0
Matching Fluid	24	0.5

smaller aperture ultrasound is also possible, e.g., [28]–[30], as is microwave radiometry [31]. While real-time absolute temperature measurement is desirable, ultrasonic or other imaging of a final endpoint, such as elasticity changes from thermal necrosis, may be sufficient as well.

III. RESULTS AND DISCUSSION

A. Antenna Performance

The tapered microstrip antennas used in the therapy array were designed using Ansoft HFSS to have optimal efficiency when radiating at 915 MHz into a coupling medium with dielectric properties of $\epsilon_r = 23$ and $\sigma = 0.06$. A comparison of the HFSS predicted and measured reflection coefficients for each of the 12 therapy antennas is shown in Fig. 6, demonstrating that all of the antennas are well matched (reflection coefficient less than -15 dB) at 915 MHz radiating into the coupling medium.

B. Array Focusing

1) *Synthetic Focusing Tests in Anatomically Realistic Numerical Breast Phantoms:* The focusing capabilities of the time-reversal method were first tested synthetically using a ten-element array to focus within a variety of anatomically realistic numerical breast phantoms. These modeling tests were performed by importing MRI-based numerical breast phantoms [32] that spanned the range of BIRADS breast types [33] into COMSOL, which was then used to simulate the interaction of the time-reversal-focused electromagnetic waves with the reported [34], [35] electrical properties (see Table I) of the various breast tissue types. These results (shown in Fig. 7)

demonstrate the ability of the system to achieve focusing within a 1.5-cm target region—for breasts of widely differing density and heterogeneity—without prohibitive microwave power delivery to other regions of the breast.

2) *Experimental Focusing Tests in Coupling Media:* The microwave power distribution for 49 focal states was measured using a coaxial probe that was manually positioned on a 2-D grid with 5-mm spacing (see Fig. 5). Microwave power distribution maps for nine sample focal states are shown in Fig. 8. These results suggest that using the current time-reversal method with a 12-element, 15-cm-diameter cylindrical array (each element 7.5 cm from the center) can achieve suitable focusing within a circular region approximately 10 cm in diameter. This is evident by good targeting accuracy, focal spot size and shape, and power delivered to the target location in this region. However, near the perimeter of the chamber, we observe reduced targeting accuracy, deformed and reduced focal spots, and significant side lobes, which are expected. These limitations can be overcome with additional elements or modifications to the geometry of the array as needed for a given focusing requirement.

C. Thermal Distribution in Tissue-Mimicking Phantoms

In the first series of phantom heating experiments, temperature measurements were taken using digital probe thermometers at sample locations within a gelatin phantom and surrounding emulsion matching medium [see Fig. 4(a)]. Following these simple temperature probe experiments, a linear array of thermistors [see Fig. 4(b)] was used to map the temperature distribution throughout the phantom and surrounding fluid for a number of gelatin phantoms, focal locations, and heating times. The results of both the thermistor array mapping and the digital probe measurements for a focal spot offset 3 cm from the center of the therapy chamber are presented in Fig. 9. In these tests, as in others performed on phantoms of different sizes and composition (some containing cancer mimicking inclusions), significant differential heating was observed at the target location.

Finally, temperature maps of the focal planes are shown for both a 3-cm offset case (see Fig. 10) and a center-focused case (see Fig. 11). These results show that the temperature distribution is in good agreement with the earlier microwave power maps. The asymmetry around the focal spots along the x -direction seen in the offset focus case is most likely due to imprecision in the manual placement of the thermistor array. Despite their somewhat low resolution, they confirm the ability of the system to achieve an antitumor effect within a 1.5-cm target region in the array plane without unwanted heating in any other region.

IV. CONCLUSION

A preclinical prototype of a microwave thermal therapy system that employs an image-based time-reversal method has been developed and tested. Simulated and experimental results have demonstrated that such a system can achieve suitable focusing and heating for the potential application of thermal therapy of the breast. Based on the results of these studies, the design and fabrication of a clinically viable focused microwave array is currently underway that will demonstrate full 3-D focusing ability

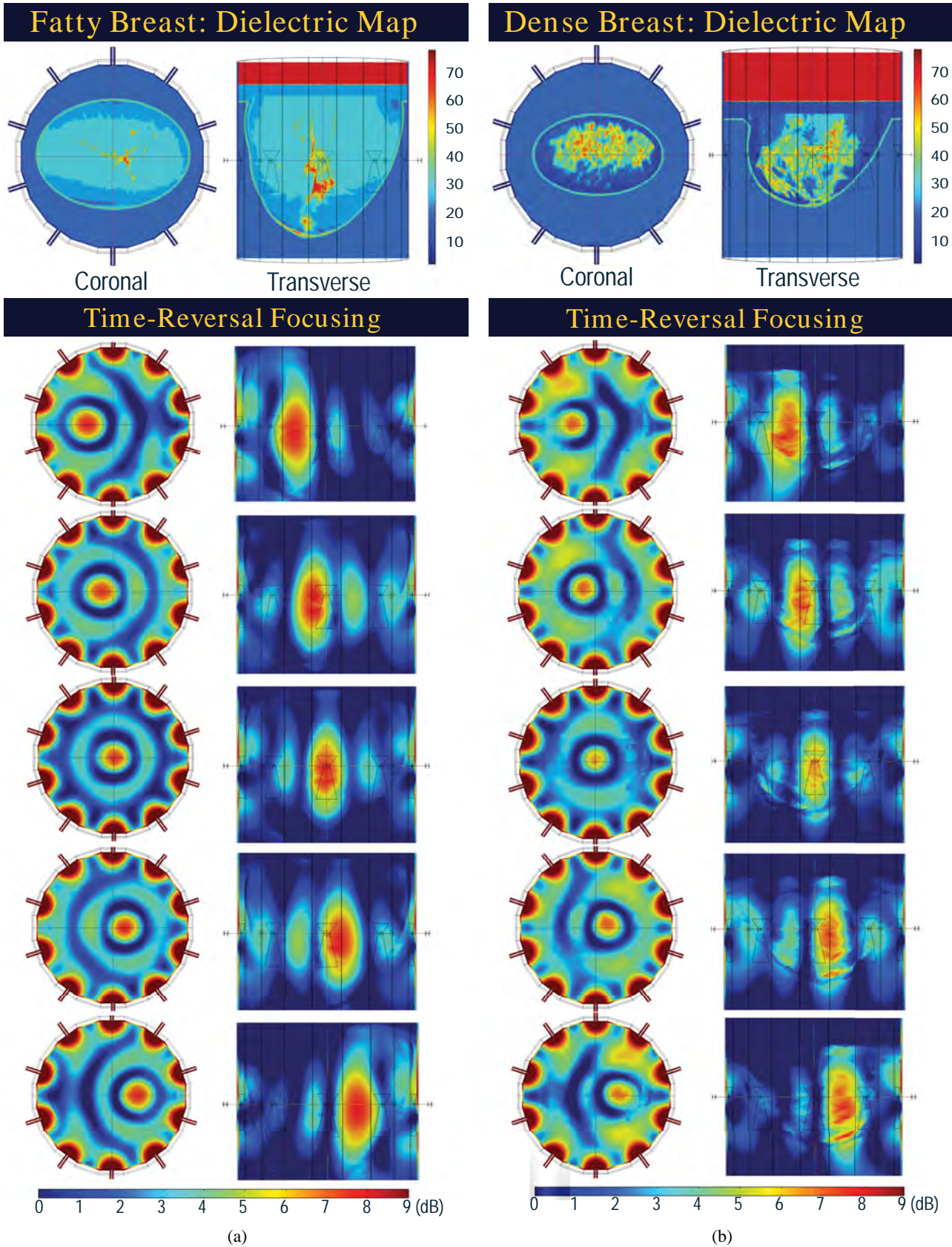


Fig. 7. COMSOL predicted microwave power distributions for time-reversal focusing in (a) fatty and (b) dense breast (ten-element array). Elongation in transverse plane due to 2-D array focusing.

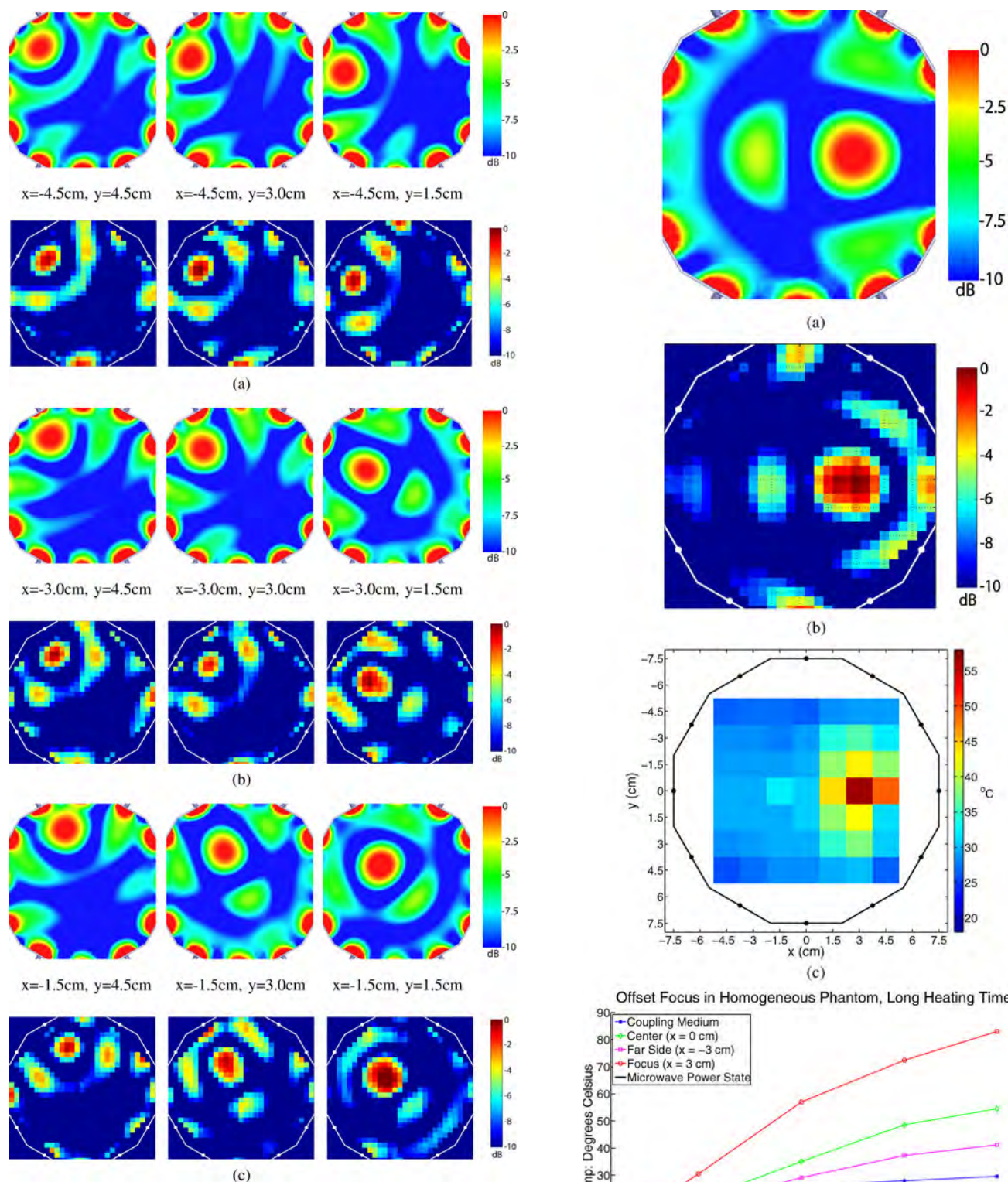


Fig. 8. Microwave power distributions on a subgrid with 1.5-cm spacing: simulated results on top versus measured results on bottom. (a) $x = -4.5$ cm, (b) $x = -3.0$ cm, and (c) $x = -1.5$ cm.

using nonlinear array optimization techniques with substantially improved anterior to posterior concentration of heating and more efficient cooling of the coupling fluid. Upon completion, the focused microwave thermal therapy system will have the potential to be used in neoadjuvant tumor treatment prior to surgery, to

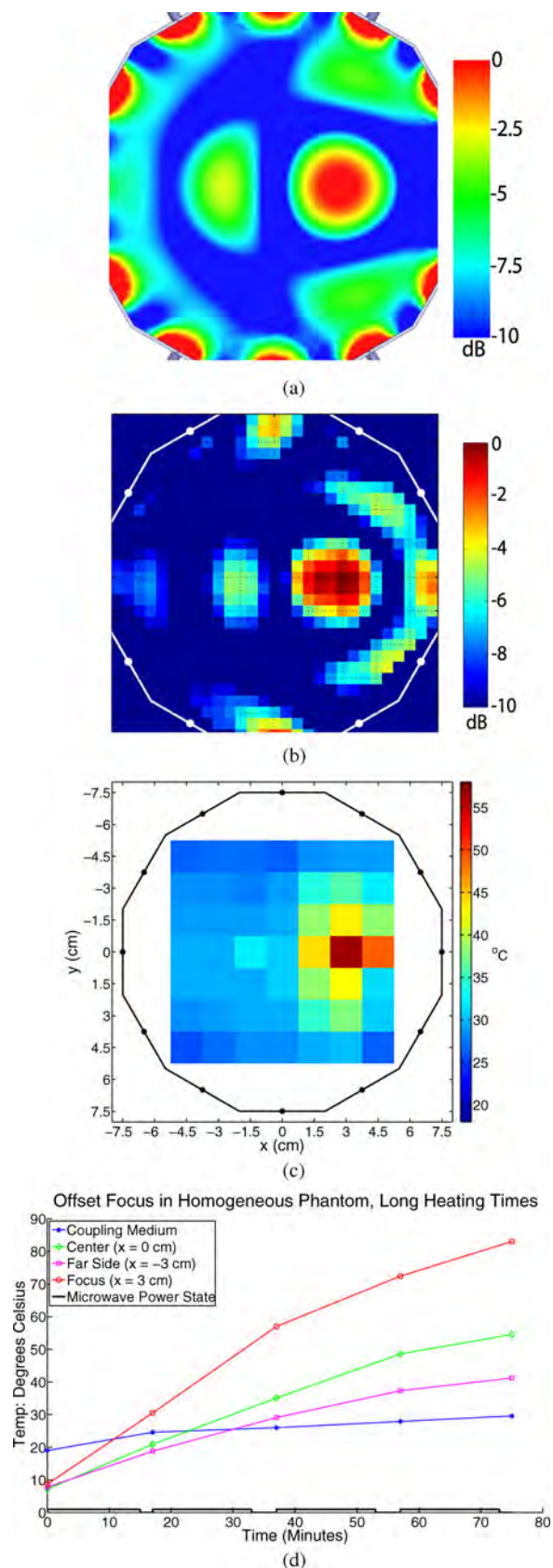


Fig. 9. Focus at $x = 3$ cm and $y = 0$ cm. (a) Simulated microwave power distribution. (b) Measured microwave power distribution. (c) Temperature after 45 min of heating, measured with thermistor array. (d) Temperature as a function of time, measured with digital probe thermometers.

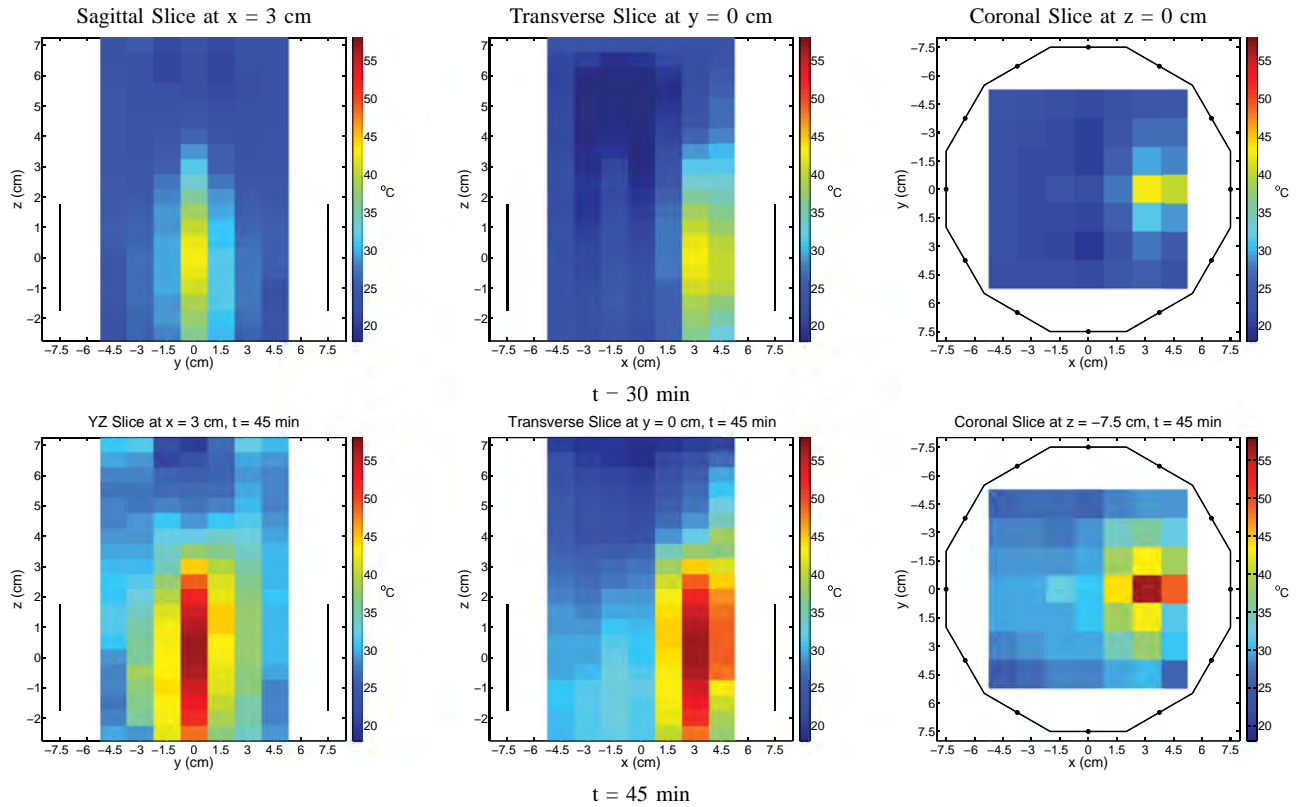


Fig. 10. Temperature maps of focused heating at $x = 3$ cm and $y = 0$ cm in homogeneous phantom for 30- and 45-min heating times. Sagittal and transverse slices show vertical extent of the active antennas; coronal slice outlines the chamber.

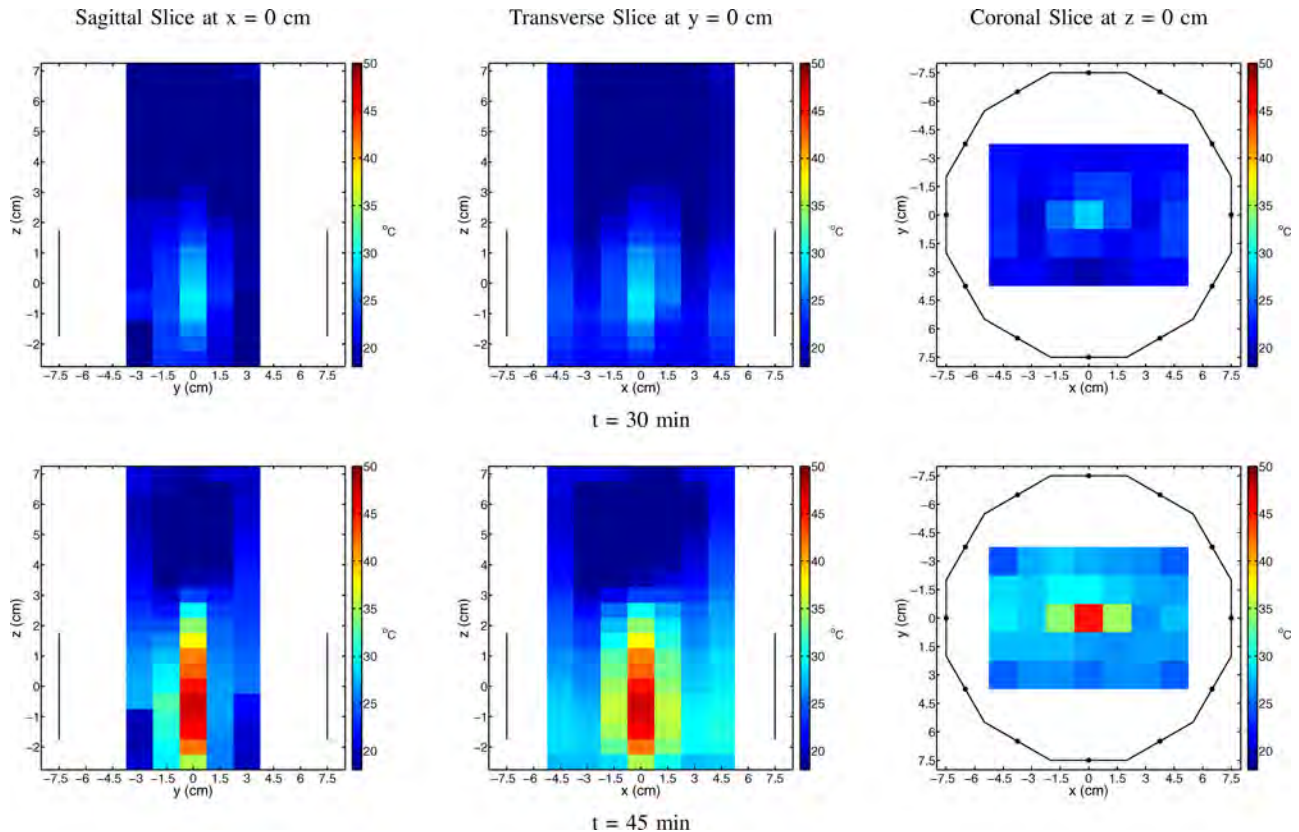


Fig. 11. Temperature maps of focused heating at $x = 0$ cm and $y = 0$ cm in homogeneous phantom for 30- and 45-min heating times. Sagittal and transverse slices show vertical extent of the active antennas; coronal slice outlines the chamber.

completely ablate the tumor, to selectively enhance drug delivery and absorption through focused thermal release, or as an adjuvant to postoperative radiation therapy and chemotherapy.

ACKNOWLEDGMENT

The authors would like to thank B. Fowlkes for his guidance on the system design, O. Kripfgans for his assistance with the modeling of numerical breast phantoms, and C. Ward, S. Clarkson, M. Fabiilli, and L. van Nieuwstadt for their assistance with the development and measurement of the emulsion coupling fluid.

REFERENCES

- [1] J. E. Kennedy, "High-intensity focused ultrasound in the treatment of solid tumours," *Nature Rev. Cancer*, vol. 5, pp. 321–327, 2005.
- [2] C. C. Vernon, J. W. Hand, S. B. Field, D. Machin, J. B. Whaley, J. van der Zee, W. L. J. van Putten, G. C. van Rhoon, J. D. P. van Dijk, D. G. González, F. Liu, P. Goodman, and M. Sherar, "Radiotherapy with or without hyperthermia in the treatment of superficial localized breast cancer: Results from five randomized controlled trials," *Int. J. Radiat. Oncol. Biol. Phys.*, vol. 35, pp. 731–744, 1996.
- [3] Z. Vujaskovic, D. W. Kim, E. Jones, L. Lan, L. McCall, M. W. Dewhirst, O. Craciunescu, P. Stauffer, V. Liotcheva, A. Betof, and K. Blackwell, "A phase I/II study of neoadjuvant liposomal doxorubicin, paclitaxel, and hyperthermia in locally advanced breast cancer," *Int. J. Hyperthermia*, vol. 26, no. 5, pp. 514–521, 2010.
- [4] B. Hildebrandt, P. Wust, O. Ahlers, A. Dieing, G. Sreenivasa, T. Kerner, R. Felix, and H. Riess, "The cellular and molecular basis of hyperthermia," *Critical Rev. Oncology/Hematology*, vol. 43, no. 1, pp. 33–56, Jul. 2002.
- [5] M. W. Dewhirst, B. L. Viglianti, M. Lora-Michiels, M. Hansen, and P. J. Hoopes, "Basic principles of thermal dosimetry and thermal thresholds for tissue damage from hyperthermia," *Int. J. Hyperthermia*, vol. 19, pp. 267–294, 2003.
- [6] E. Jones, D. Thrall, M. W. Dewhirst, and Z. Vujaskovic, "Prospective thermal dosimetry: The key to hyperthermia future," *Int. J. Hyperthermia*, vol. 22, pp. 247–253, 2006.
- [7] W. C. Dooley, H. I. Vargas, A. J. Fenn, M. B. Tomaselli, and J. K. Harness, "Focused microwave thermotherapy for preoperative treatment of invasive breast cancer: A review of clinical studies," *Ann. Surg. Oncol.*, vol. 17, pp. 1076–1093, 2010.
- [8] H. I. Vargas, W. C. Dooley, R. A. Gardner, K. D. Gonzalez, R. Venegas, S. H. Heywang-Kobrunner, and A. J. Fenn, "Focused microwave phased array thermotherapy for ablation of early-stage breast cancer: Results of thermal dose escalation," *Ann. Surg. Oncol.*, vol. 11, pp. 139–146, 2004.
- [9] Z. Li, M. Vogel, P. F. Maccarini, V. Stakhursky, B. J. Soher, S. Das, O. A. Arabe, W. T. Joines, and P. R. Stauffer, "Improved hyperthermia treatment control using SAR/temperature simulation and PRFS magnetic resonance thermal imaging," *Int. J. Hyperthermia*, vol. 27, no. 1, pp. 86–99, 2011.
- [10] P. R. Stauffer, P. Maccarini, K. Arunachalam, O. Craciunescu, C. Diederich, T. Juang, F. Rossetto, J. Schlorff, A. Milligan, J. Hsu, P. Sneed, and Z. Vujaskovic, "Conformal microwave array (CMA) applicators for hyperthermia of diffuse chestwall recurrence," *Int. J. Hyperthermia*, vol. 26, no. 7, pp. 686–698, 2010.
- [11] K. S. Cheng, M. W. Dewhirst, P. R. Stauffer, and S. Das, "Effective learning strategies for real-time image-guided adaptive control of multiple source hyperthermia applicators," *Med. Phys.*, vol. 37, no. 3, pp. 1285–1297, 2010.
- [12] *Phase 1/2 study of ThermoDox with approved hyperthermia in treatment of breast cancer recurrence at the chest wall (DIGNITY)*. Bethesda, MD. NCT00826085. (ClinicalTrials.gov).
- [13] *Phase 3 study of ThermoDox with radiofrequency ablation (RFA) in treatment of hepatocellular carcinoma (HCC)*. Bethesda, MD. NCT00617981. (ClinicalTrials.gov).
- [14] C. D. Landon, J. Park, D. Needham, and M. W. Dewhirst, "Nanoscale drug delivery and hyperthermia: The materials design and preclinical and clinical testing of low temperature-sensitive liposomes used in combination with mild hyperthermia in the treatment of local cancer," *The Open Nanomed. J.*, vol. 3, pp. 38–64, 2011.
- [15] A. Surowiec and H. I. Bicher, "Heating characteristics of the TRIPAS hyperthermia system for deep seated malignancy," *J. Microw. Power Electromagn. Energy*, vol. 30, no. 3, pp. 135–40, 1995.
- [16] A. J. Fenn, G. L. Wolf, and R. M. Fogle, "An adaptive microwave phased array for targeted heating of deep tumours in intact breast: Animal study results," *Int. J. Hyperthermia*, vol. 15, pp. 45–61, 1999.
- [17] R. A. Gardner, H. I. Vargas, J. B. Block, C. L. Vogel, A. J. Fenn, G. V. Kuehl, and M. Doval, "Focused microwave phased array thermotherapy for primary breast cancer," *Ann. Surg. Oncol.*, vol. 9, pp. 326–332, 2002.
- [18] K. Arunachalam, S. S. Udpa, and L. Udpa, "Computational feasibility of deformable mirror microwave hyperthermia technique for localized breast tumors," *Int. J. Hyperthermia*, vol. 23, pp. 577–589, 2007.
- [19] M. Converse, E. J. Bond, B. D. Van Veen, and S. C. Hagness, "A computational study of ultrawideband versus narrowband microwave hyperthermia for breast cancer treatment," *Microw. Theory Tech.*, vol. 54, pp. 2169–2180, 2006.
- [20] M. Fink, D. Cassereau, A. Derode, C. Prada, M. Tanter, J. L. Thomas, and F. Wu, "Time reversed acoustics," *Rep. Prog. Phys.*, vol. 63, pp. 1933–1995, 2000.
- [21] B. Guo, L. Xu, and J. Li, "Time reversal based hyperthermia treatment of breast cancer," *Microw. Opt. Tech. Lett.*, vol. 47, no. 4, pp. 335–338, Nov. 2005.
- [22] P. Kosmas, E. Zastrow, S. C. Hagness, and B. D. Van Veen, "A computational study of time reversal techniques for ultra-wideband microwave hyperthermia treatment of breast cancer," in *Proc. IEEE/SP 14th Workshop Statist. Signal Process.*, Aug. 26–29, 2007, pp. 312–316.
- [23] J. P. Stang and W. T. Joines, "Tapered microstrip patch antenna array for microwave breast imaging," in *Proc. IEEE MTT-S Int. Microw. Symp. Dig. Dig.*, 2008, pp. 1313–1316.
- [24] J. P. Stang, W. T. Joines, Q. H. Liu, G. A. Ybarra, M. Yuan, and I. Leonhardt, "Tapered microstrip patch antenna array for use in breast cancer screening via 3D active microwave imaging," in *Proc. IEEE Int. Symp. Antennas Propag.*, 2009, pp. 1–4.
- [25] J. P. Stang, C. Ward, L. van Nieuwstadt, M. Fabiilli, M. Haynes, P. Carson, and M. Moghaddam, "Customizable emulsion matching media and tissue mimicking phantoms for microwave breast imaging and therapy," *Phys. Med. Biol.*, to be published.
- [26] S. A. Johnson, D. A. Christensen, and B. Baxter, "Noninvasive acoustic temperature tomography for measurement of microwave and ultrasound-induced hyperthermia," *J. Bioeng.*, vol. 1, no. 5/6, pp. 555–570, 1977.
- [27] I. Jovanovifa, A. Hormati, P. Littrup, N. Duric, O. Rama, and M. Vetterli, "Temperature monitoring during tissue freezing using ultrasound speed measurements," in *Proc. SPIE Med. Imaging.*, 2009, vol. 7265, pp. 72650Q-1–72650Q-8.
- [28] P. VanBaren and E. S. Ebbini, "Multipoint temperature control during hyperthermia treatments: Theory and simulation," *IEEE Trans. Biomed. Eng.*, vol. 42, no. 8, pp. 818–827, Aug. 1995.
- [29] R. Seip and E. S. Ebbini, "Noninvasive estimation of tissue temperature response to heating fields using diagnostic ultrasound," *IEEE Trans. Biomed. Eng.*, vol. 42, no. 8, pp. 828–839, Aug. 1995.
- [30] D. Liu and E. S. Ebbini, "Real-time 2-D temperature imaging using ultrasound," *IEEE Trans. Biomed. Eng.*, vol. 57, no. 1, pp. 12–16, Jan. 2010.
- [31] K. Arunachalam *et al.*, "Characterization of a digital microwave radiometry system for noninvasive thermometry using a temperature-controlled homogeneous test load," *Phys. Med. Biol.*, vol. 53, no. 14, pp. 3883–3901, Jul. 21, 2008.
- [32] E. Zastrow, S. K. Davis, M. Lazebnik, F. Kelcz, B. D. Van Veen, and S. C. Hagness, "Database of 3D grid-based numerical breast phantoms for use in computational electromagnetics simulations. (2007). [Online]. Available: <http://uwcem.ece.wisc.edu/MRI/database/>
- [33] C. J. D'Orsi, L. W. Bassett, and W. A. Berg, *Breast Imaging Reporting and Data System (BI-RADS) Atlas*, 4th ed. Reston, VA: ACR, 2003.
- [34] M. Lazebnik, L. McCartney, D. Popovic, C. B. Watkins, M. J. Lindstrom, J. Harter, S. Sewall, A. Magliocco, J. H. Booske, M. Okoniewski, and S. C. Hagness, "A large-scale study of the ultrawideband microwave dielectric properties of normal breast tissue obtained from reduction surgeries," *Phys. Med. Biol.*, vol. 52, pp. 2637–2656, 2007.
- [35] M. Lazebnik, D. Popovic, L. McCartney, C. B. Watkins, M. J. Lindstrom, J. Harter, S. Sewall, T. Ogilvie, A. Magliocco, T. M. Breslin, W. Temple, D. Mew, J. H. Booske, M. Okoniewski, and S. C. Hagness, "A large-scale study of the ultrawideband microwave dielectric properties of normal, benign and malignant breast tissues obtained from cancer surgeries," *Phys. Med. Biol.*, vol. 52, pp. 6093–6115, 2007.

Authors' photographs and biographies not available at the time of publication.

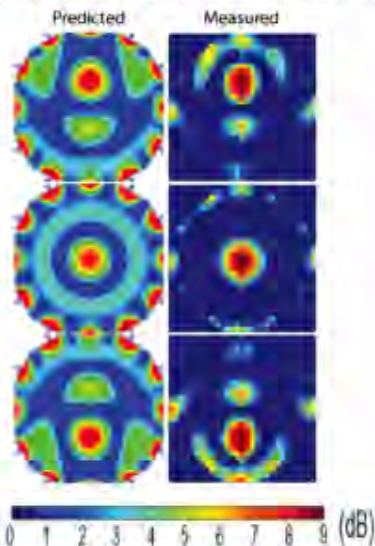
Improving External Treatments for Breast Cancer Tumors

Mahta Moghaddam, University of Southern California

Paul Carson, University of Michigan

FY09 Idea Award

Malignant tissues have electrical and acoustical properties that make them distinguishable from healthy tissue, including an ability to highly absorb microwave and ultrasound energy and thus be heated more quickly than surrounding tissue. This property can be exploited for thermal therapies in which elevated temperatures are used to achieve cell death or render the cells more vulnerable to ionizing radiation and chemotherapy. Both microwave and ultrasound modalities have been used for thermal therapies; however, there are limitations with each method. Drs. Moghaddam and Carson are investigating the combination of two thermal therapies: high



steering ability of the array is clearly demonstrated.

Dr. Moghaddam is working to improve targeting the microwaves in HIFW to overcome focus and uniformity issues using an array design that could be fine-tuned for each patient. (Fig. 1a). Dr. Carson is developing a transducer array that will allow placement of the HIFU focal zone close to the chest wall and permit ablation of deep tumors at higher speed and uniformity than currently possible with ultrasound (Fig. 1b). Using information gathered from the study of each treatment modality, the collaborators aim to combine these therapies in a microwave-ultrasound synergistic thermal (MUST) treatment system. Experimental results using laboratory prototypes generated focused heating sufficient for an antitumor effect in tissue-mimicking gelatin phantoms. The heating focal spot sizes were as small as 1.5 cm with microwaves and 1.5 mm with ultrasound. Further development of the MUST system will capitalize on the strengths of each modality such that the combined system could substantially enhance treatment results through precise and uniform heating accompanied by simultaneous imaging of the temperature.

intensity focused ultrasound (HIFU), which is limited in its efficiency to treat large tumors fast with uniformity, and high intensity focused microwave (HIFW), which can treat fast and relatively uniformly but without the resolution to avoid heating adjacent healthy tissues or to achieve uniform heating at sharp boundaries of tissue properties. The proposed combined system seeks to remove the limitations inherent in individual application of these therapies.

Fig 1a. Predicted field intensities beside measured thermal maps in the 20cm treatment chamber. The

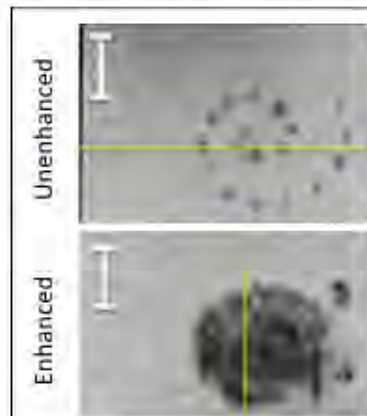


Fig. 1b. T2-weighted MR images of ultrasound thermal lesions in a uniform gel, placed in a spiral without (top) and with (bottom) controlled gas bubble generation from IV administered perfluorocarbon microdroplets. The latter greatly enhances heating only in the focal zone. Note the small, sparse lesions in the top, "unenhanced" image and the uniform coverage from larger lesions in the "enhanced" image. Both were obtained in the same exposure time and ultrasound output levels.